Award Number: 06HQGR0160

GROUND MOTIONS FROM LARGE CASCADIA SUBDUCTION EARTHQUAKES

FINAL REPORT

September 3, 2008

P. Somerville, R. Graves and N. Collins*

URS Group, Inc.

566 El Dorado Street
Pasadena, CA 91101

Tel: (626) 449-7650
Fax: (626) 449-3536

*Email: paul_somerville@urscorp.com

Research supported by the U.S. Geological Survey (USGS), Department of the Interior, under award number 06HQGR0202. The views and conclusions contained in this document are those of the authors and should not be interpreted as necessarily representing the official policies, either expressed or implied, of the U.S. Government.

GROUND MOTIONS FROM LARGE CASCADIA SUBDUCTION EARTHQUAKES

SUMMARY

Ground motions from great subduction earthquakes on the Cascadia plate interface make a major contribution to the ground motion hazard in the USGS National Seismic Hazard Maps and the MCE maps in most parts of the Cascadia region. In the Hazard Maps, the subduction source is modeled by earthquakes having magnitudes M_w as large as 9.2. Since these magnitudes are larger than any of the earthquakes on which current empirical ground motion models (Atkinson and Boore, 2003; Youngs et al., 1997; Zhao et al., 2006) are based, it is important to use earthquake source and strong ground motion data from recent large subduction earthquakes, such as the Mw 8.4 Arequipa, Peru earthquake of 2001, to provide insight into the nature of ground motions from such large events. The strong motion recordings of this earthquake provide the first glimpse at what the ground motions from such large earthquakes may be like.

Broadband ground motion simulations enhance the usefulness of the recordings of such earthquakes by providing a means of interpolating and extrapolating the recorded data. In this report, we first test our capability to simulate the eight broadband strong motion recordings of the Mw 8.4 Arequipa earthquake by demonstrating that our simulations reproduce the amplitudes of the recorded ground motions without systematic bias. We use simulations to make maps of the ground motions caused by the earthquake.

Based on this test using the Mw 8.4 Arequipa earthquake, we then applied the ground motion simulation procedure to estimate the ground motion characteristics of earthquakes that rupture the entire Cascadia subduction zone. We compared the simulated ground motions with those predicted by other models, and made maps of the simulated ground motions for two site conditions: soft rock (NEHRP B/C boundary), and deep soil (NEHRP D). We provide equations for predicting the response spectra of the ground motions for these two site conditions.

EARTHQUAKE SOURCE SCALING RELATIONS OF SUBDUCTION EARTHQUAKES

Somerville et al. (2002) developed scaling relations for the source parameters of subduction earthquakes, based on the rupture models of seven large subduction earthquakes. These models are analogous to those we developed for crustal earthquakes (Somerville et al., 1999). The subduction earthquakes used in these scaling relations include three earthquakes whose rupture models we developed: 1923 Tokyo, Japan (Wald and Somerville, 1995); 1944 Tonankai, Japan (Ichinose et al., 2003); and 2001 Peru (Somerville et al., 2003). The rupture models portray the spatial and temporal distribution of slip on the fault plane, as inferred from strong motion recordings, teleseismic data, and in some cases geodetic and tsunami observations. The scaling relations describe the scaling with seismic moment of rupture area, rise time, asperity dimensions, and the corner periods of spatial wavenumber models of fault slip heterogeneity, which control the spatial distribution of slip and slip velocity.

We used the Somerville et al. (2002) scaling relations to characterize the spatial and temporal distribution of slip on the rupture plane of future large subduction earthquakes. The relation between seismic moment and rupture area for subduction earthquakes was found to be:

$A = 5.2 \times 10^{-15} Mo^{2/3}$

For a given seismic moment, the subduction earthquake rupture area is more than twice as large as that found for crustal earthquakes by Somerville et al. (1999):

$A = 2.23 \times 10^{-15} Mo^{2/3}$

Consequently, for a given seismic moment, subduction earthquakes have average slip that is less than half that of crustal earthquakes.

Somerville et al. (2002) also measured the rise time of both subduction and crustal earthquakes based on the maximum slip velocity (Ishii et al., 2002). They found that the rise time for both subduction and crustal earthquakes is given by:

$T_r = 1.8 \times 10^{-9} Mo^{1/3}$

Since the slip in subduction earthquakes is less than half that in crustal earthquakes of the same seismic moment, a similar rise time implies that the slip velocity on the fault in subduction earthquakes is less than half that in crustal earthquakes. This causes the ground motions of subduction earthquakes to be weaker than those of crustal earthquakes having the same seismic moment.

PROCEDURE FOR BROADBAND STRONG GROUND MOTION SIMULATION

We use a hybrid broadband ground motion simulation approach, based on frequency-wavenumber Green's functions for long periods (> 3sec) and on a partly stochastic ray theory method (Somerville et al., 1991) for shorter periods, to simulate broadband ground motions for large subduction earthquakes. We showed in earlier work that the short period simulation procedure successfully reproduces the recorded ground motions of the M_w 8.0 Valparaiso, Chile and Michoacan, Mexico earthquakes of 1985 (Somerville et al., 1991), and on that basis we applied it to simulate the ground motions of M_w 8.0 Cascadia earthquakes (Cohee et al., 1991). Specifically, we used the Caleta de Campos rock site recording of an aftershock of the 1985 Michoacan, Mexico earthquake as an empirical source function in the simulations, described in detail by Cohee et al. (1991).

In the hybrid broadband simulation procedure, the low frequency and high frequency components of the ground motions are computed separately and then combined using matched filters. The low frequency simulation methodology, used for periods longer than 0.3 seconds, uses a deterministic representation of source and wave propagation effects (Graves and Pitarka, 2004) that is based on the approach described by Hartzell and Heaton (1983). The basic calculation is carried out using a 1D frequency-wavenumber integration algorithm.

The earthquake source is specified by a kinematic description of fault rupture, incorporating spatial heterogeneity in slip, rupture velocity and rise time. Following Hartzell and Heaton (1983), the fault is divided into a number of subfaults. The slip and rise time are constant across each individual subfault, although these parameters are allowed to vary from subfault to subfault. We use a slip velocity function that is constructed using two triangles as shown in Figure 1. This functional form is based on results of dynamic rupture simulations (e.g., Guatteri et al., 2003). We constrain the parameters of this function as follows:

$$T_r = 1.83 \times 10^{-9} \cdot M_0^{-1/3}$$
$$T_p = 0.2 \cdot T_r$$
$$h = 0.2 \cdot A \qquad (1)$$

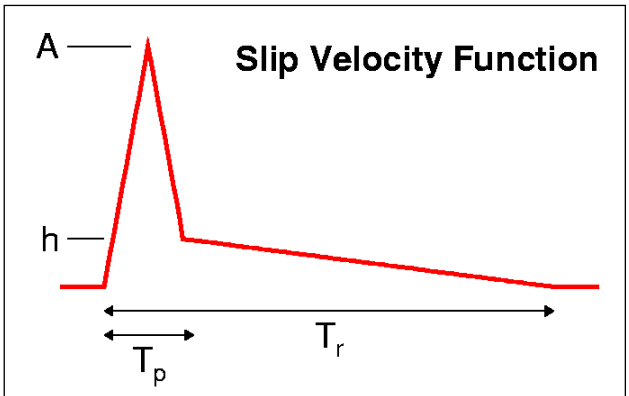

Figure 1. Slip velocity function used in the deterministic simulations [see equation (1)].

where M_0 is the seismic moment, T_r is the rise time and A is normalized to give the desired final slip. The expression for T_r comes from the empirical analysis of Somerville et al. (1999). In general, T_r may vary across the fault; however, in practice we only allow a depth dependent scaling such that T_r increases by a factor of 2 if the rupture is between 0 and 5 km depth. This is consistent with observations of low slip velocity on shallow fault ruptures (Kagawa et al., 2004).

The rupture initiation time (T_i) is determined using the expression

$$T_i = R / V_r - \delta t \qquad (2)$$
$$V_r = 0.8 \cdot V_s$$

where R is the rupture path length from the hypocenter to a given point on the fault surface, V_r is the rupture velocity and is set at 80% of the local shear wave velocity (V_s), and δt is a timing perturbation that scales linearly with slip amplitude such that $\delta t = \delta t_0$ where the slip is at its maximum and $\delta t = 0$ where the slip is at the average slip value. For these calculations, we set $\delta t_0 = 0.1\text{sec}$. This scaling results in faster rupture across portions of the fault having large slip as suggested by source inversions of past earthquakes (Hisada, 2001).

For scenario earthquakes, the slip distribution can be specified using randomized spatial fields, constrained to fit certain wave number properties (e.g., Somerville et al., 1999; Mai and Beroza, 2002). In the simulation of past earthquakes, we use smooth representations of the static slip distribution determined from finite-fault source inversions. Typically, these inversions will also include detailed information on the spatial variation of rupture initiation time and slip velocity function, either by solving for these parameters directly or by using multiple time windows. However, we do not include these in our simulations of scenario earthquakes, but rather rely on equations (1) and (2) to provide them. This is because the level of detailed resolution of these parameters provided by the source inversions will generally not be available *a priori* for future earthquakes. Furthermore, since the inversions determine these parameters by optimally fitting the selected observations, it is not clear that they will produce an optimal waveform fit at sites not used in the inversion.

The high frequency simulation methodology, used for periods shorter than 0.3 seconds, is a stochastic approach that sums the response for each subfault using empirical source functions. The simulation procedure was originally developed by Somerville et al. (1991) following the concepts of Irikura (1978) and Hartzell (1978).

The crustal structure model used in the simulations has a surface shear wave velocity of 1.5 km/sec, corresponding to the boundary between NEHRP site categories A and B. To adjust the resulting simulations to lower surface shear wave velocities, we used the NEHRP amplitude and period dependent amplification factors to scale the response spectra. The two NEHRP site conditions for which ground motion maps were generated are B/C and D. The B/C category has a surface shear wave velocity Vs30 of 0.76 km/sec to represent stiff soil /soft rock site conditions (the boundary between NEHRP S_B and S_C). This is the site condition used in the USGS National Seismic Hazard Maps and the MCE maps. For the scenario maps, in addition to maps for the B/C boundary site condition, we made maps for NEHRP site condition D – deep soil.

GROUND MOTION MODELS

We compare the ground motion estimates obtained in this report with three ground motion models for subduction earthquakes. Those three models are Atkinson and Boore (2003); Youngs et al. (1997); and Zhao et al. (2006). The former two models were derived from worldwide sets of strong motion recordings of subduction earthquakes, and the Zhao et al. (2006) model was derived from strong motion recordings from earthquakes in Japan. For the B/C site condition, we use the average of the B and C relations of Atkinson and Boore (2003); the rock relations of Youngs et al. (1997), and the SC I relations of Zhao et al. (2006). For the D site condition, we use the D relations of Atkinson and Boore (2003); the soil relations of Youngs et al. (1997), and the SC III relations of Zhao et al. (2006).

In this report, we fit a simple ground motion model to the simulations. The ground motion model has the form:

Ln (Sa) = C1 + C2 x closest distance

THE M_W 8.4 AREQUIPA, PERU EARTHQUAKE OF JUNE 23, 2001

The M_w 8.4 Arequipa, Peru earthquake of June 23, 2001 is the largest earthquake for which strong ground motion recordings have ever been obtained. The purpose of this section of the report is to find out whether this hybrid simulation procedure reproduces the features of the M_w 8.4 2001 Peru earthquake ground motions.

The rupture model that we derived for this earthquake (Somerville et al., 2003) is shown in Figures 2 and 3. The rupture zone of the earthquake was about 400 km long, and most of the slip occurred in two asperities, one at shallow depths (5 – 15 km) and the other at greater depths (25 – 40 km). Figure 3 shows the stages in the development of the rupture model used for broadband simulations. The top panel shows the slip model and rupture time model derived by Somerville et al. (2003). The next panel shows the modification of the rupture times using the dependency of rupture velocity on slip described in the preceding section. In the remaining two panels, the original slip model has been interpolated at one quarter the sampling interval of the original slip model. The rupture model shown at the bottom of Figure 2 is the one that was used for broadband simulations. The average rise time of this rupture model is 4.8 seconds, somewhat shorter than the value of 6.4 seconds predicted by the Somerville et al. (2002) scaling relations.

Strong motion recordings of the Peru earthquake were obtained in Moquegua, Peru and at seven stations in northern Chile (Boroschek and Comte, 2004), including three in Arica, whose locations are shown in Figure 2 and listed in Table 1. We used our rupture model of the 2001 Peru earthquake to simulate broadband ground motions at the eight strong motion recording sites, and at the grid of stations shown in Figure 2. We compared the recorded and simulated ground motions at the recording stations, and analyzed the ground motions simulated over the grid.

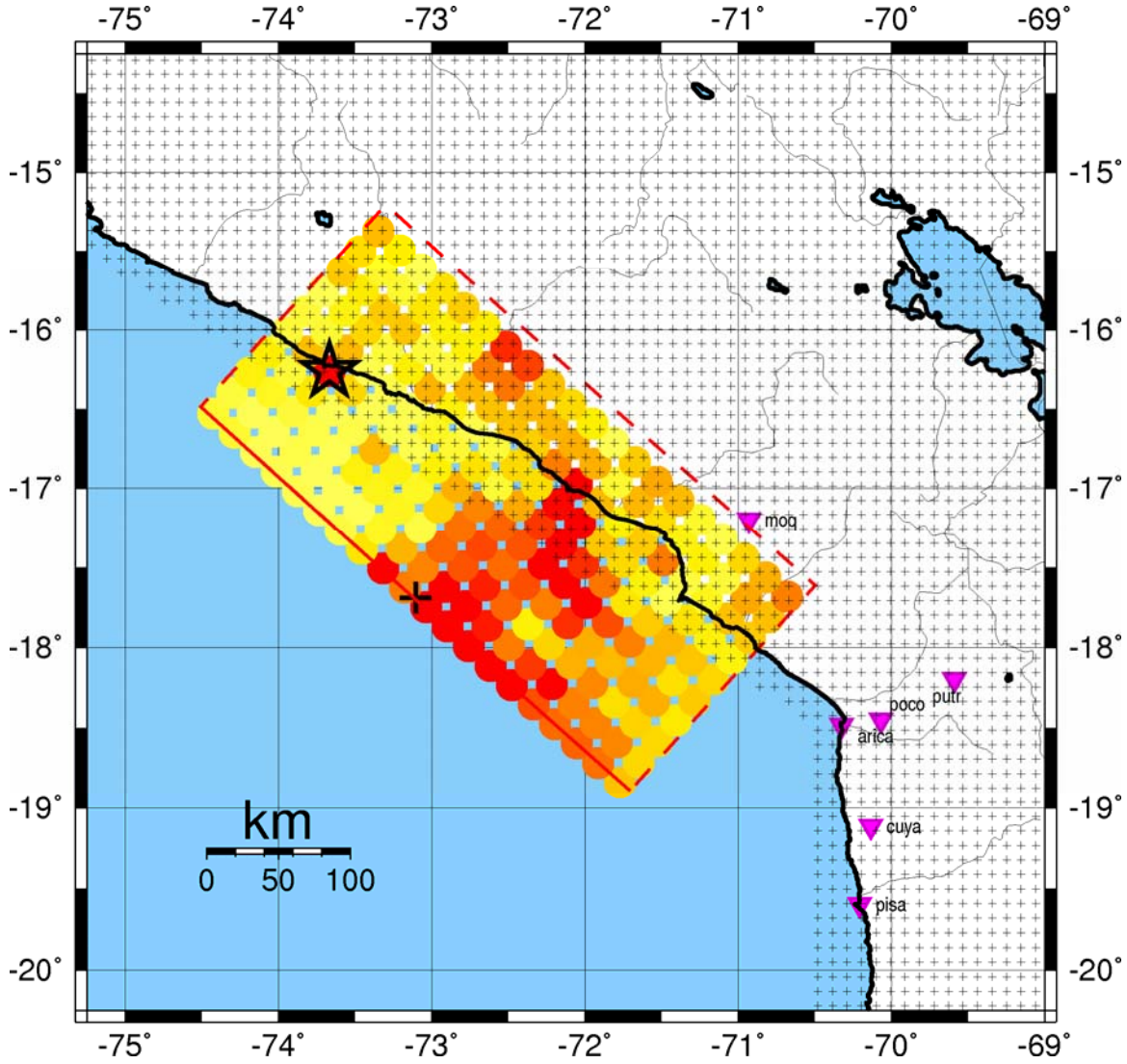

Figure 2. Rupture model of the 2001 Arequipa, Peru earthquake and locations of strong ground motion recording stations, and grid of stations used for simulations.

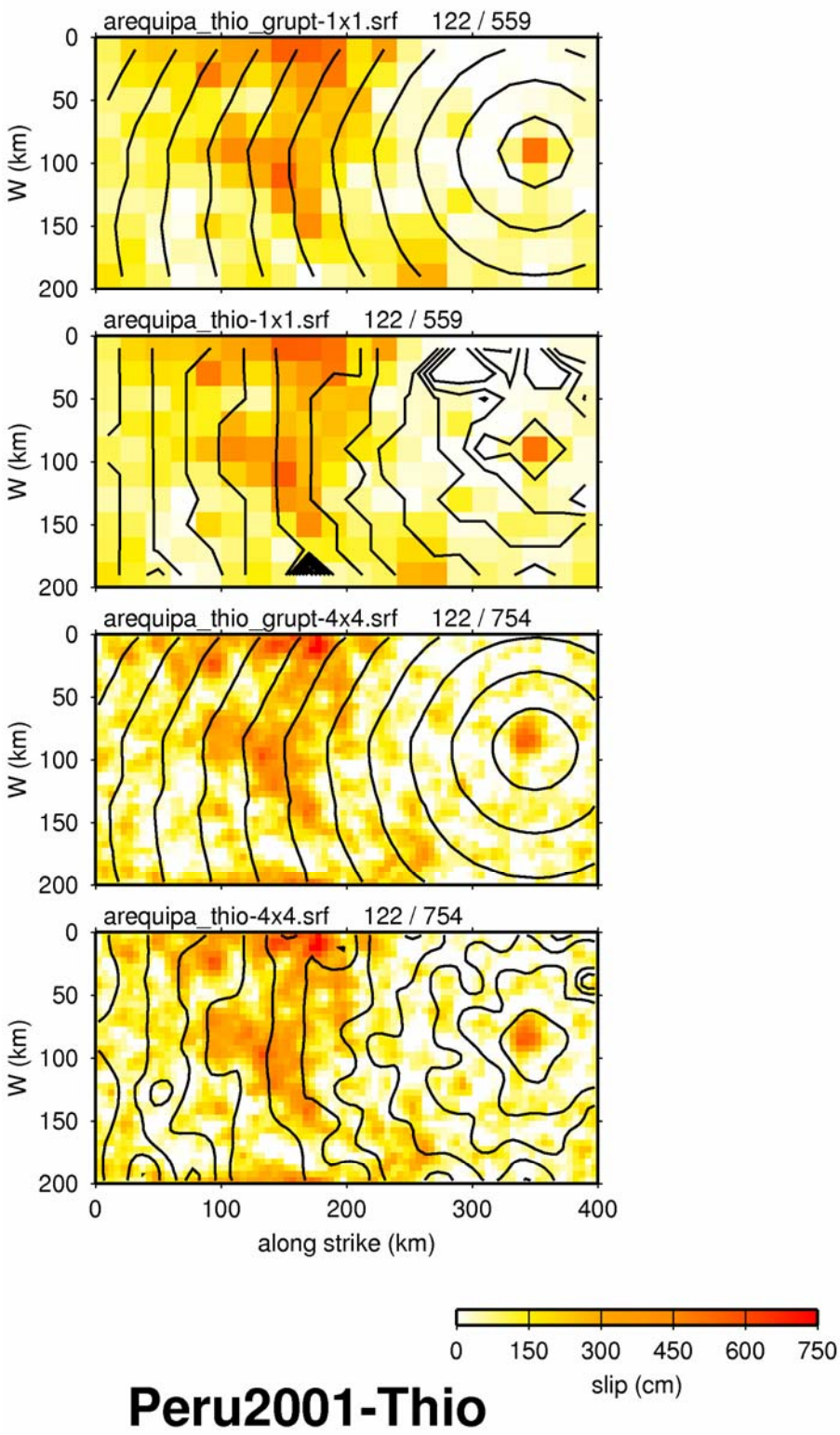

Figure 3. Rupture model of the 2001 Arequipa, Peru earthquake. Source: Somerville et al. (2003).

Table 1. Strong motion recordings of the 2001 Arequipa earthquake

Station	Abbrev	Latitude	Longitude	Site	Closest Distance	Long	Trans
Arica Casa	acas	-18.485	-70.323	soil	90.538	140	50
Arica Costanera	acos	-18.485	-70.323	soil	90.538	60	330
Arica Hospital	ahos	-18.485	-70.323	soil	90.538	0	90
Cuya	cuya	-19.117	-70.135	rock	144.820	210	120
Moquegua	moq	-17.200	-70.930	rock	61.825	0	90
Pisagua	pisa	-19.600	-70.206	rock	172.431		
Poconchile	poco	-18.450	-70.068	soil	109.023	170	80
Putre	putr	-18.198	-69.587	soil	133.833	80	150

Crustal Structure Model

The crustal velocity model that we used, which is listed in Table 2, was derived from the results of Ocola et al. (1995). This model was modified to include a shallow layer of low seismic velocity representing weathered rock.

Table 2. Crustal structure model for southern Peru. Modified from Ocola et al., 1995.

Vp	Qp	Vs	Qs	Density	Thickness
2.600	2000	1.500	900.000	2.000	0.200
5.300	2000	3.030	900.000	2.100	6.700
6.000	2000	3.370	900.000	2.500	4.600
6.500	2000	3.650	900.000	2.780	18.100
7.300	2000	4.100	900.000	3.180	15.800
8.100	2000	4.500	900.000	3.400	16.000
8.101	2000	4.501	900.000	3.401	100.000

Comparison of Recorded and Simulated Ground Motions - 2001 Arequipa Event

In Figure 4, we compare the recorded and simulated peak accelerations of the 2001 Arequipa earthquake with the predictions of three ground motion models (left), and with the average of the three models (right). The simulated values are in fairly close agreement with the recorded ones. The ground motion models are also in fairly close agreement with the recorded values.

The recorded and simulated response spectra at each station are compared in Figure 5. The agreement is quite good at Moquegua, and at the three stations in Arica for periods less than 1 second. The simulations tend to overpredict the recorded ground motions at periods between 1 and 2 seconds. Figure 6 shows the goodness of fit between the recordings and simulations at all of the stations, following the procedure of Abrahamson et al. (1990). The grey shading shows the 90th percentile confidence interval in the median prediction. There is little systematic bias in the prediction of the ground motions, although there is some underprediction at a period of 0.5 seconds and some overprediction between 1 and 2 seconds, especially on the North component. The standard error of the prediction, shown by the green shading, is about a factor of 1.5 (0.4 natural log units).

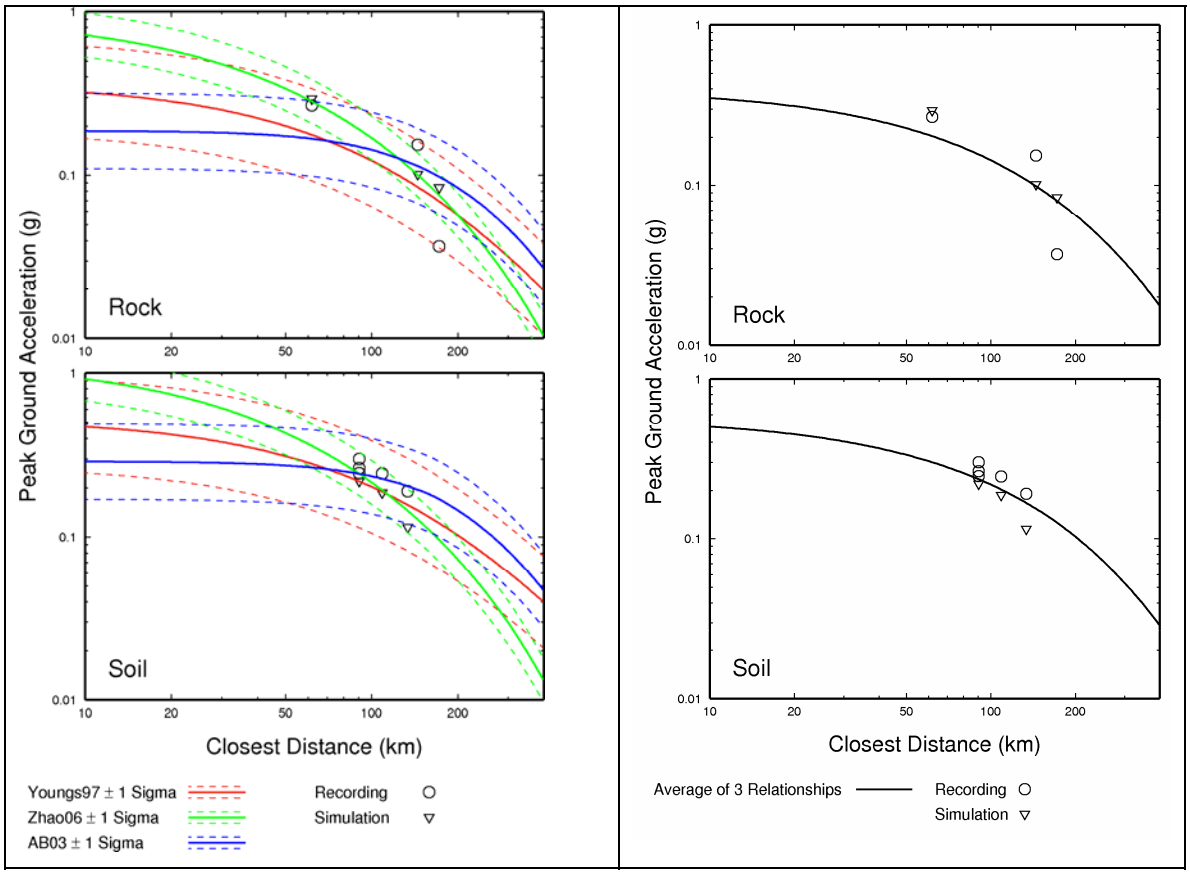

Figure 4. Comparison of recorded and simulated peak accelerations with (left): three ground motion models and (right) the average of the three ground motion models.

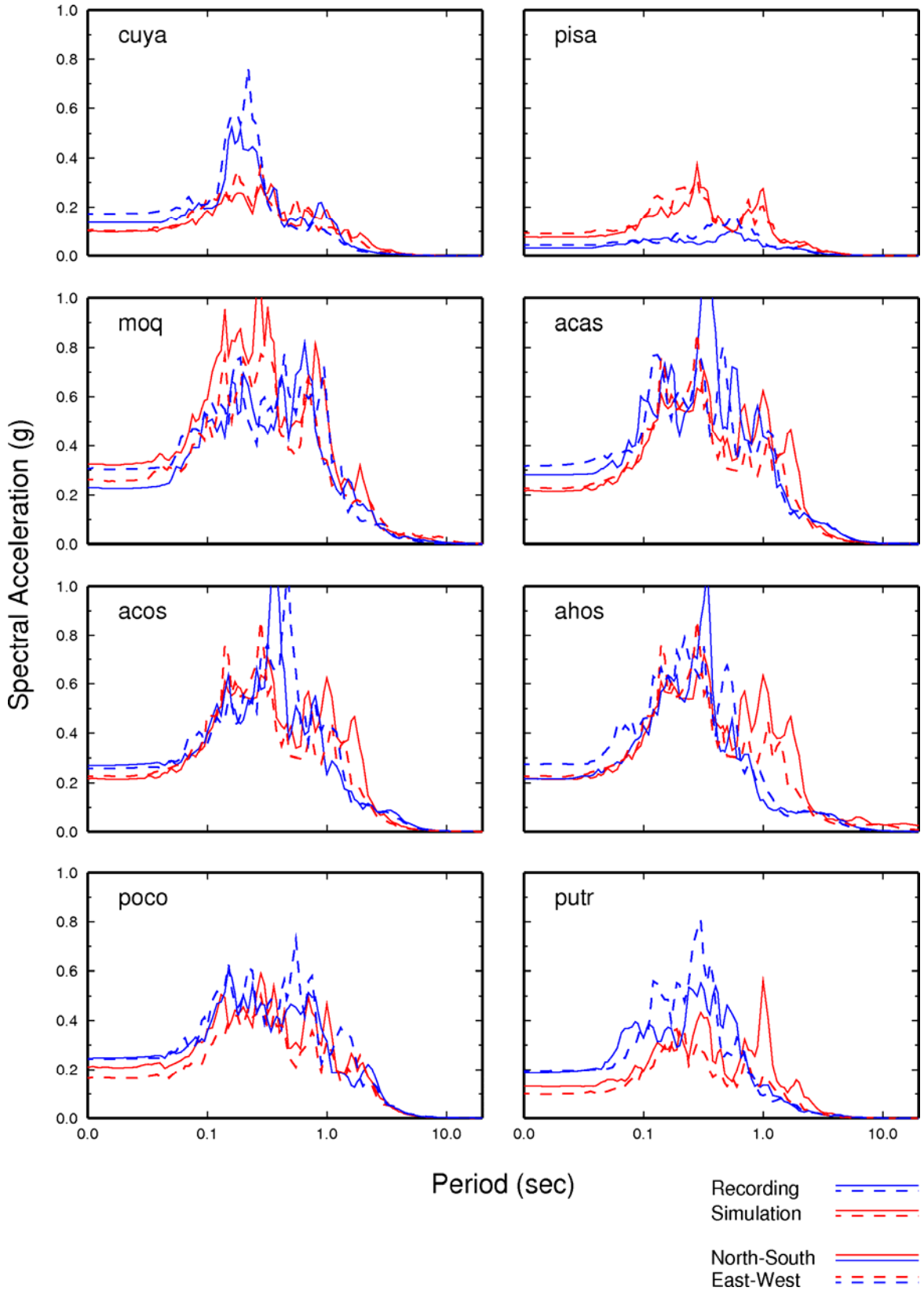

Figure 5. Comparison of recorded and simulated response spectra of the 2001 Arequipa earthquake.

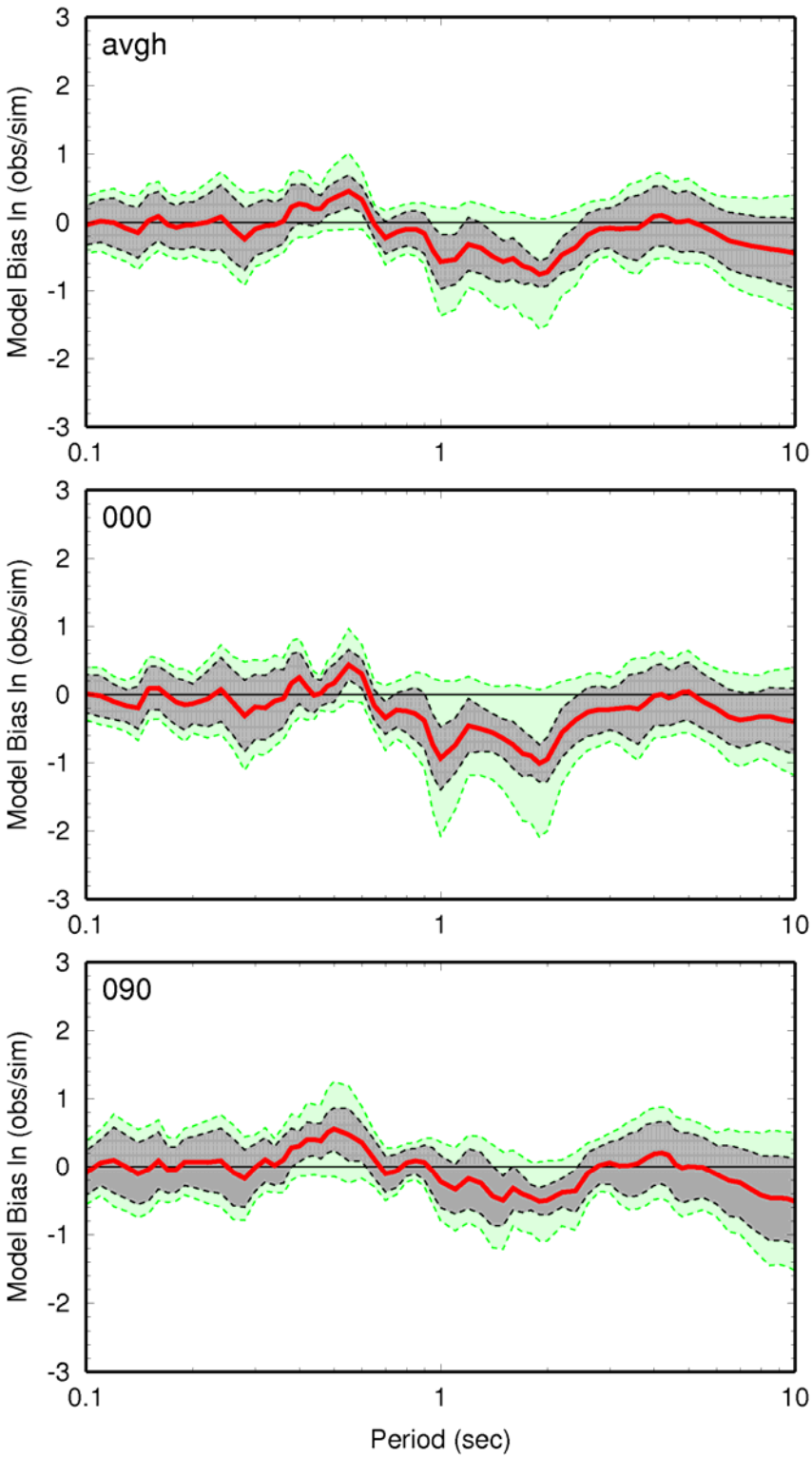

Figure 6. Goodness of fit of recorded and simulated response spectra of the 2001 Arequipa earthquake for average, North and East components. The red line shows the bias; the green zone shows the standard deviation, and the grey zone shows the standard deviation of the mean.

Ground Motion Maps of the 2001 Arequipa Earthquake

The comparisons described above have demonstrated the performance of our strong motion simulation procedure to match the recorded ground motions of the M_w 8.4 Peru earthquake. This forms the basis for generating ground motion maps of the 2001 Arequipa earthquake. Using the simulation procedure described above, we made pairs of ground motion maps for the whole region affected by the earthquake, one for soft rock site conditions (B/C boundary), and another for deep soil site conditions (D). The maps are shown in Figures 7 through 9 for peak acceleration and for spectral acceleration of 0.2, 0.5, 1.0, 2.0 and 5.0 seconds.

The attenuation of ground motion in the southern Peru region is shown in Figures 10 through 15 for peak acceleration and the same response spectral acceleration periods as in Figures 7 through 9. The top two panels of each figure show the attenuation for soft rock site conditions, and the bottom panels show the attenuation for deep soil site conditions. In each pair of figures, the three ground motion models are shown individually in the top panel and their average is shown in the bottom panel. The agreement between the simulations and ground motion models is quite close for peak acceleration and 0.2 seconds spectral acceleration, but at 0.5 seconds the simulations underpredict the models and at 1 and 2 seconds the simulations overpredict the models. Similar trends were found with respect to the strong motion recordings, as shown in Figures 5 and 6.

The average horizontal response spectra of the simulations of the 2001 Arequipa earthquake are compared with three ground motion models in a suite of distance ranges in Figures 16 and 17 for soft rock and deep soil site conditions respectively. The closest agreement is with the Zhao et al. (2006) model, with fairly close agreement with the Youngs et al. (1997) model, and poor agreement with the Atkinson and Boore (2003) model.

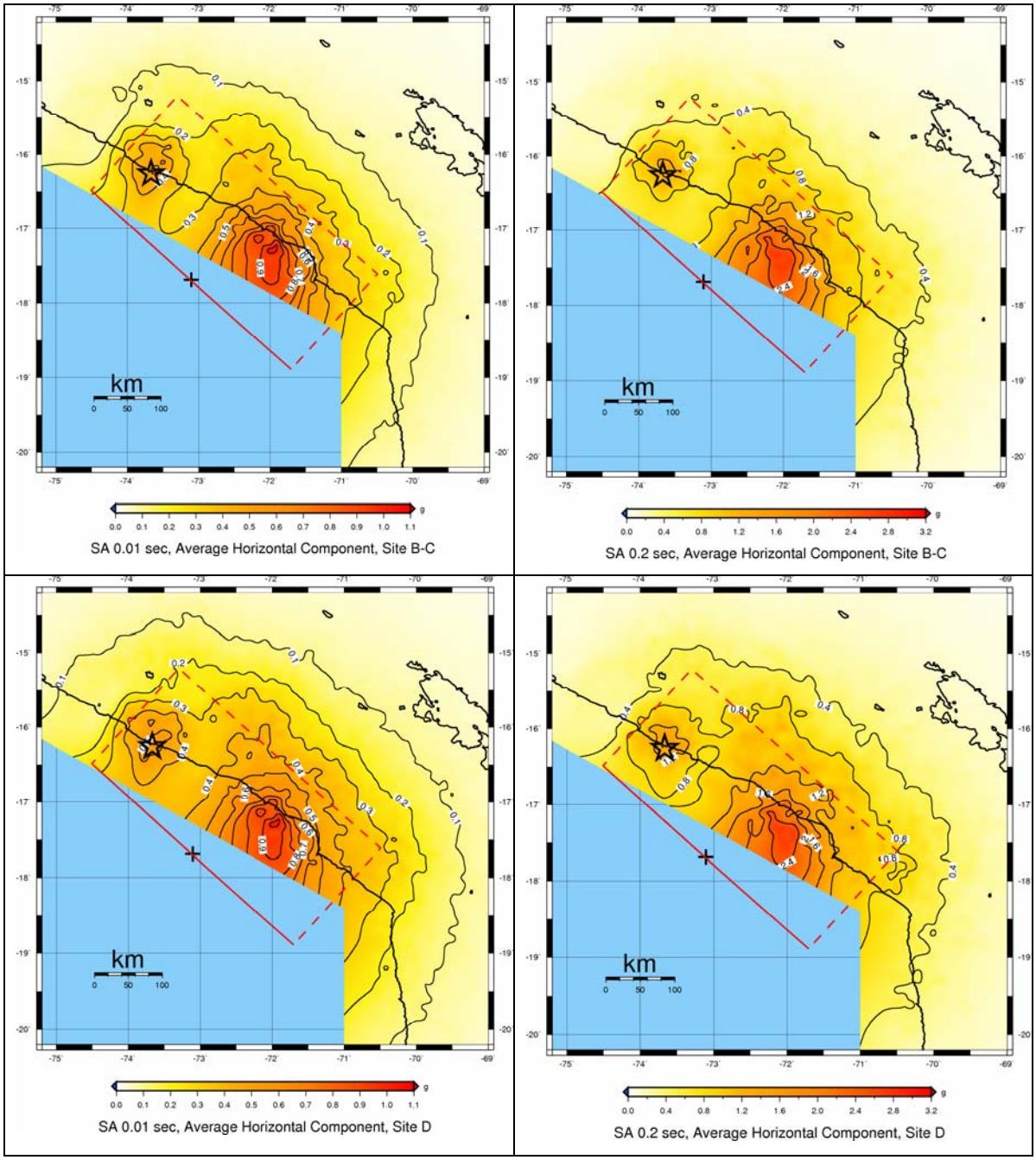

Figure 7. Simulated horizontal peak acceleration map (left) and 0.2 sec spectral acceleration map (right) of the 2001 Arequipa earthquake for soft rock (top) and deep soil (bottom) site conditions.

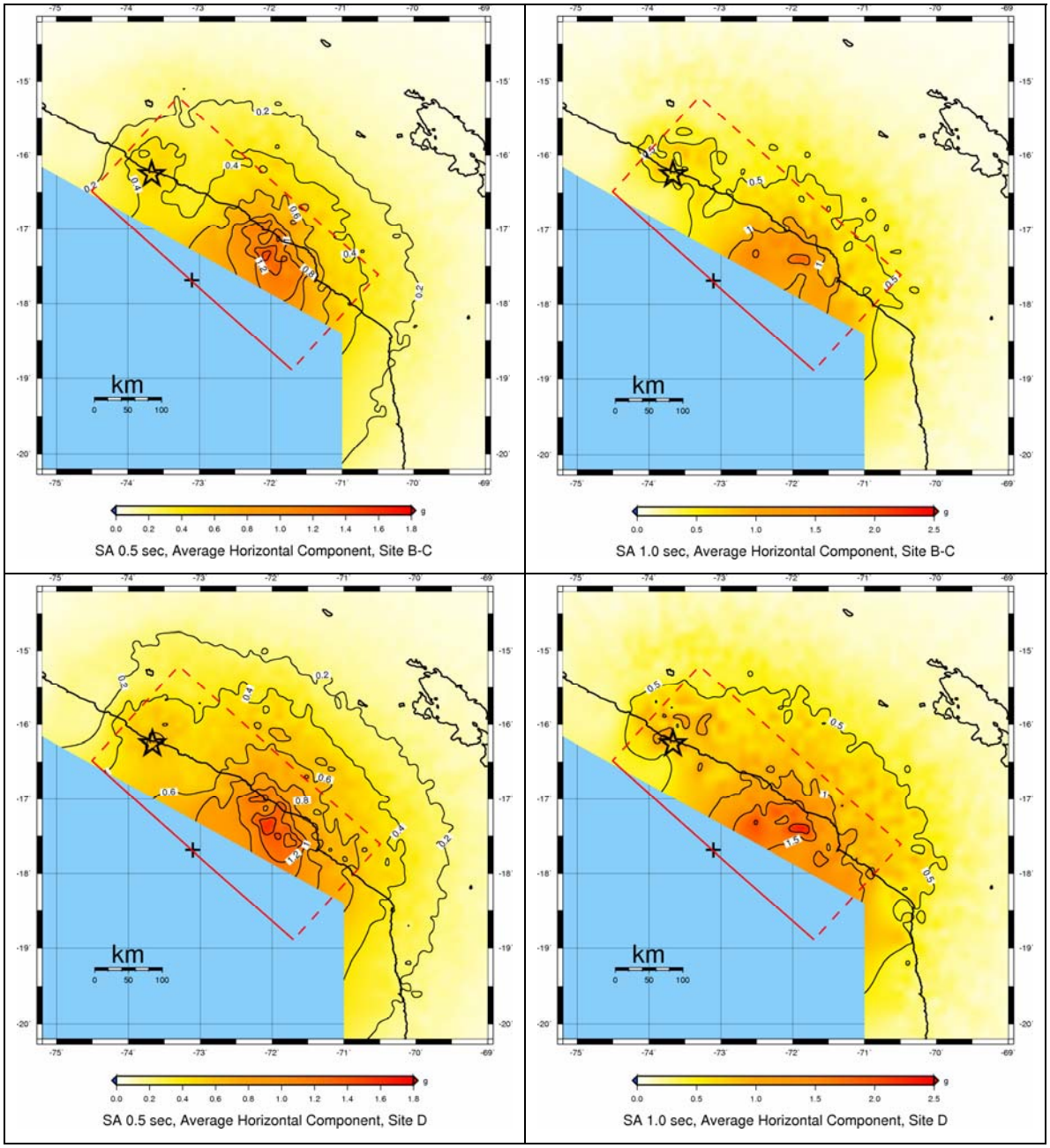

Figure 8. Simulated horizontal 0.5 spectral acceleration map (left) and 1.0 sec spectral acceleration map (right) of the 2001 Arequipa earthquake for soft rock (top) and deep soil (bottom) site conditions.

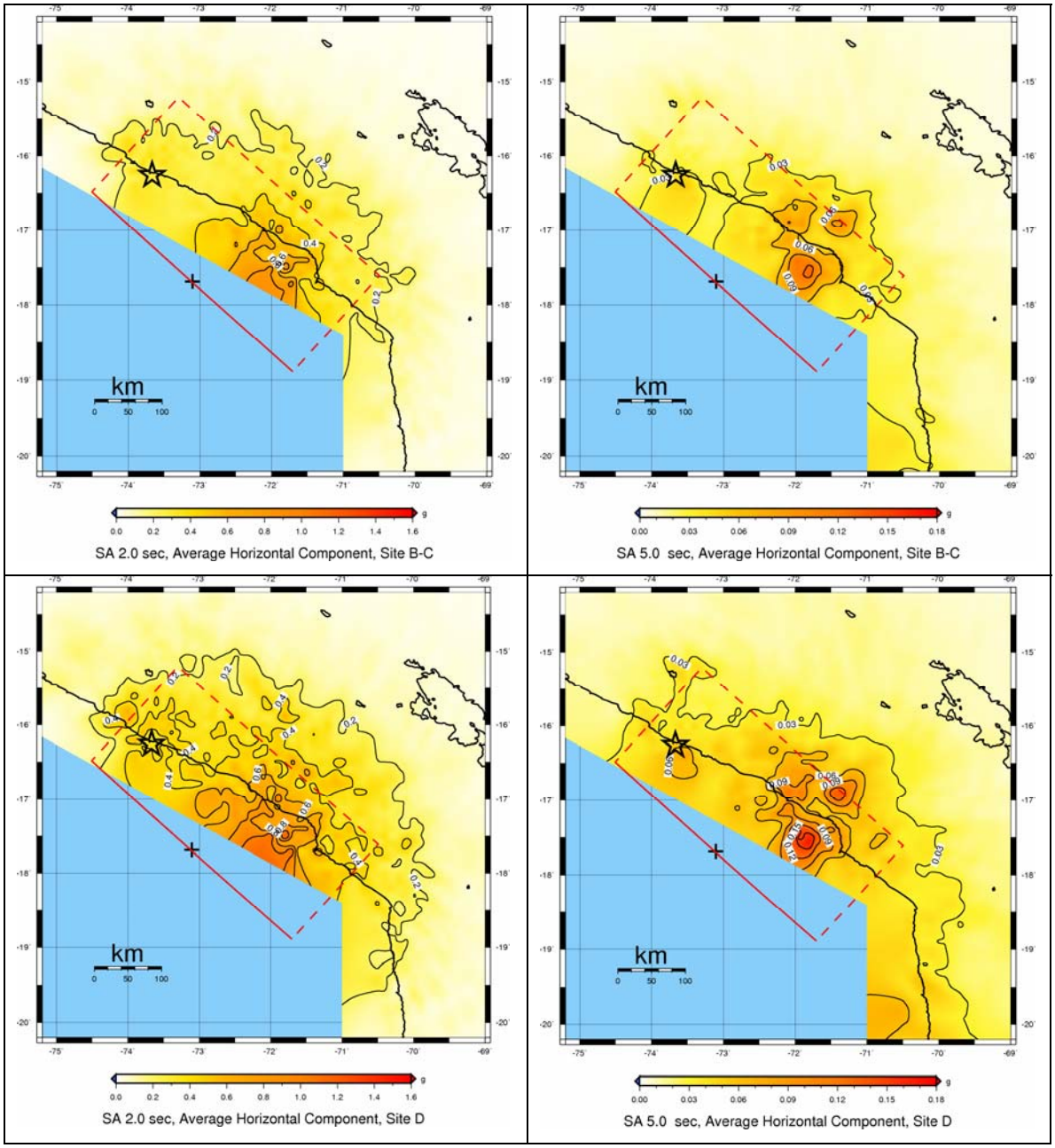

Figure 9. Simulated horizontal 2.0 spectral acceleration map (left) and 5.0 sec spectral acceleration map (right) of the 2001 Arequipa earthquake for soft rock (top) and deep soil (bottom) site conditions.

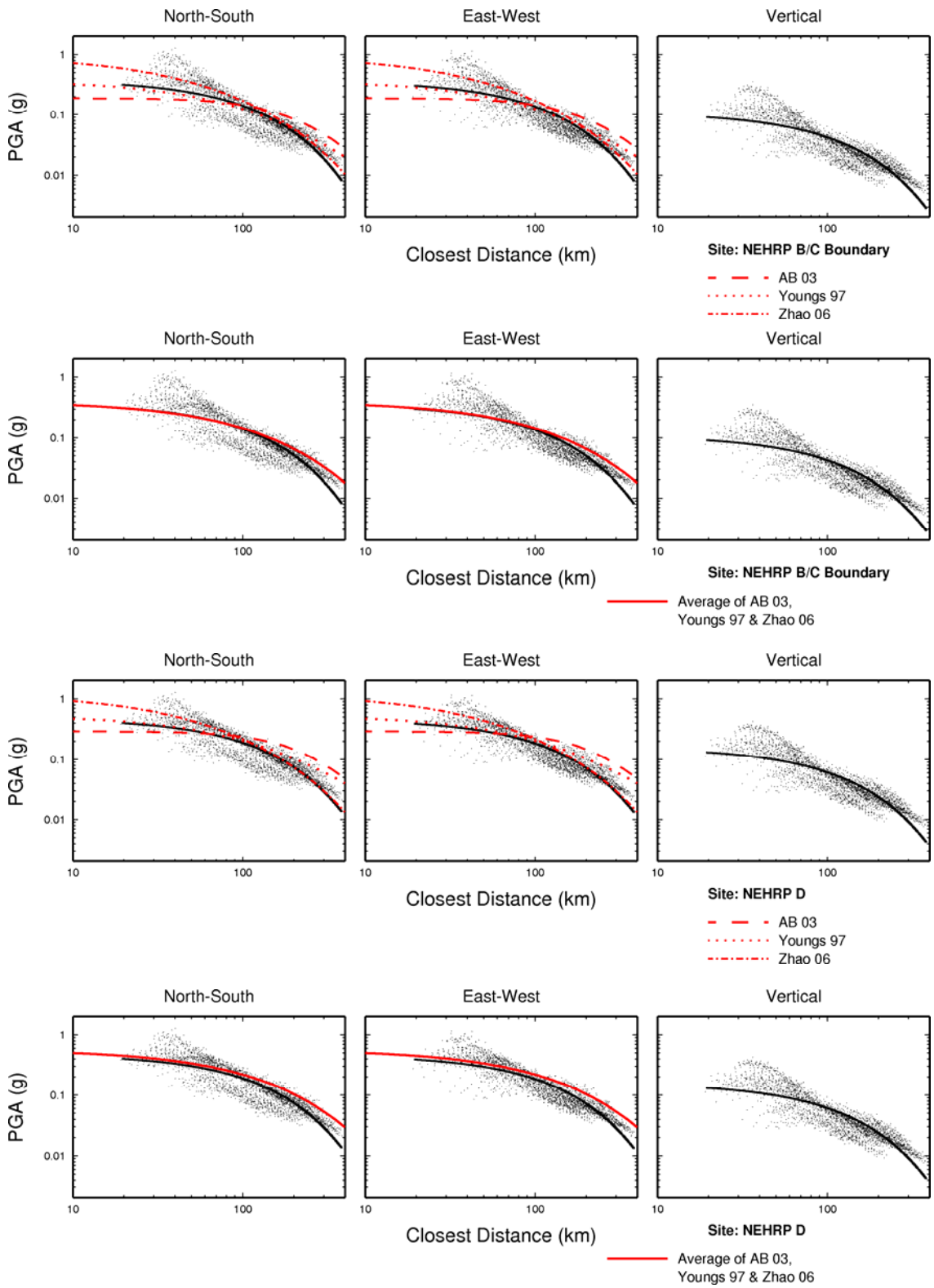

Figure 10. Comparison of simulated peak accelerations with for 2001 Arequipa earthquake with ground motion models

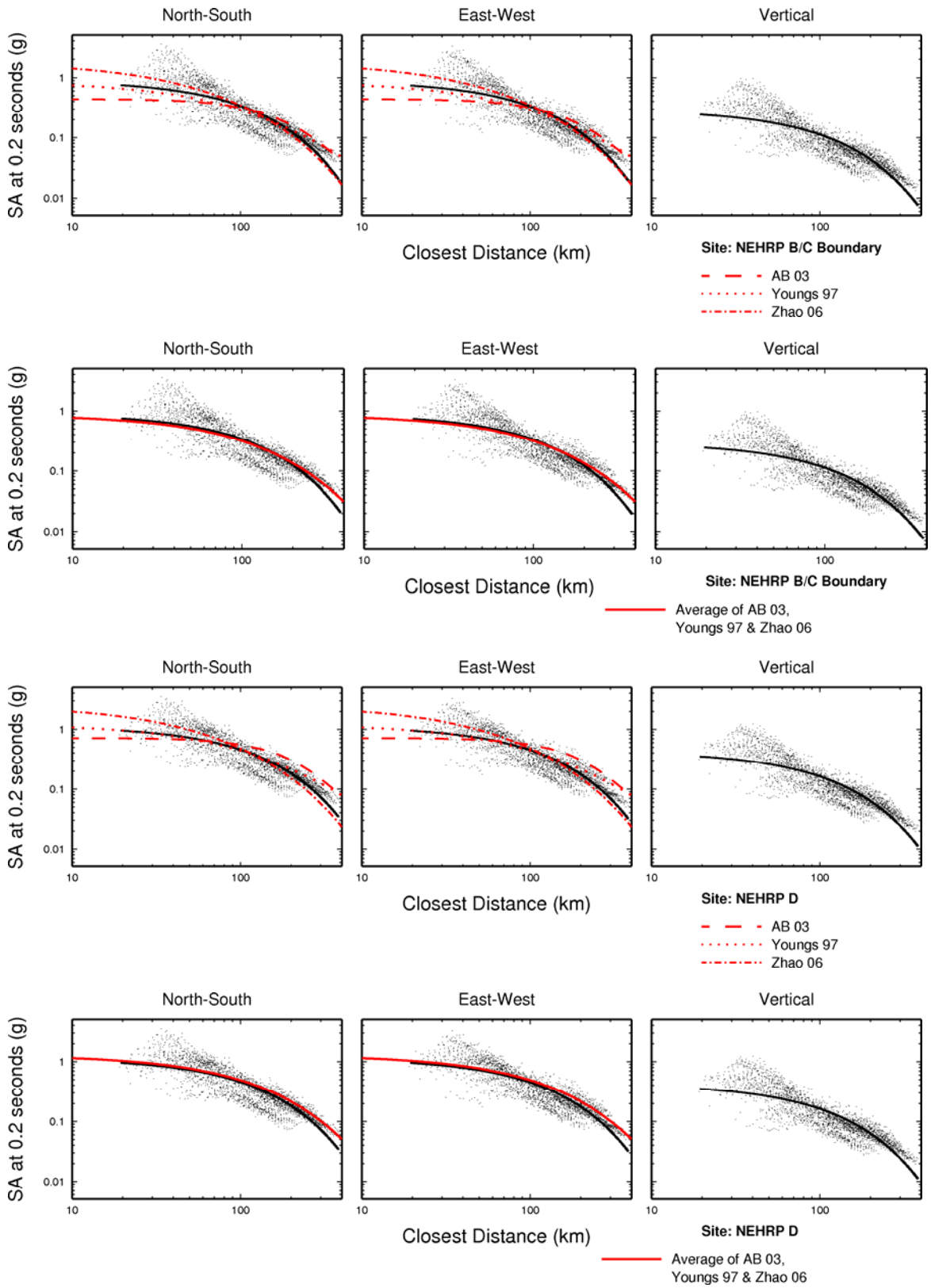

Figure 11. Comparison of simulated 0.2 second spectral accelerations for the 2001 Arequipa earthquake with ground motion models

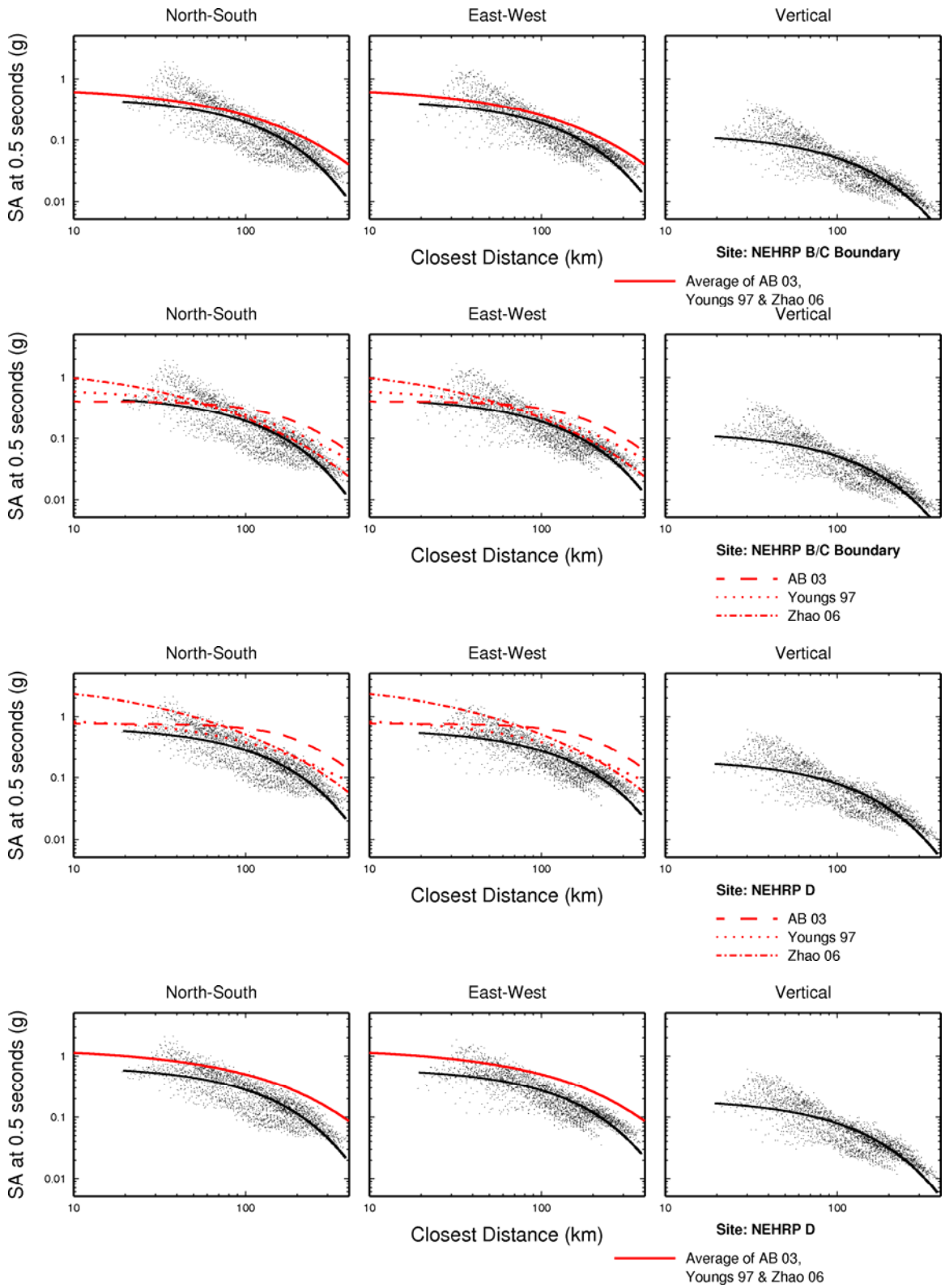

Figure 12. Comparison of simulated 0.5 second spectral accelerations for the 2001 Arequipa earthquake with ground motion models

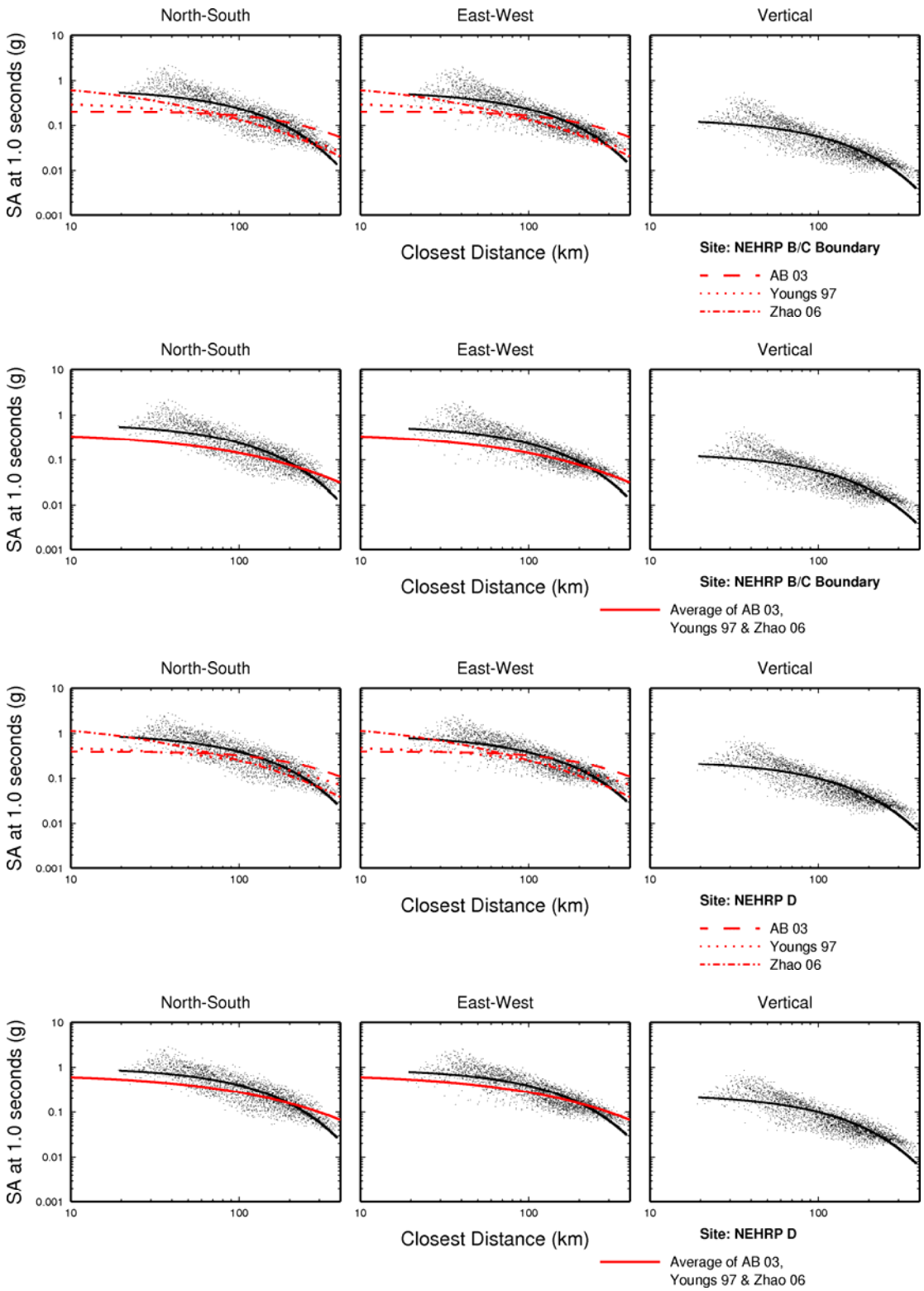

Figure 13. Comparison of simulated 1 second spectral accelerations for the 2001 Arequipa earthquake with ground motion models

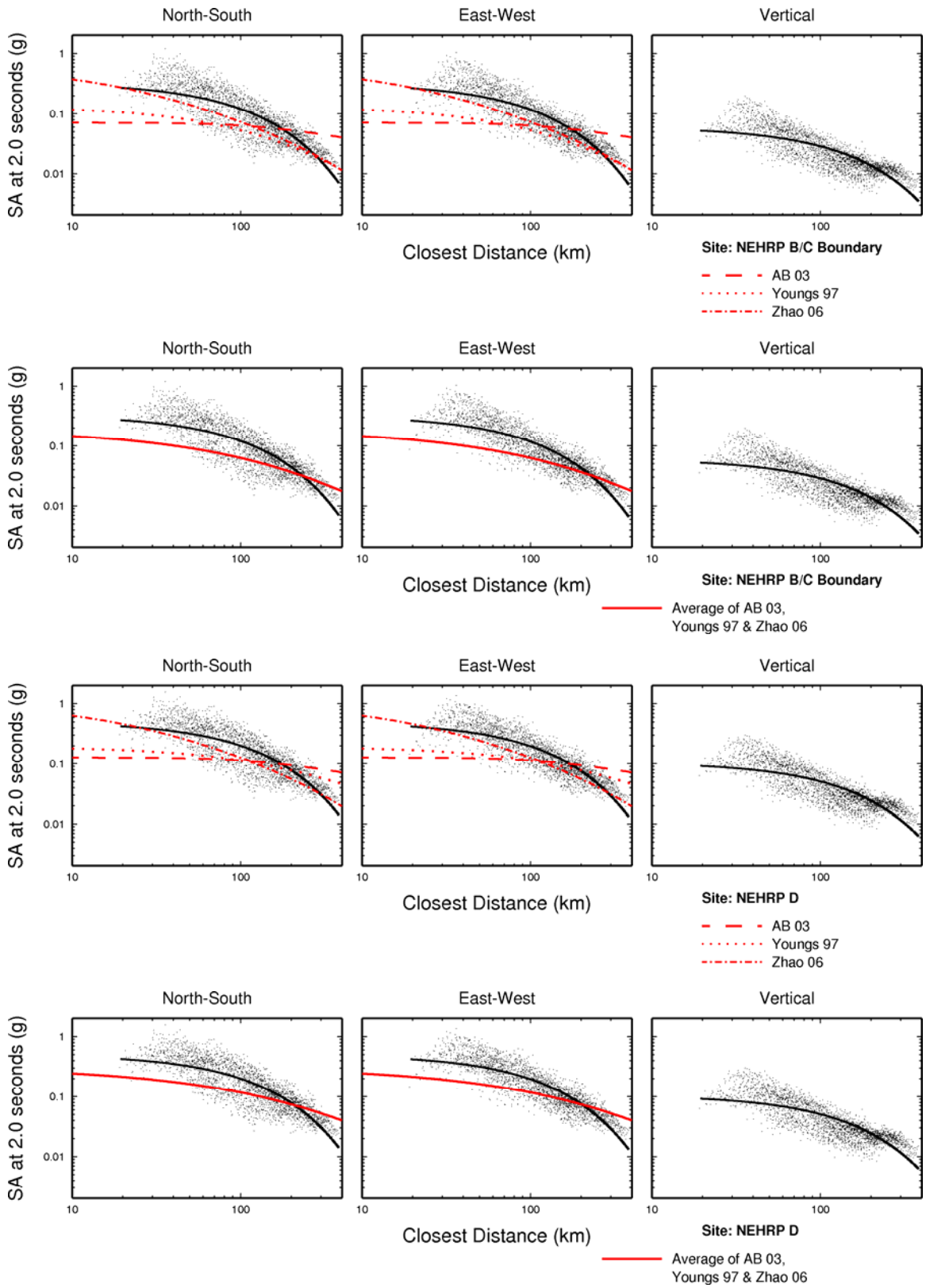

Figure 14. Comparison of simulated 2 second spectral accelerations for the 2001 Arequipa earthquake with ground motion models

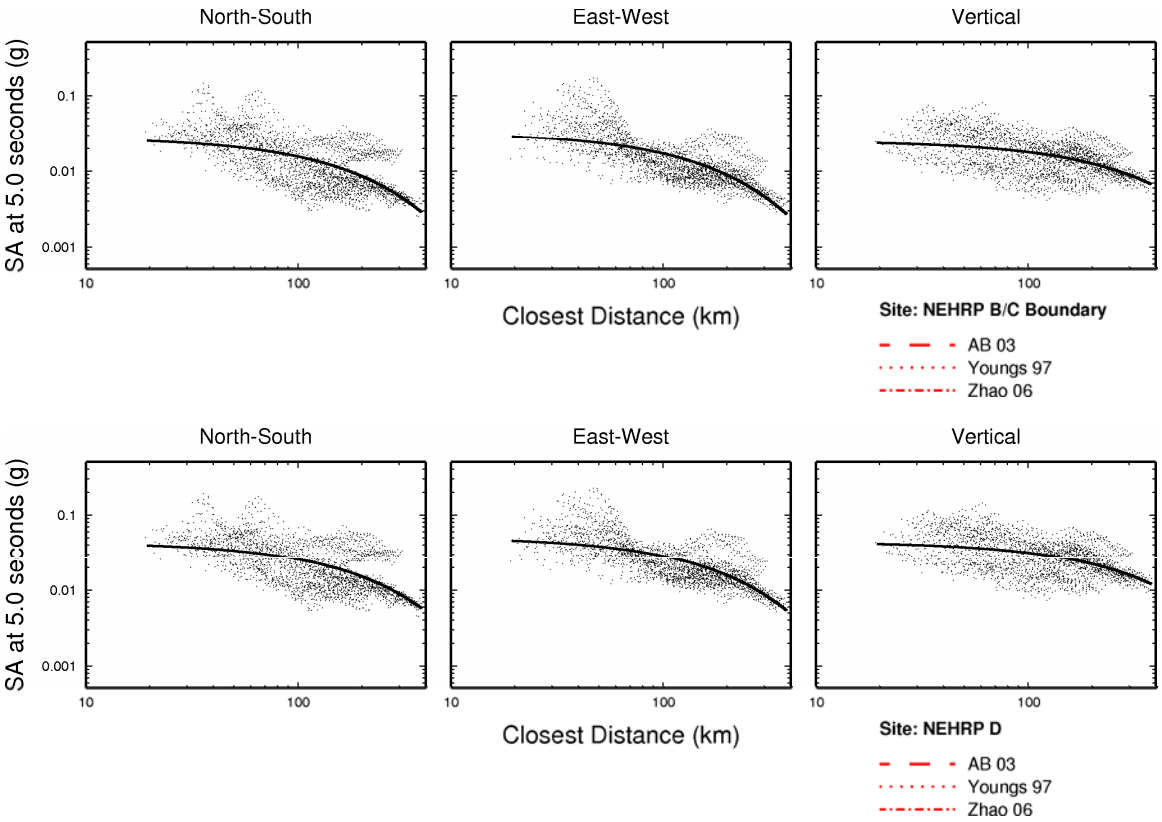

Figure 15. Simulated 5 second spectral accelerations for the 2001 Arequipa earthquake.

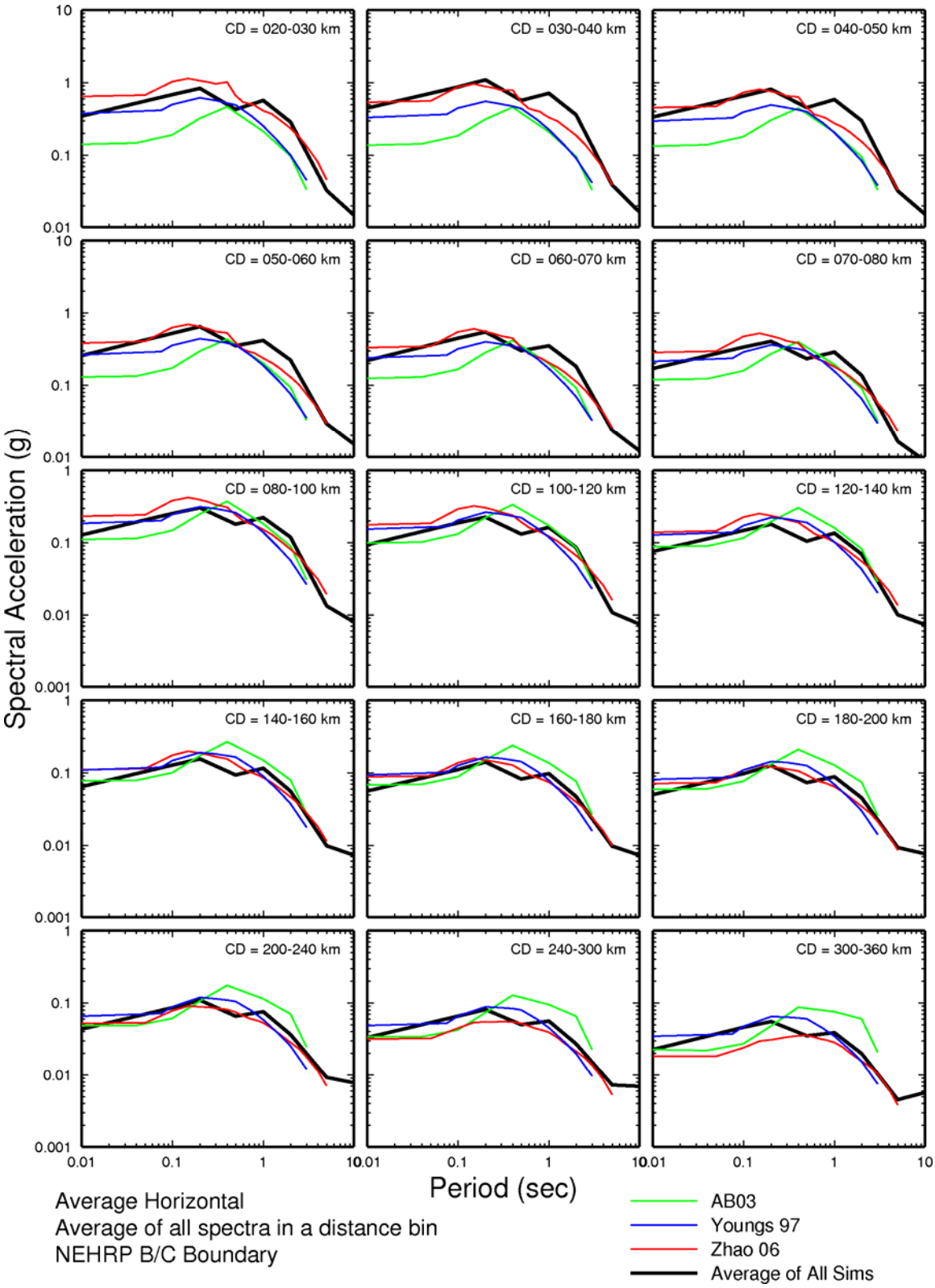

Figure 16. Comparison of average horizontal simulated response spectra for a suite of distance ranges for the 2001 Peru earthquake for soft rock (B/C boundary) site conditions with three ground motion models

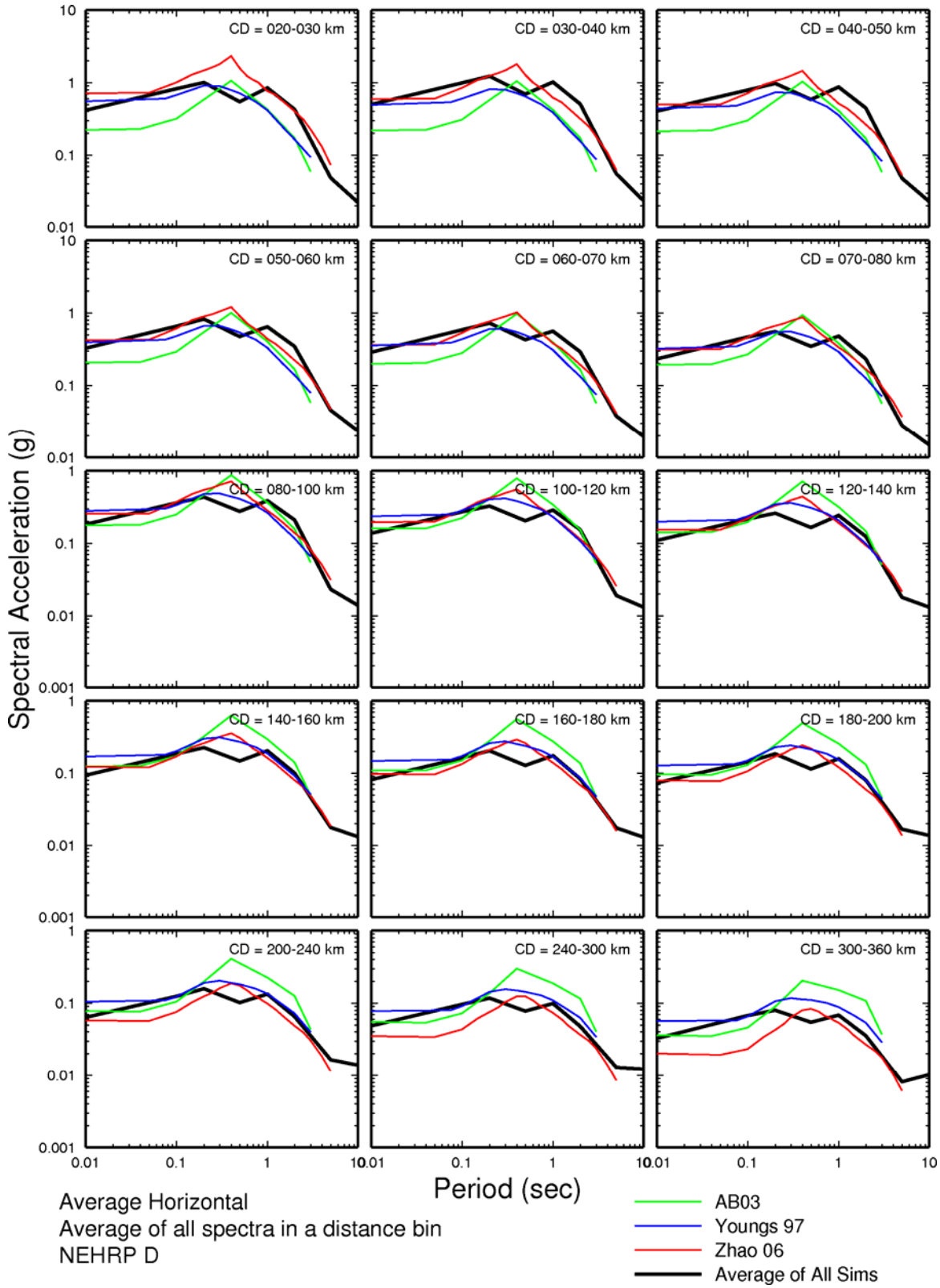

Figure 17. Comparison of average horizontal simulated response spectra for a suite of distance ranges for the 2001 Peru earthquake for deep soil (D) site conditions with three ground motion models

EARTHQUAKES THAT RUPTURE THE ENTIRE CASCADIA SUBDUCTION ZONE

Earthquake Source Characterization

This section of the report describes the modeling of subduction earthquakes that rupture the entire Cascadia subduction zone. The geometry of the Cascadia earthquake source models used in this report was based on the source characterization of Petersen et al. (2008). In particular, we used their "base" model of the bottom of the seismogenic plate interface, shown in Figure 18, to which they gave a weight of 0.5. This model is based on the global observation that rupture usually extends down to depths of about 30 km. Petersen et al (2008) gave weights of 0.1, 0.2 and 0.2 to the alternative models "top," "middle," and "bottom" respectively, which are also shown in Figure 18. The sensitivity of the calculated seismic hazard to uncertainty in the model for the bottom of the seismogenic zone was analyzed by Petersen et al. (2002). This depth controls the eastern extent of the subduction zource, and thus has a strong influence on ground motion levels in the urban regions of Washington and Oregon, which mainly lie to the east of the source.

The fault geometry used to represent the base model is shown in Figure 19. The subduction interface was divided into three segments to accommodate the shallower dip at the bend in the subduction zone near the Olympic Peninsula. The shallower segment has a downdip width of 160 km while the other segments have downdip widths of 120 km. The rupture area of the combined fault segments is 131,500 square km.

Petersen et al. (2008) assume that such earthquakes have magnitudes in the range of 8.8 to 9.2, with a weight of 0.6 given to magnitude 9.0, and weights of 0.2 given to magnitudes of 8.8 and 9.2. However, the relations between seismic moment and rupture area of subduction earthquakes derived by Somerville et al. (2002) from the rupture models of past earthquakes predict that the magnitude corresponding to a rupture area of 131,500 square km is Mw 8.7. Accordingly, we performed ground motion simulations for earthquakes having Mw 8.7. To test the sensitivity of the ground motions to uncertainty in the magnitude of the earthquake, we also assigned magnitudes of 8.4 and 9.0 to this earthquake source. The source parameters of these earthquakes, listed in Table 3, do not conform to the self-similar scaling relations of Somerville et al. (2002). Specifically, their rupture areas are twice and half as large respectively, and their average displacements are half and twice as large respectively, than those of Mw 8.4 and 9.0 earthquakes that do conform to the Somerville et al. (2002) scaling relations, listed in Table 4.

Table 3. Source Parameters of Modeled Mw 8.4, 8.7 and 9.0 Earthquakes that all Rupture the Whole Cascadia Subduction Zone (Not Self Similar)

Mw	Rupture Area (sq km)	Average Slip (cm)	Rise Time (sec)	Slip Velocity (cm/sec)
8.4	131,500	106	6.4	16.5
8.7	131,500	297	9.0	33.0
9.0	131,500	831	12.7	66.0

Table 4. Source Parameters of Mw 8.4, 8.7 and 9.0 Earthquakes that Conform to the Self-Similar Scaling relations of Somerville et al. (2002)

Mw	Rupture Area (sq km)	Average Slip (cm)	Rise Time (sec)	Slip Velocity (cm/sec)
8.4	65,750	212	6.4	33.0
8.7	131,500	297	9.0	33.0
9.0	263,000	416	12.7	33.0

For each of the three events listed in Table 3, we generated earthquake rupture models for three hypocentral locations: south, central and north. The rupture models of the three Mw 8.7 events are shown in Figure 20, the rupture models of the three Mw 9.0 events are shown in Figure 21, and the rupture models of the three Mw 8.4 events are shown in Figure 22. The rupture models of the Mw 8.7 earthquakes conform to the self-similar scaling relations of Somerville et al. (2002), but the rupture models of the Mw 9.0 and Mw 8.4 earthquakes do not. The average slip of the Mw 9.0 earthquake is twice that predicted by the Somerville et al. (2002) scaling relations, and the average slip of the Mw 8.4 earthquake is half.

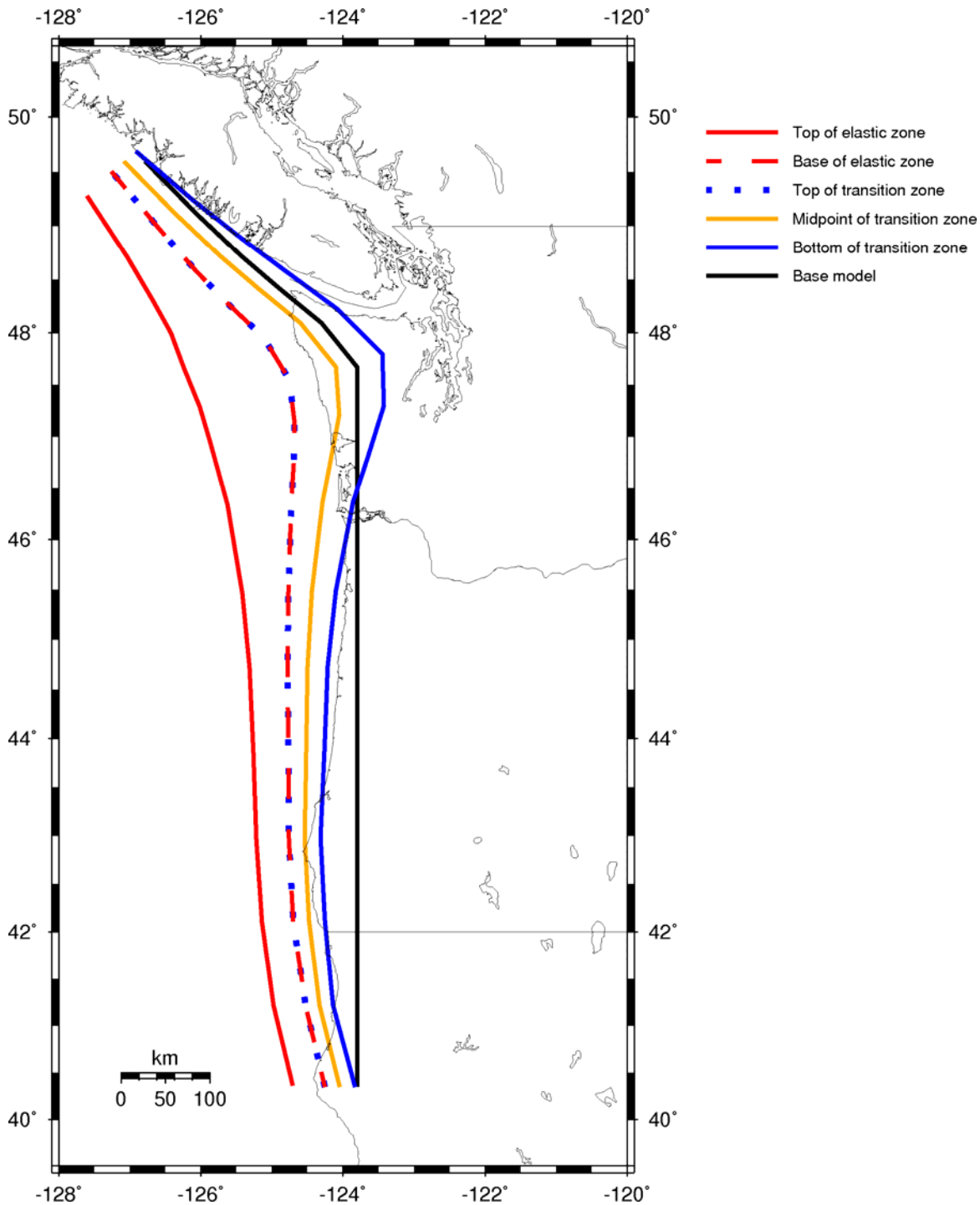

Figure 18. Alternative models of the downdip extent of the Cascadia subduction zone. Source: Petersen et al. (2008). This study used the base model based on global data, shown by the thick black line.

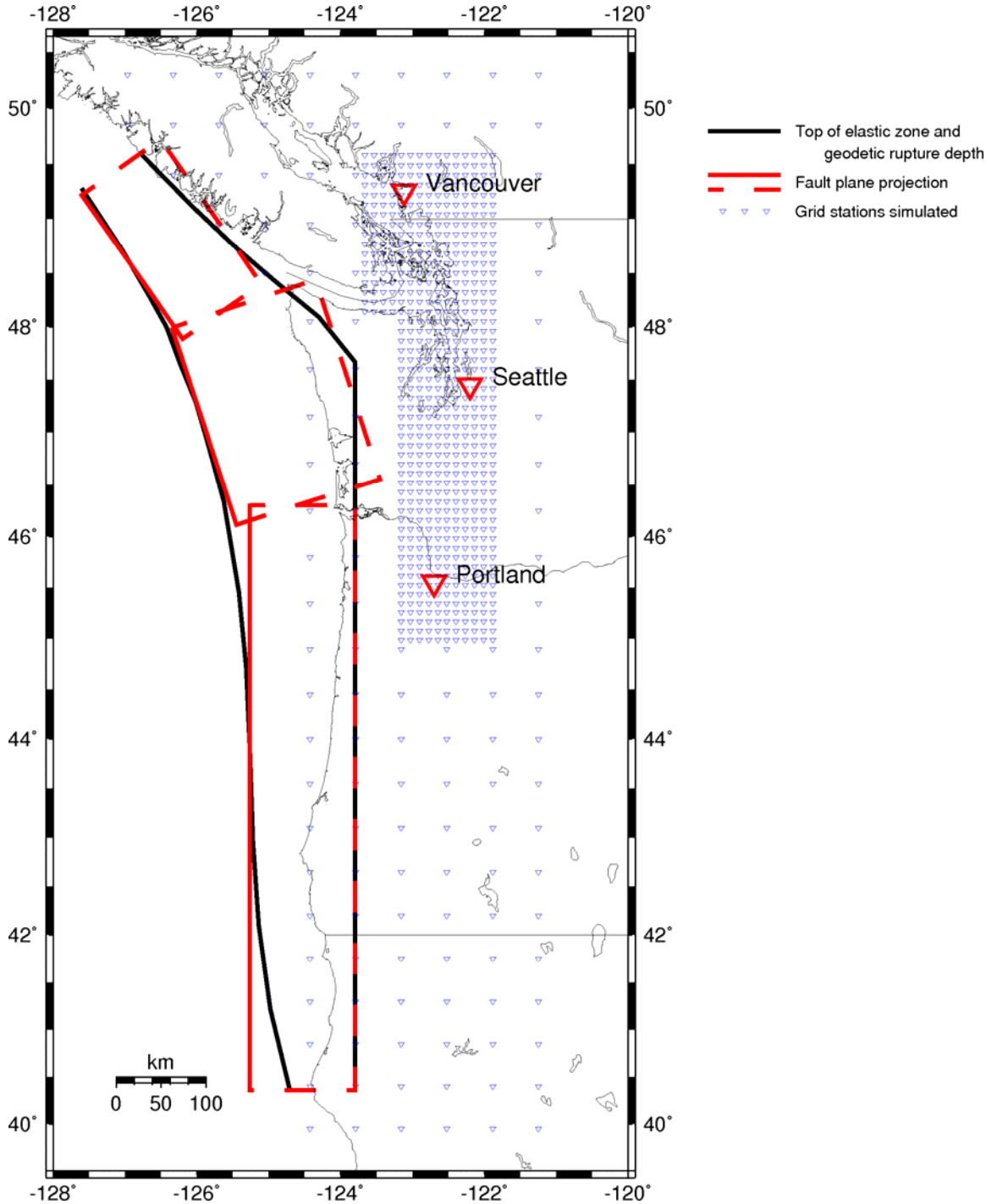

Figure 19. Modeled rupture geometry of the Cascadia subduction zone and the grid of stations used for strong motion simulation (blue triangles).

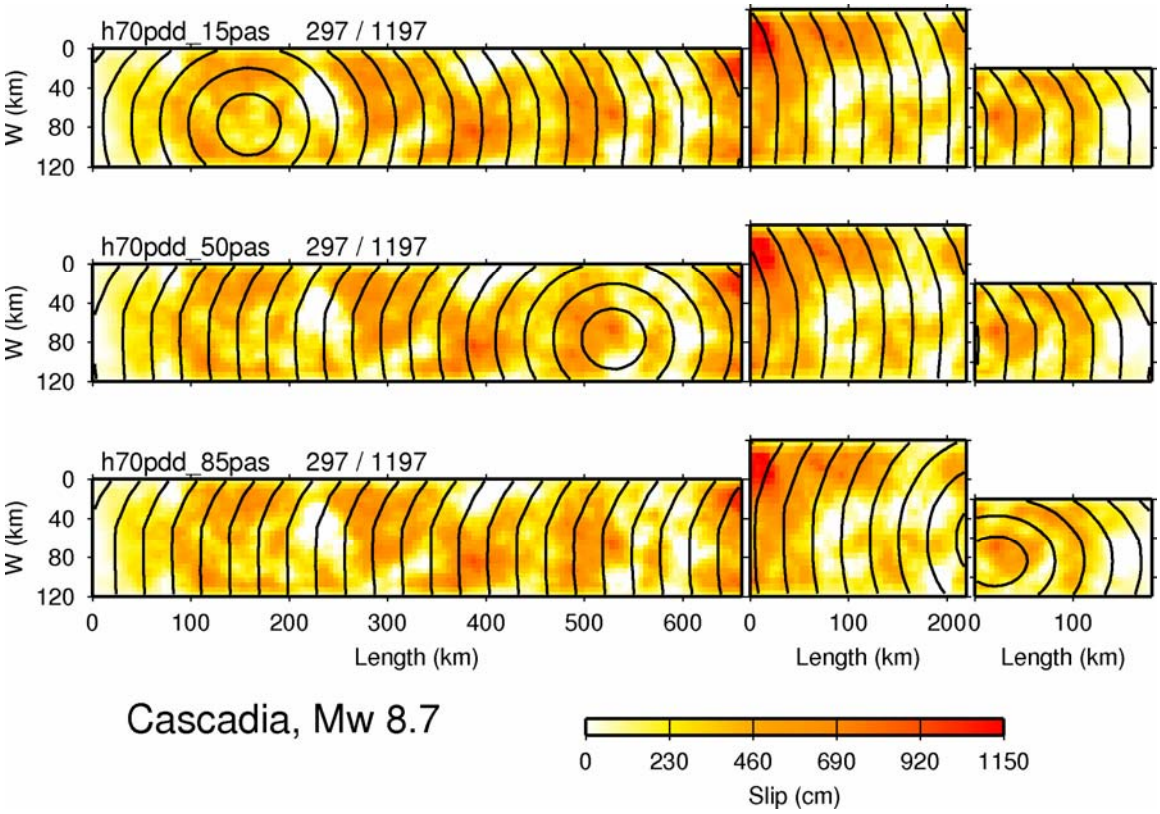

Figure 20. Rupture models of three Mw 8.7 scenario earthquakes on the Cascadia subduction zone with southern (top), central (middle), and northern (bottom) hypocenters. The average slip is 297 cm and the maximum slip is 1197 cm. These rupture models conform to the self-similar scaling relations of Somerville et al. (2002).

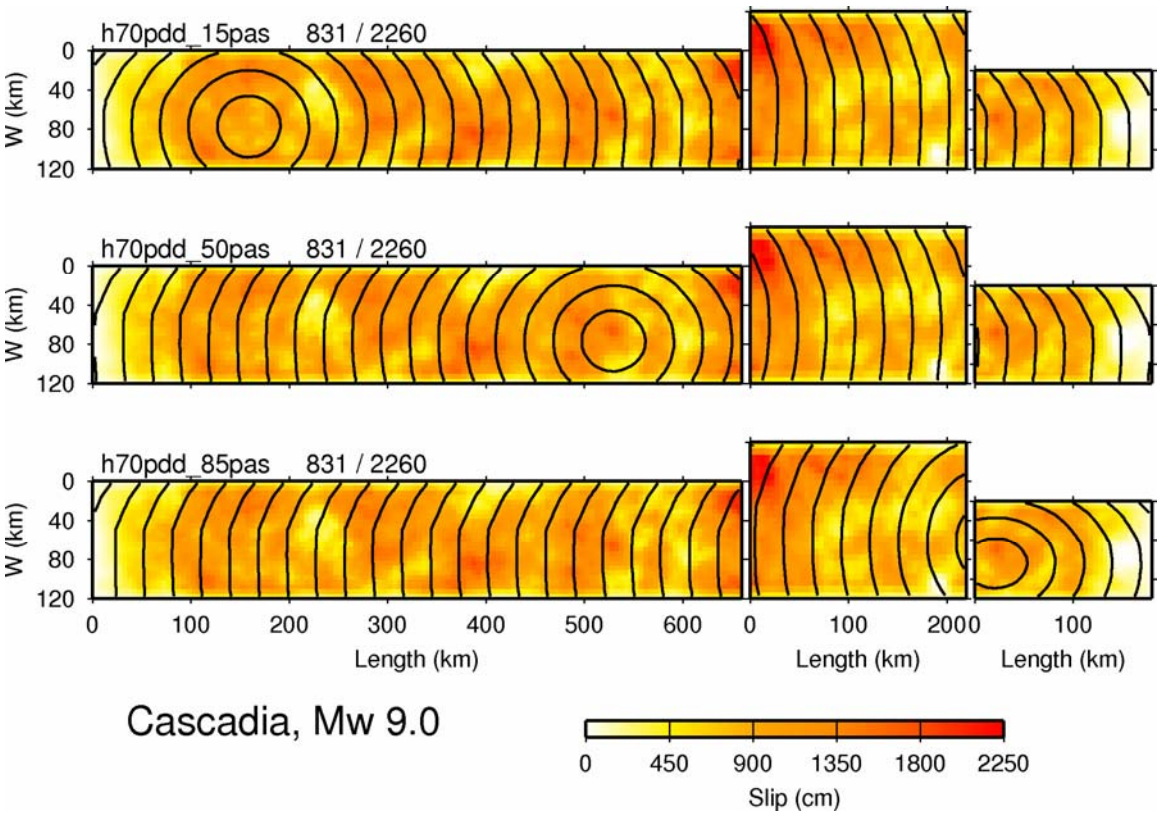

Figure 21. Rupture models of three Mw 9.0 scenario earthquakes on the Cascadia subduction zone with southern (top), central (middle), and northern (bottom) hypocenters. The average slip is 831 cm and the maximum slip is 2260 cm. These rupture models do not conform to the self-similar scaling relations of Somerville et al. (2002).

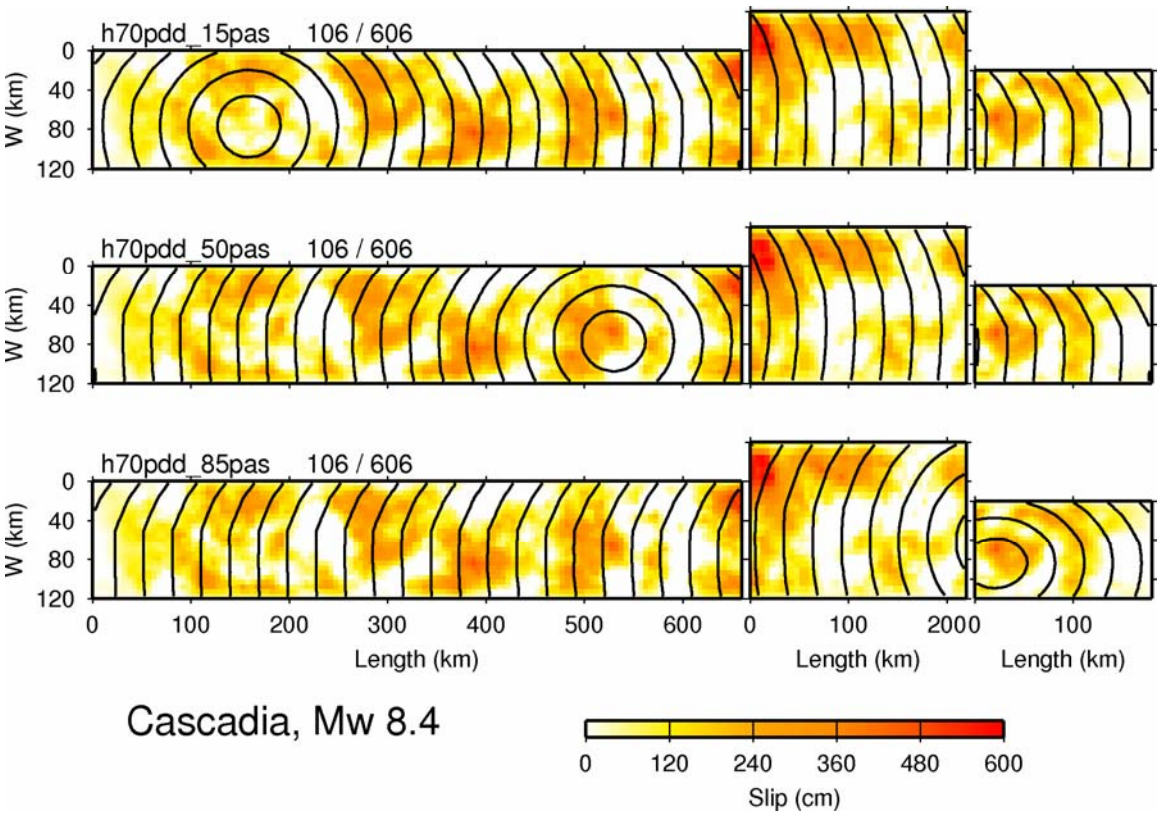

Figure 22. Rupture models of three Mw 8.4 scenario earthquakes on the Cascadia subduction zone with southern (top), central (middle), and northern (bottom) hypocenters. The average slip is 106 cm and the maximum slip is 606 cm. These rupture models do not conform to the self-similar scaling relations of Somerville et al. (2002).

Crustal Structure

In a previous study in which we simulated the ground motions of Cascadia subduction earthquakes, we demonstrated the adequacy of Green's functions computed using a series of 1D approximations to a 2D seismic velocity model of the Cascadia subduction zone by comparing the 1D and 2D Green's functions (Cohee et al., 1991). The 2D model used a simple model of the subcrustal structure from the Lithoprobe transect (Clowes et al., 1987). Subsequent work by Brocher et al. (2003) and McNeill et al. (2004) indicates the presence of a serpentinized forearc upper mantle along the Cascadia margin. This forearc has significantly lower seismic velocities than those of Clowes et al. (1987) used in the ground motion study by Cohee et al. (1991).

McNeill et al. (2004) analyzed the effect of a serpentinized forearc upper mantle along the Cascadia margin on ground motions from megathrust earthquakes, and concluded that it has a relatively minor effect. It alters the distance range over which postcritically reflected S waves dominate by shifting the reflecting interface from the continental Moho to the oceanic Moho, but does not significantly affect the amplitudes. Accordingly, we conclude that it is not critical to use full 2D or 3D Green's functions in our simulations, and so we used Green's functions computed using a 1D approximation to the velocity model of the Cascadia subduction zone. We found that the velocity model we used for Peru is broadly compatible with the velocity model for Cascadia described McNeill et al. (2004). This velocity model, which has velocities that are considerably lower than those used by Cohee et al. (1991), is shown in Table 5.

Table 5. Crustal structure model for Cascadia.

Vp	Qp	Vs	Qs	Density	Thickness
2.600	2000	1.500	900.000	2.000	0.200
5.300	2000	3.030	900.000	2.100	6.700
6.000	2000	3.370	900.000	2.500	4.600
6.500	2000	3.650	900.000	2.780	18.100
7.300	2000	4.100	900.000	3.180	15.800
8.100	2000	4.500	900.000	3.400	16.000
8.101	2000	4.501	900.000	3.401	100.000

Another important influence on the amplitude and durations on strong ground motions is the effect of sedimentary basins, such as the Puget Trough and the Portland and Tualatin basins. We have addressed basin response in these locations in other studies (Ichinose, 2003b; Pitarka et al., 2002), and recognize that this is an important issue to be addressed in future studies, but it lies beyond the scope of this report.

Ground Motion Maps

We performed ground motion simulations at the stations shown by the grid in Figure 19. We then generated ground motion maps for each of the three rupture scenarios for each of the three earthquake magnitudes. The rupture models of the Mw 8.7 earthquakes conform to the self-similar scaling relations of Somerville et al. (2002), but the rupture models of the Mw 9.0 and Mw 8.4 earthquakes do not. The average slip of the Mw 9.0 earthquake is twice that predicted by the Somerville et al. (2002) scaling relations, and the average slip of the Mw 8.4 earthquake is half. We consider that the simulated ground motions of the Mw 9.0 and Mw 8.4 earthquakes approximately represent upper and lower "bounds" (plus and minus two standard deviations) on the ground motions for

earthquakes that rupture the entire Cascadia subduction zone. The maps for the Mw 8.7 earthquake represent an estimate of the median ground motion levels.

The maps, shown in Figures 23 through 34, are for peak acceleration and response spectral acceleration at 0.2, 0.5, 1.0, 2.0, and 5.0 seconds for each of two site conditions: soft rock (NEHRP B/C) and deep soil (NEHRP D). The particular slip distribution of the earthquake rupture model has a significant impact on the distribution of ground motion along the coast in the border region between Oregon and Washington. This pattern would be smoothed out if a large number of simulations were done. Also, the spectral shape of the empirical source function used in the simulation procedure has an impact on the simulated ground motions, as illustrated in Figures 5 and 6.

Ground Motion Attenuation

The attenuation of ground motion with distance derived from the strong motion simulations is shown in four sets of figures. The first set, Figures 35 – 40, compares the simulated ground motion values and a simple model that is fit to those values (shown by a solid black line) with the three ground motion models. The simulated response spectral values for the three different hypocentral locations are shown in different colors. The second set, Figures 41 – 46, compares the simulated ground motion values and a simple model that is fit to those values (shown by a solid black line) with the average of the three ground motion models. The third set, Figures 47 – 52, compares the simple models fit to the simulated ground motion values with the three ground motion models. The fourth set, Figures 53 – 58, compares the simple models fit to the simulated ground motion values with the average of the three ground motion models.

From the first set of Figures (35 – 40), it is clear that there are very large differences between the three ground motion models, especially in the slopes of the attenuation curves, which mainly affect the ground motion estimates at close distances where data are sparse. Of the simulations for the three earthquake magnitudes, the magnitude 8.7 Cascadia earthquake generally predicts values close to the average of the three ground motion models, which is expected because that magnitude is the only one of the three that conforms to the Somerville et al. (2002) scaling relations. This can be seen more clearly in Figures 41 – 46, which compare the simulations with the average of the three ground motion models. The simulations tend to underpredict the three ground motion models at a period of 0.5 seconds and overpredict the three ground motion models at periods of 1 and 2 seconds. This is consistent with the tendency of the simulations to underpredict and overpredict the strong motion recordings of the 2001 Arequipa earthquake in the respective period ranges (Figure 6).

The simulations of the magnitude 9.0 earthquake generally overpredict the three models, which is expected because the average slip of that event is twice that of the Somerville et al. (2002) scaling relations, which would to result in an overprediction by a factor of two. Similarly, the simulations of the magnitude 8.4 earthquake generally underpredict the three models, which is expected because the average slip of that event is half that of the Somerville et al. (2002) scaling relations, which would result in an underprediction by a factor of two. We consider that the simulated ground motions of the Mw 9.0 and Mw 8.4 earthquakes approximately represent upper and lower “bounds”

(plus and minus two standard deviations) on the ground motions for earthquakes that rupture the entire Cascadia subduction zone.

In Figures 47 – 58, we compare the simulated ground motions, represented by the fitted curves, with the three ground motion models. These figures compare all three earthquake magnitudes in the same panel, and show simulation results for different hypocenter locations in separate panels. Figures 47 – 52 provide comparisons with the three individual ground motion models, and Figures 53 – 58 provide comparisons with the average of the three.

All three models have magnitude scaling that is small at short periods and increases at longer periods. This scaling is much smaller than the magnitude scaling of the simulations, because the simulations do not portray realistic magnitude scaling based on the Somerville et al. (2002) model. As described above, the rupture models of the Mw 8.7 earthquakes conform to the self-similar scaling relations of Somerville et al. (2002), but the rupture models of the Mw 9.0 and Mw 8.4 earthquakes do not. The average slip of the Mw 9.0 earthquake is twice that predicted by the Somerville et al. (2002) scaling relations, and the average slip of the Mw 8.4 earthquake is half. We consider that the simulated ground motions of the Mw 9.0 and Mw 8.4 earthquakes approximately represent upper and lower "bounds" (plus and minus two standard deviations) on the ground motions for earthquakes that rupture the entire Cascadia subduction zone. The ground motions of the Mw 8.7 earthquake represent an estimate of the median ground motion levels.

From Figures 53 – 58, we see that the simulations of the Mw 8.7 earthquake are generally consistent with the average of the three ground motion models. As noted above, the simulations tend to underpredict the three ground motion models at a period of 0.5 seconds and overpredict the average of the three ground motion models at periods of 1 and 2 seconds. This is consistent with the tendency of the simulations to underpredict and overpredict the strong motion recordings of the 2001 Arequipa earthquake in the respective period ranges (Figure 6).

The response spectra of the simulations of the Mw 8.7 Cascadia earthquakes are compared with the three ground motion models in a suite of distance ranges in Figures 59 and 60 for soft rock and deep soil site conditions respectively. There is fairly close agreement for the Youngs et al. (1997) model, with moderate agreement for the Zhao et al. (2006) model and less agreement with the Atkinson and Boore (2003) model.

The response spectra of the simulations of the Mw 9.0 and Mw 8.4 Cascadia earthquakes are compared with the three ground motion models in a suite of distance ranges in Figures 61 through 64 for soft rock and deep soil site conditions respectively. The large differences between the model response spectra and the Mw 9.0 and 8.4 Cascadia earthquake simulations are as expected from the factor of two difference in average slip compared with the Somerville et al. (2002) scaling relations, as described above. We consider that the simulated ground motions of the Mw 9.0 and Mw 8.4 earthquakes approximately represent upper and lower "bounds" (plus and minus two standard deviations) on the ground motions for earthquakes that rupture the entire Cascadia subduction zone.

We averaged the simulations over the three hypocenter locations and the two horizontal components to obtain simple ground motion models for Mw 8.7 earthquakes. The resulting models were adjusted to account for the discrepancies between the recorded and simulated ground motions of the 2001 Arequipa earthquake, as seen in Figures 5 and 6. Specifically, we compensated for the trough in the simulations at 0.5 second period and the peaks in the simulations at 1 and 2 second period. The resulting ground motion models are given in Tables 6 and 7, and compared with the three ground motion models and the average of the simulations in Figures 65 and 66. We consider that these ground motion models are appropriate for estimating the response spectra of ground motions of earthquakes that rupture the entire Cascadia Plate Interface.

Table 6. Ground motion model for Mw 8.7 earthquakes rupturing the entire Cascadia Plate Interface, NEHRP B/C site conditions

Ln (Sa) = C1 + C2 * closest distance

Period	C1	C2
0.01	-0.10886E+01	-0.81363E
0.10	-0.39134E+00	-0.83152E
0.20	-0.22889E+00	-0.80824E
0.50	-0.31710E+00	-0.81941E
1.00	-0.10361E+01	-0.72873E
2.00	-0.18363E+01	-0.81329E
5.00	-0.34516E+01	-0.74857E
10.0	-0.40081E+01	-0.46149E
20.0	-0.50548E+01	-0.34997E

Table 7. Ground motion model for Mw 8.7 earthquakes rupturing the entire Cascadia Plate Interface, NEHRP D site conditions

Ln (Sa) = C1 + C2 * closest distance

Period	C1	C2
0.01	-0.84186E+00	-0.72997E
0.10	-0.14461E+00	-0.74786E
0.20	0.17834E-01	-0.72458E
0.50	-0.00056E+00	-0.73553E
1.00	-0.15740E+00	-0.64667E
2.00	-0.11876E+01	-0.73122E
5.00	-0.30029E+01	-0.66650E
10.0	-0.35594E+01	-0.37942E
20.0	-0.46061E+01	-0.26790E

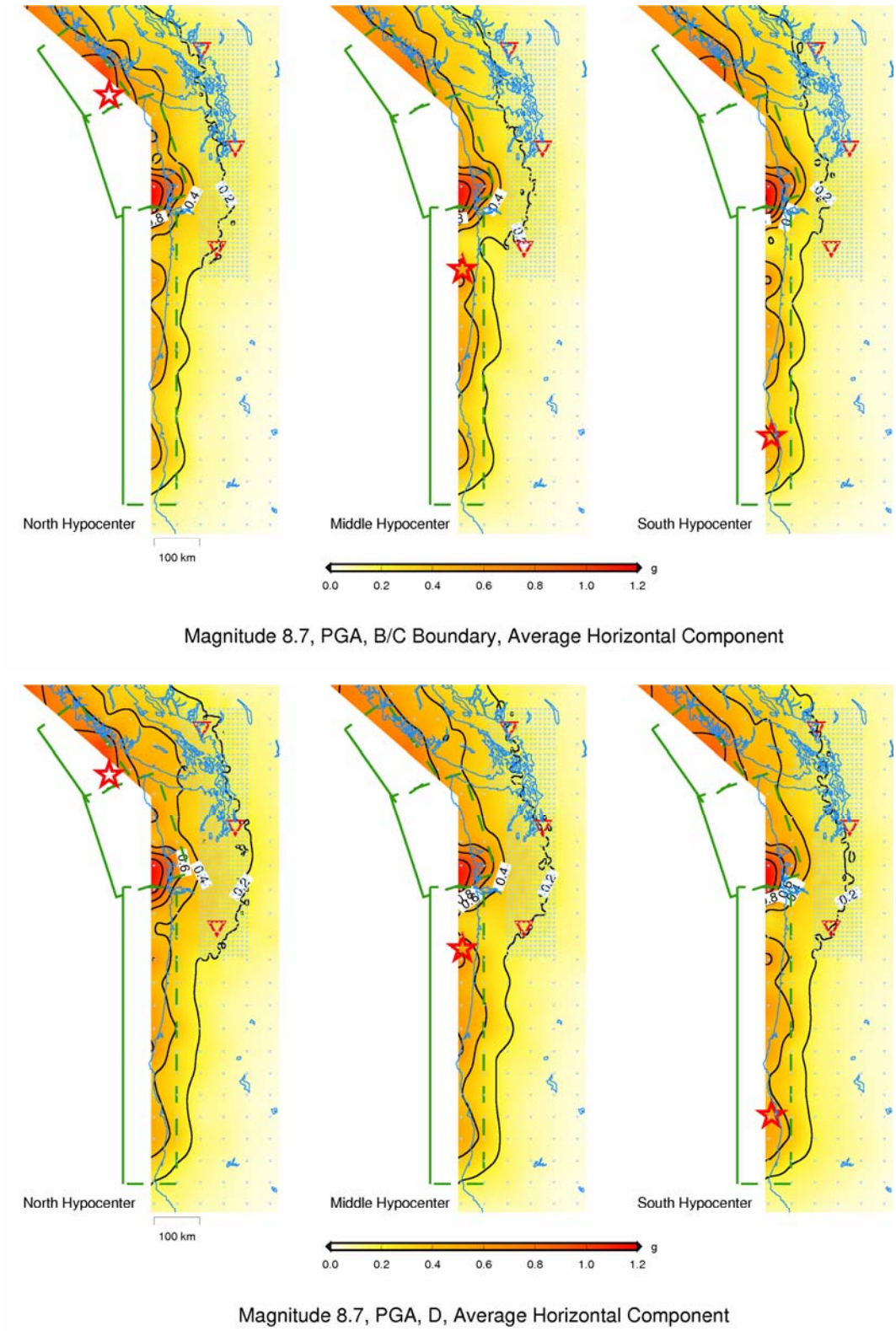

Figure 23. Ground motion maps for peak acceleration for an Mw 8.7 Cascadia earthquake for three hypocenter locations for soft rock (top) and deep soil (bottom) site conditions

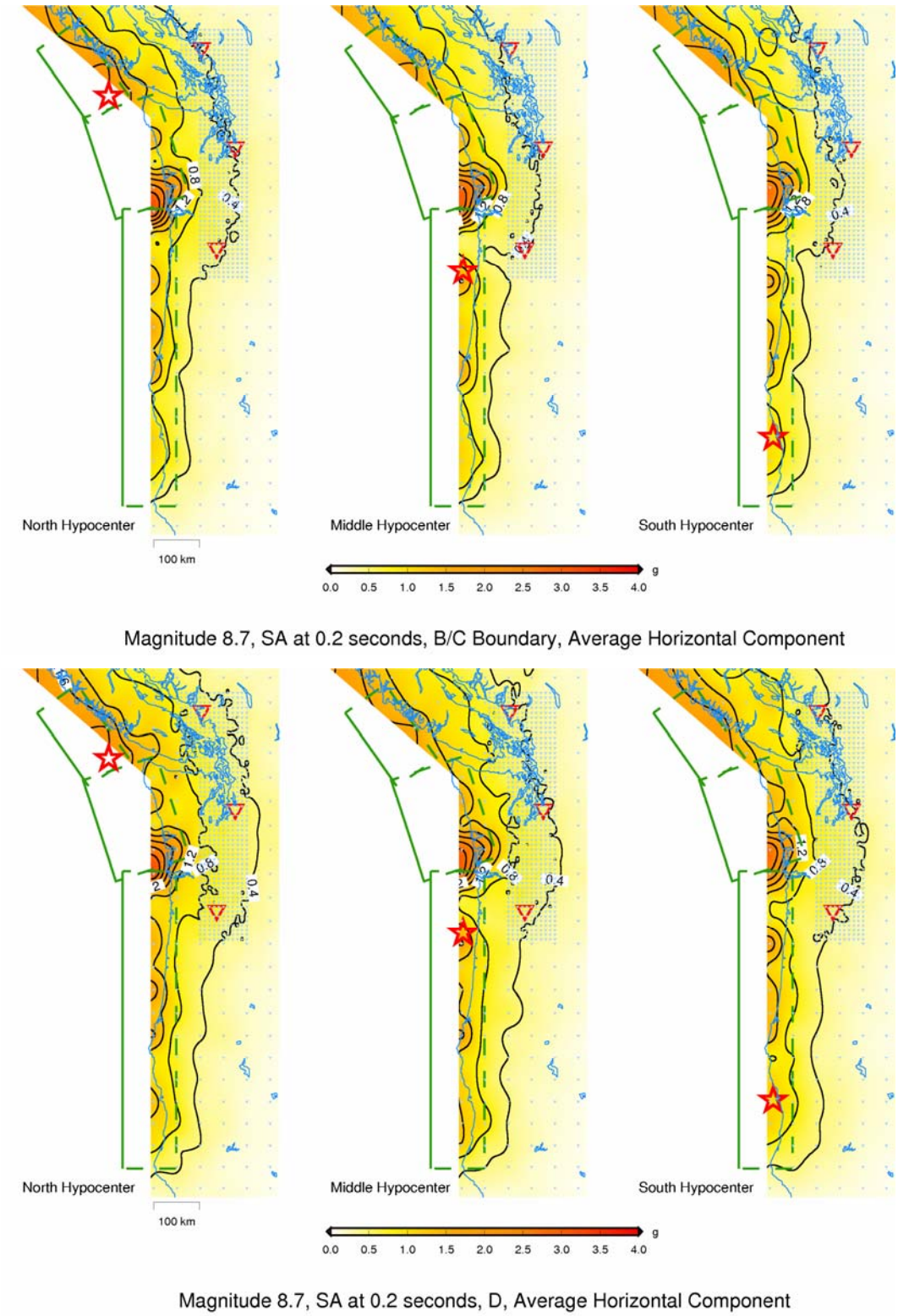

Figure 24. Ground motion maps for 0.2 sec spectral acceleration for an Mw 8.7 Cascadia earthquake for three hypocenter locations for soft rock (top) and deep soil (bottom) site conditions

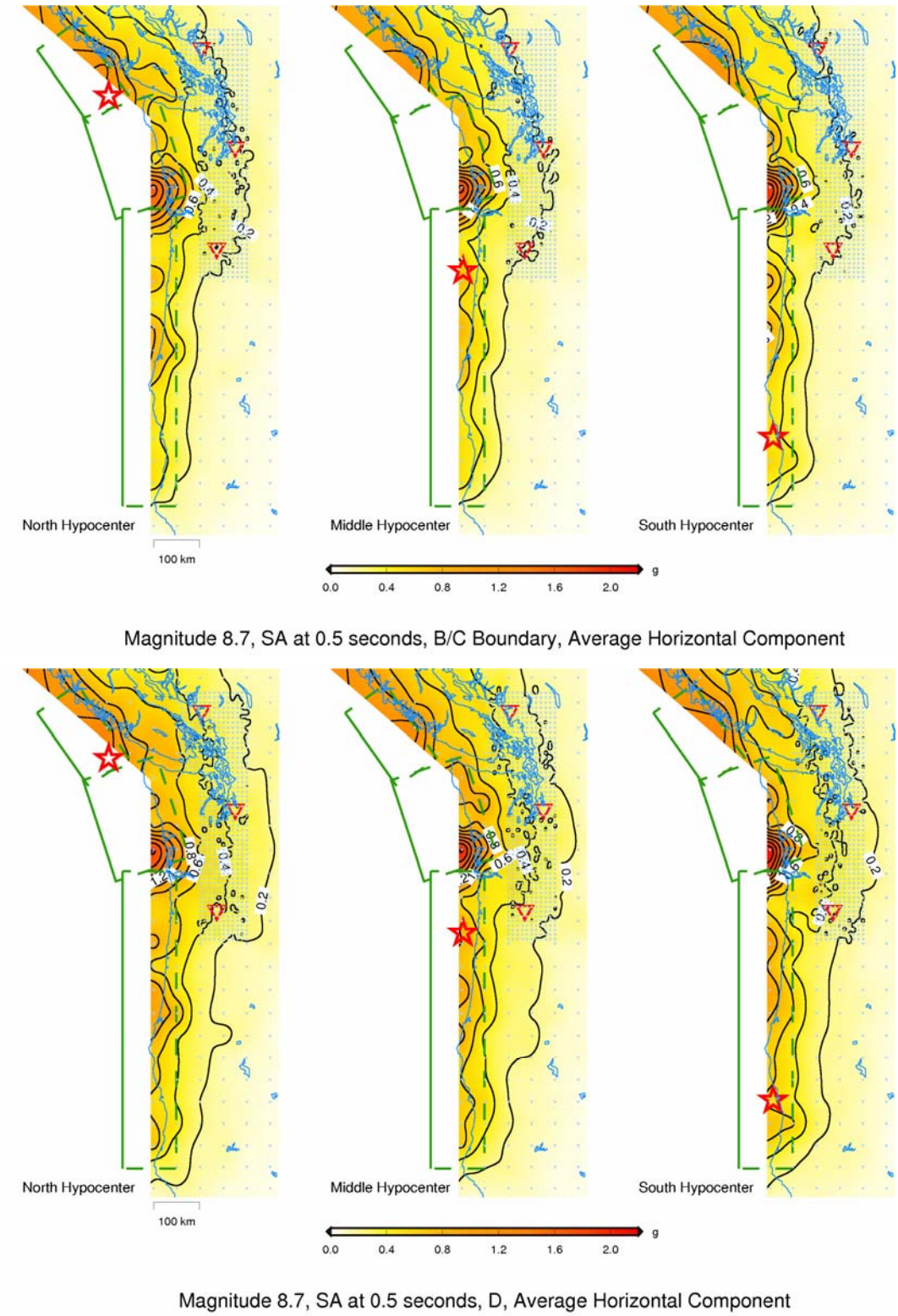

Figure 25. Ground motion maps for 0.5 sec spectral acceleration for an Mw 8.7 Cascadia earthquake for three hypocenter locations for soft rock (top) and deep soil (bottom) site conditions

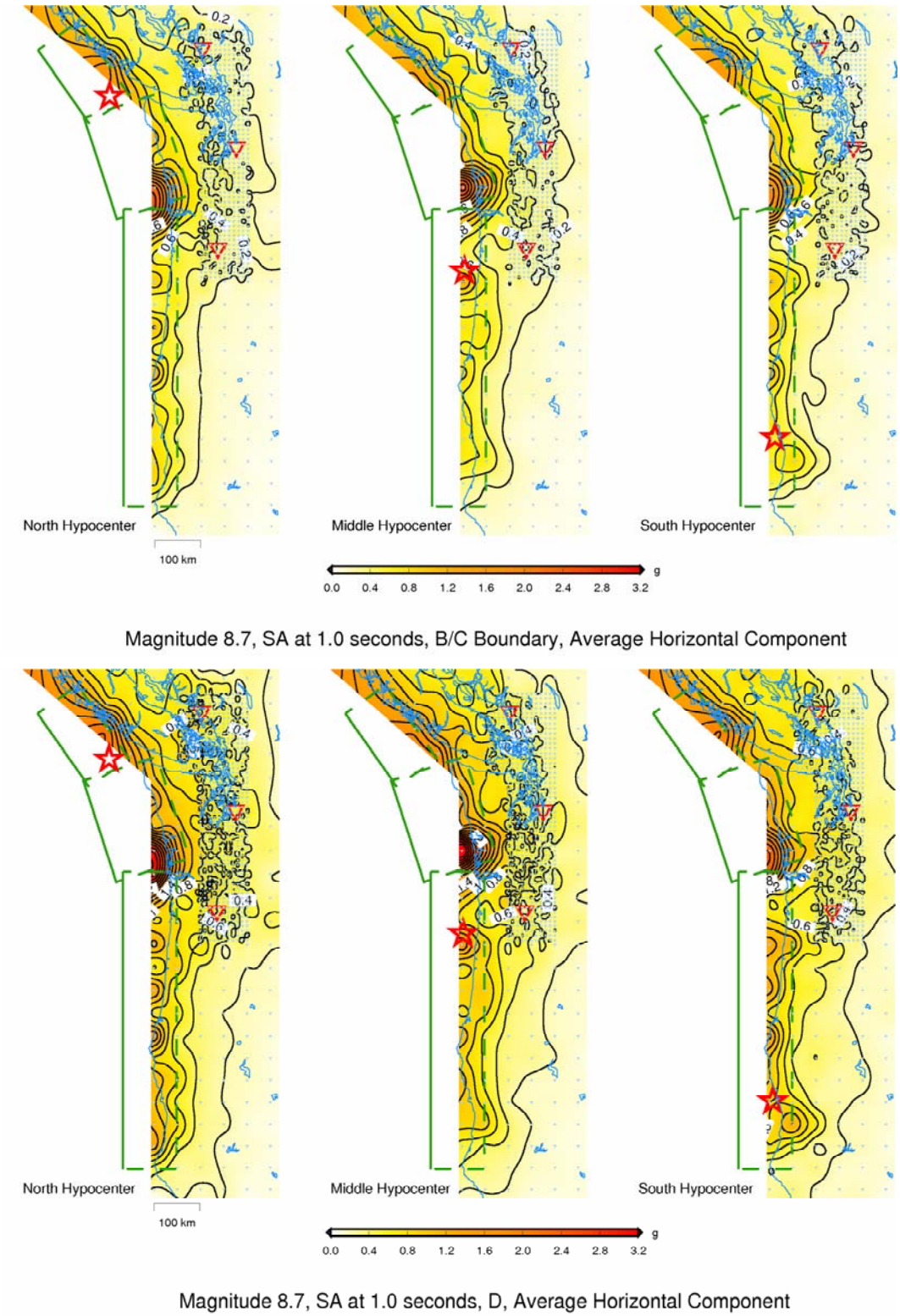

Figure 26. Ground motion maps for 1 sec spectral acceleration for an Mw 8.7 Cascadia earthquake for three hypocenter locations for soft rock (top) and deep soil (bottom) site conditions

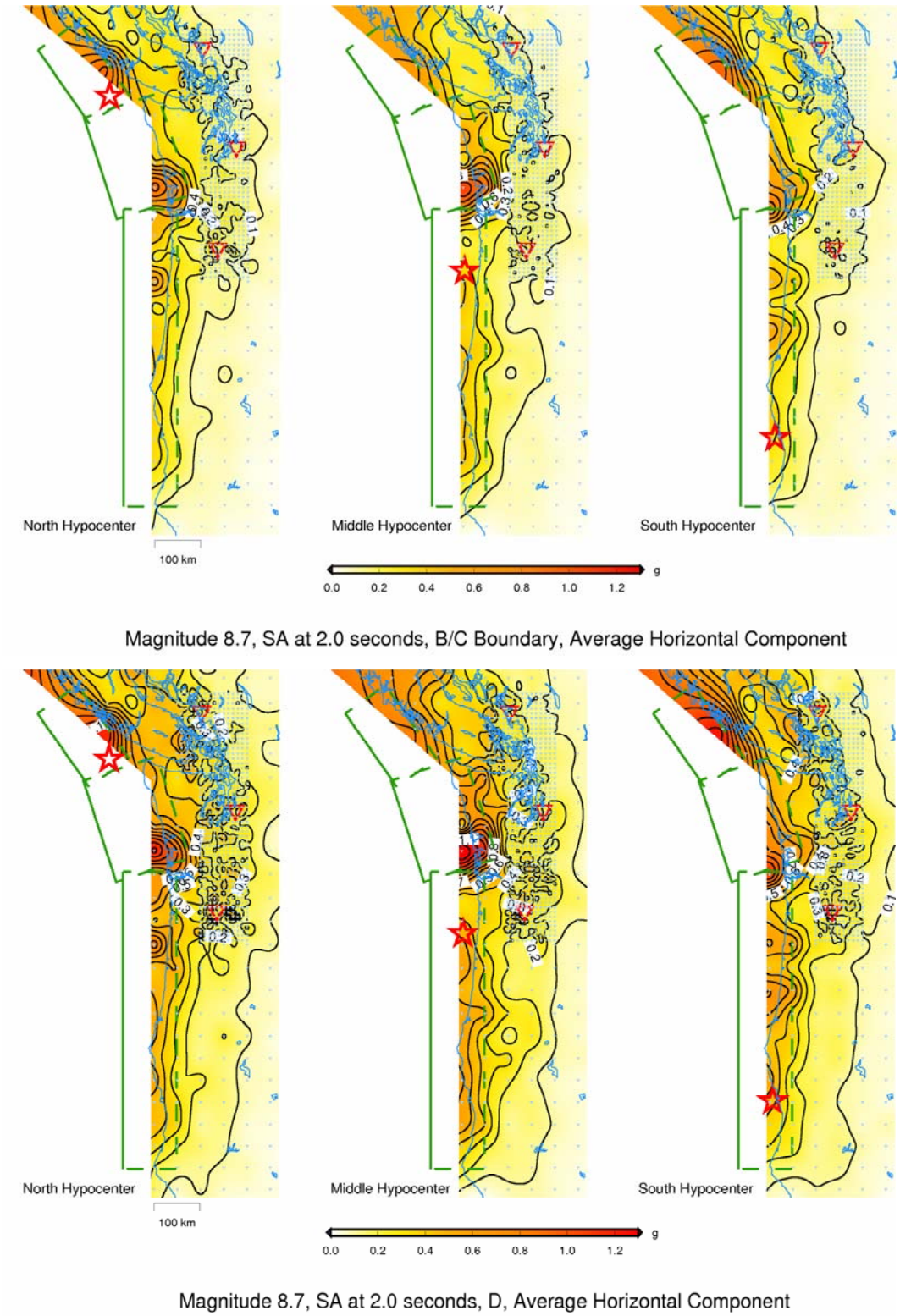

Figure 27. Ground motion maps for 2 sec spectral acceleration for an Mw 8.7 Cascadia earthquake for three hypocenter locations for soft rock (top) and deep soil (bottom) site conditions

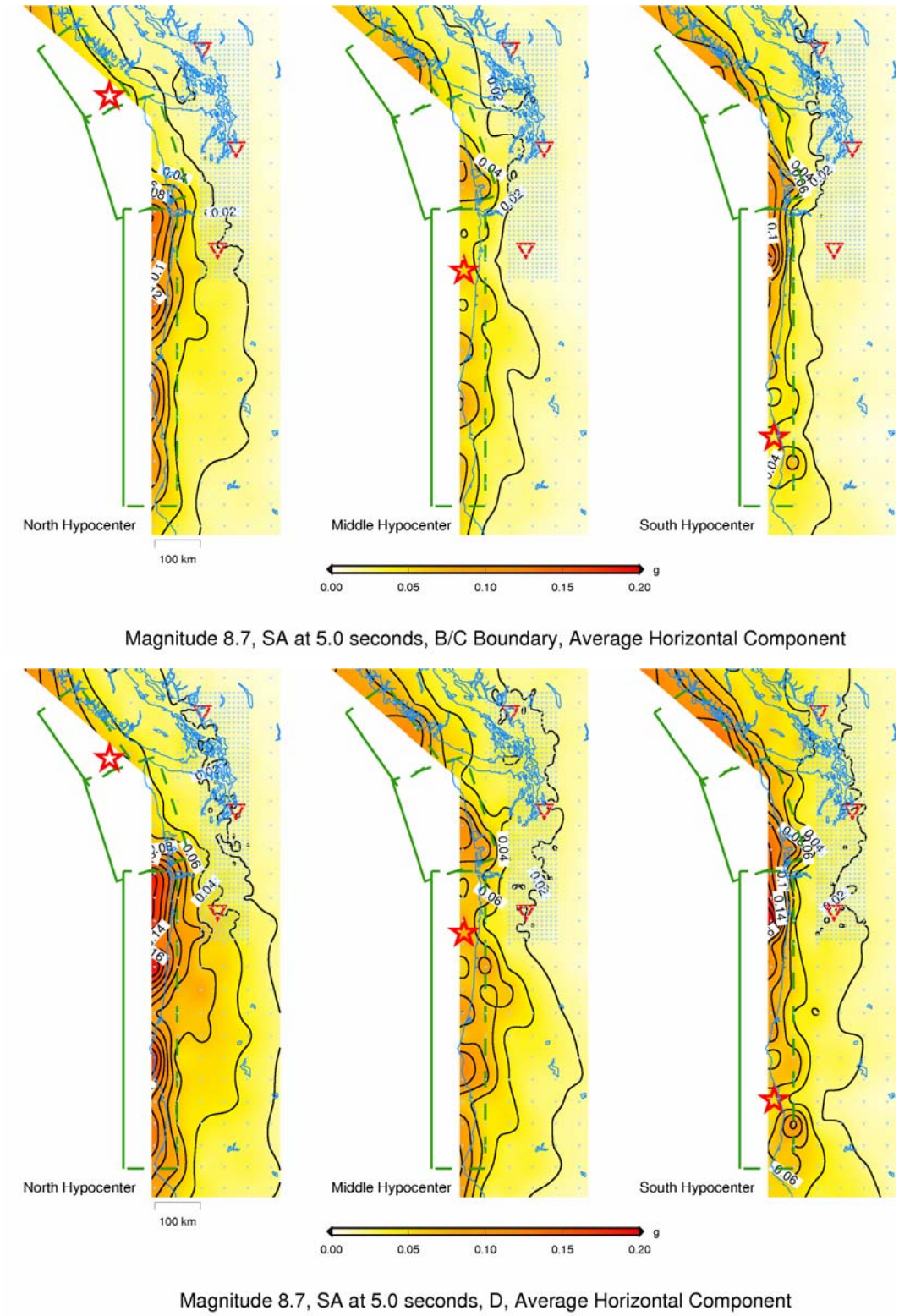

Figure 28. Ground motion maps for 5 sec spectral acceleration for an Mw 8.7 Cascadia earthquake for three hypocenter locations for soft rock (top) and deep soil (bottom) site conditions

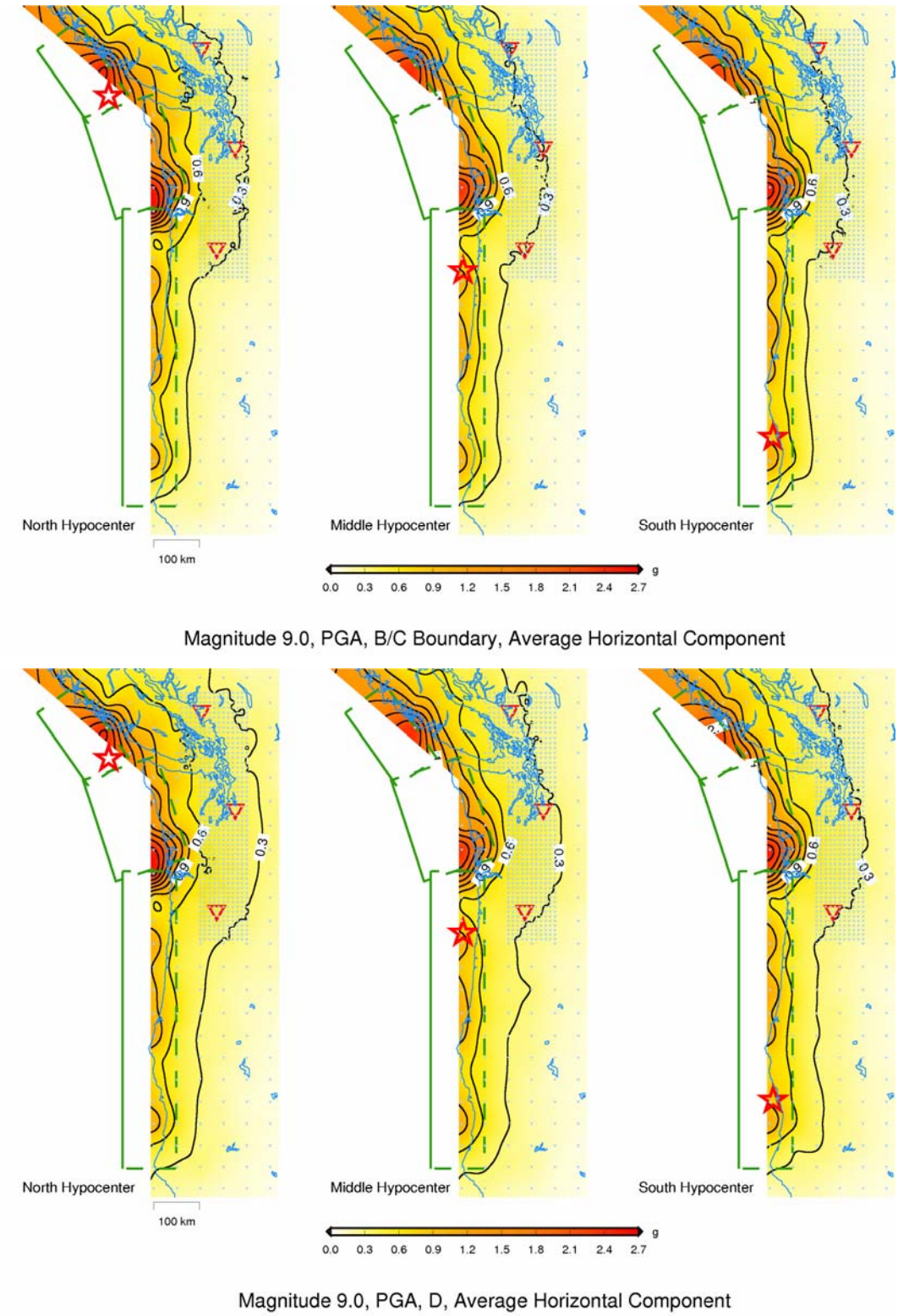

Figure 29. Ground motion maps for peak acceleration for an Mw 9.0 Cascadia earthquake for three hypocenter locations for soft rock (top) and deep soil (bottom) site conditions. The earthquake has average slip twice as large as that predicted by the Somerville et al. (2002) scaling relations.

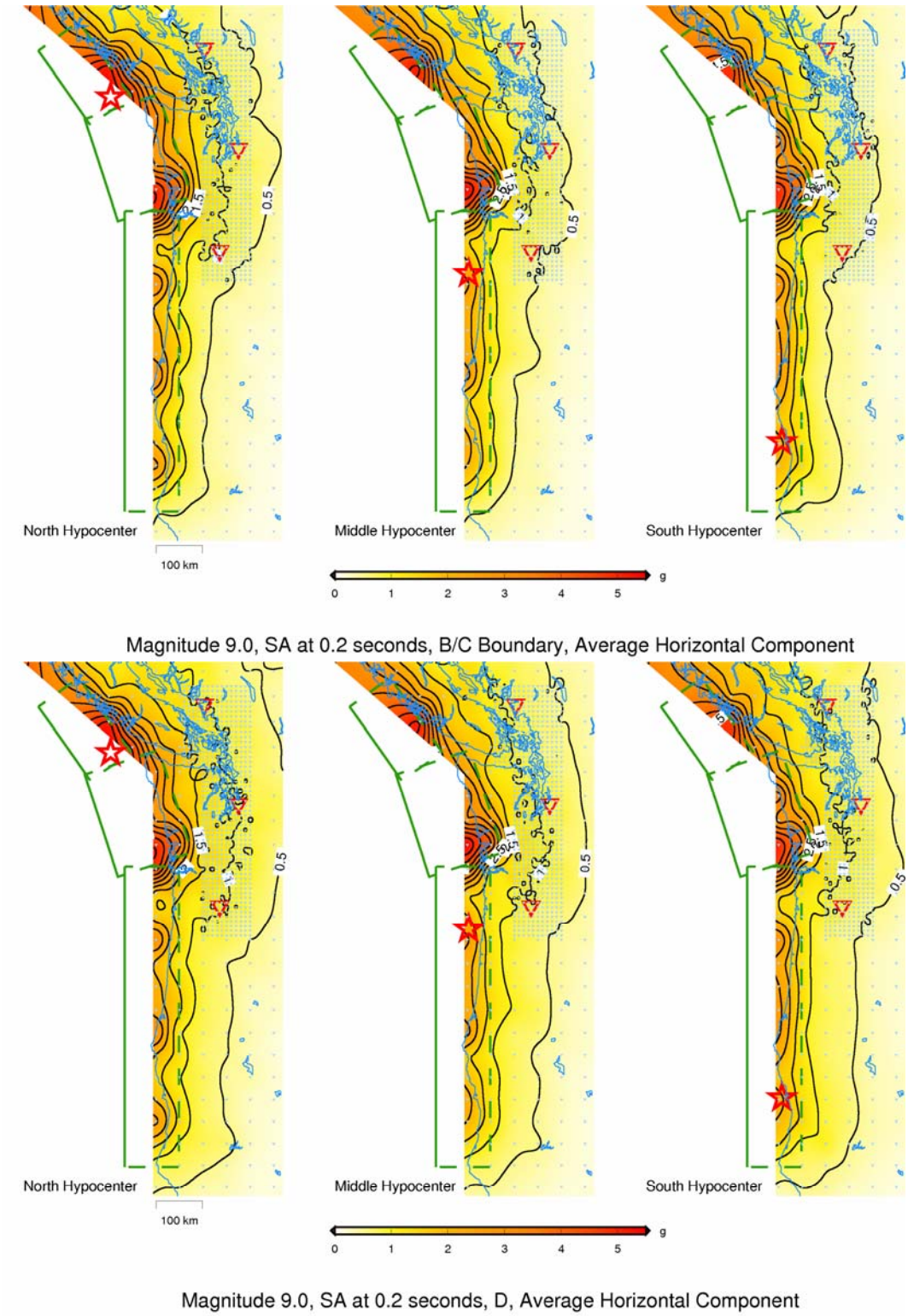

Figure 30. Ground motion maps for 0.2 sec spectral acceleration for an Mw 9.0 Cascadia earthquake for three hypocenter locations for soft rock (top) and deep soil (bottom) site conditions. The earthquake has average slip twice as large as that predicted by the Somerville et al. (2002) scaling relations.

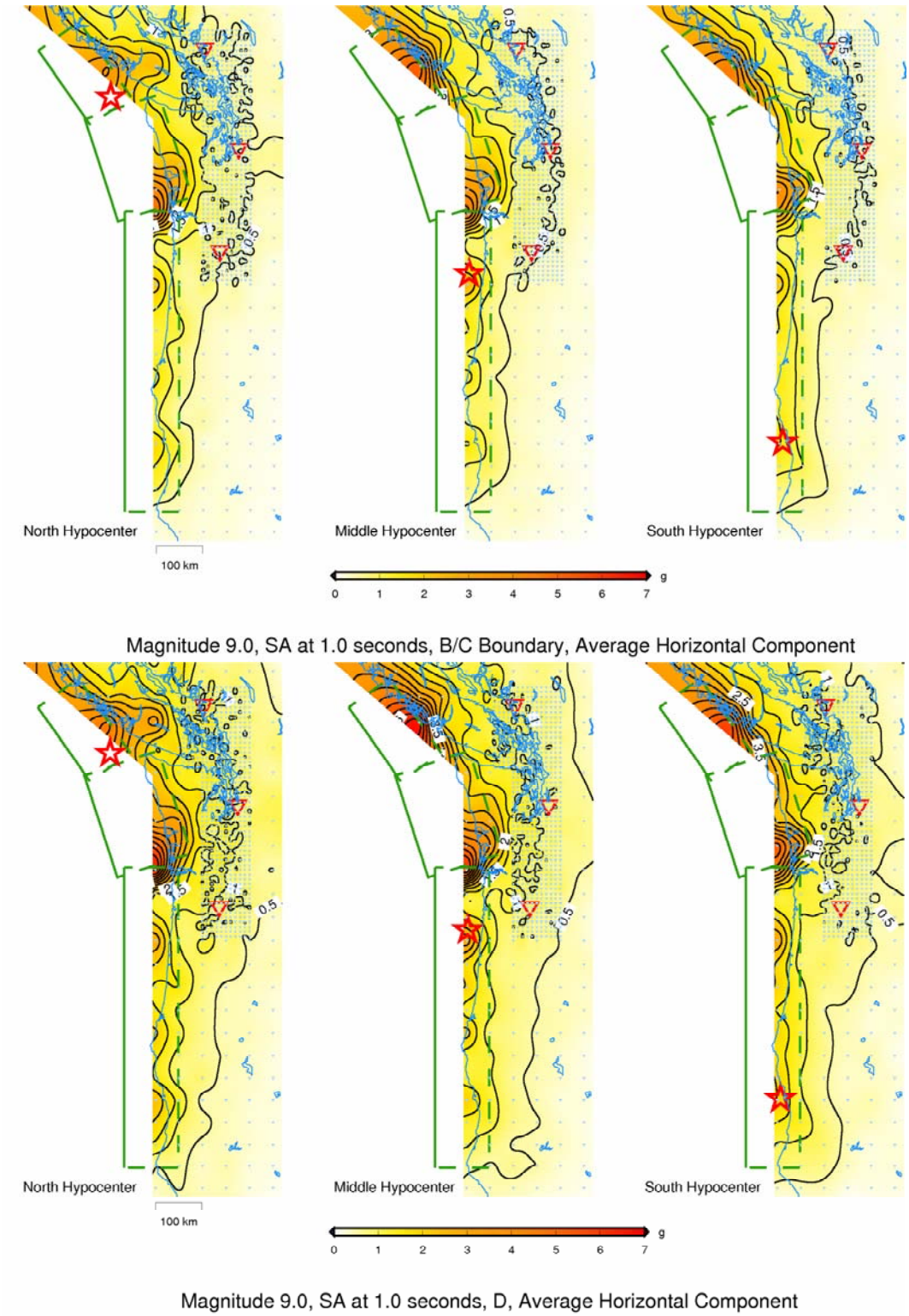

Figure 31. Ground motion maps for 1 sec spectral acceleration for an Mw 9.0 Cascadia earthquake for three hypocenter locations for soft rock (top) and deep soil (bottom) site conditions. The earthquake has average slip twice as large as that predicted by the Somerville et al. (2002) scaling relations.

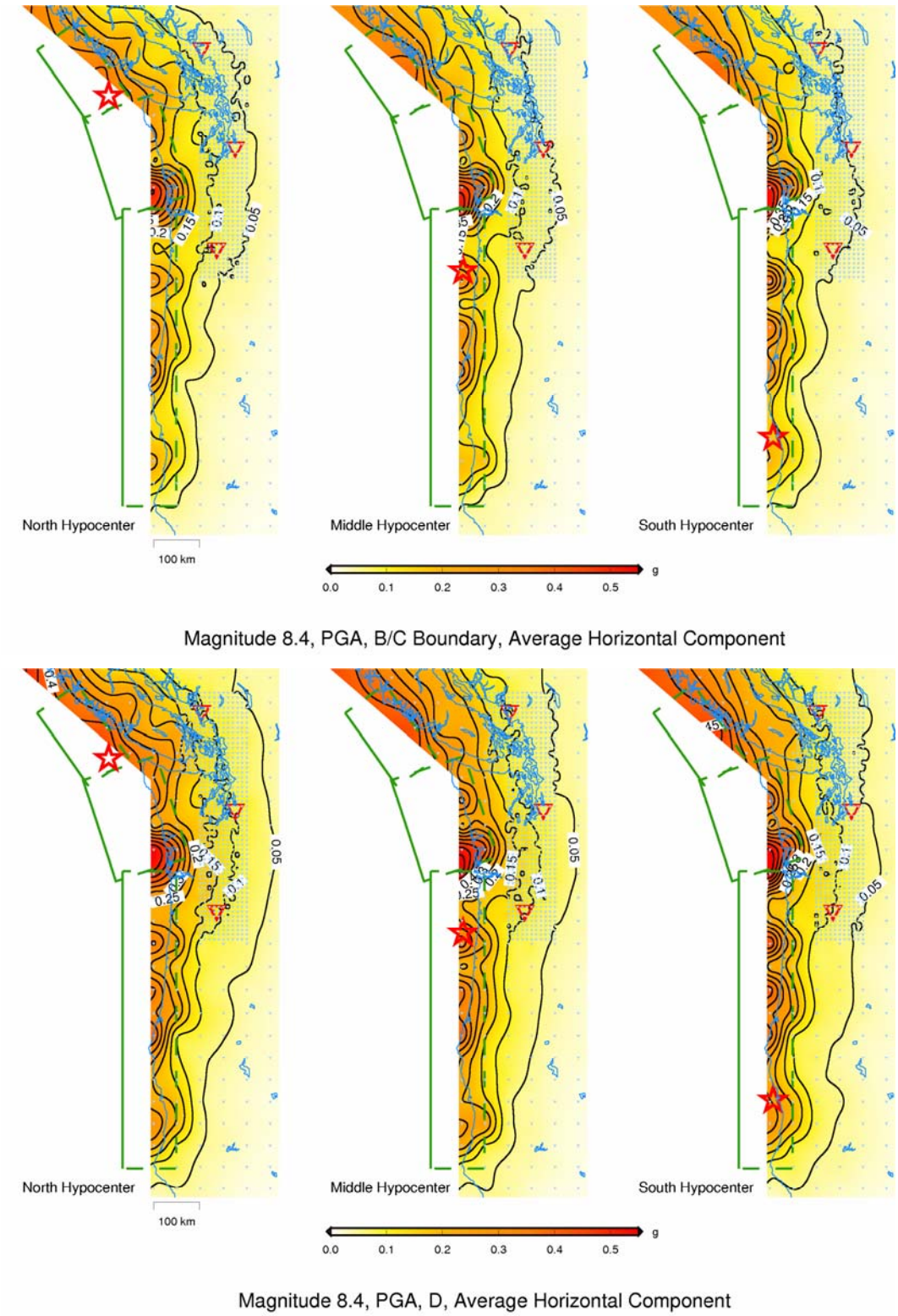

Figure 32. Ground motion maps for peak acceleration for an Mw 8.4 Cascadia earthquake for three hypocenter locations for soft rock (top) and deep soil (bottom) site conditions. The earthquake has average slip half as large as that predicted by the Somerville et al. (2002) scaling relations.

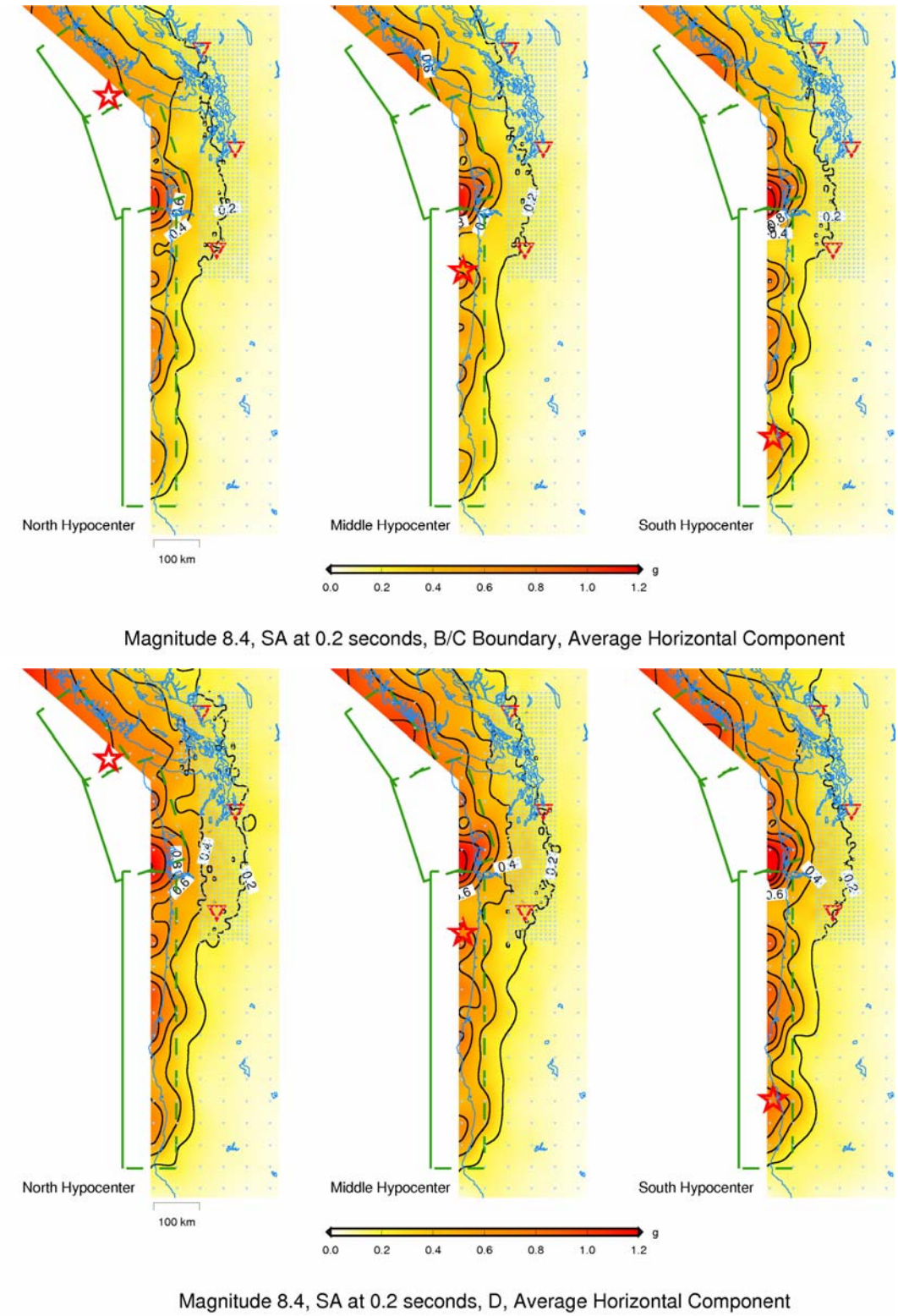

Figure 33. Ground motion maps for 0.2 sec spectral acceleration for an Mw 8.4 Cascadia earthquake for three hypocenter locations for soft rock (top) and deep soil (bottom) site conditions. The earthquake has average slip half as large as that predicted by the Somerville et al. (2002) scaling relations.

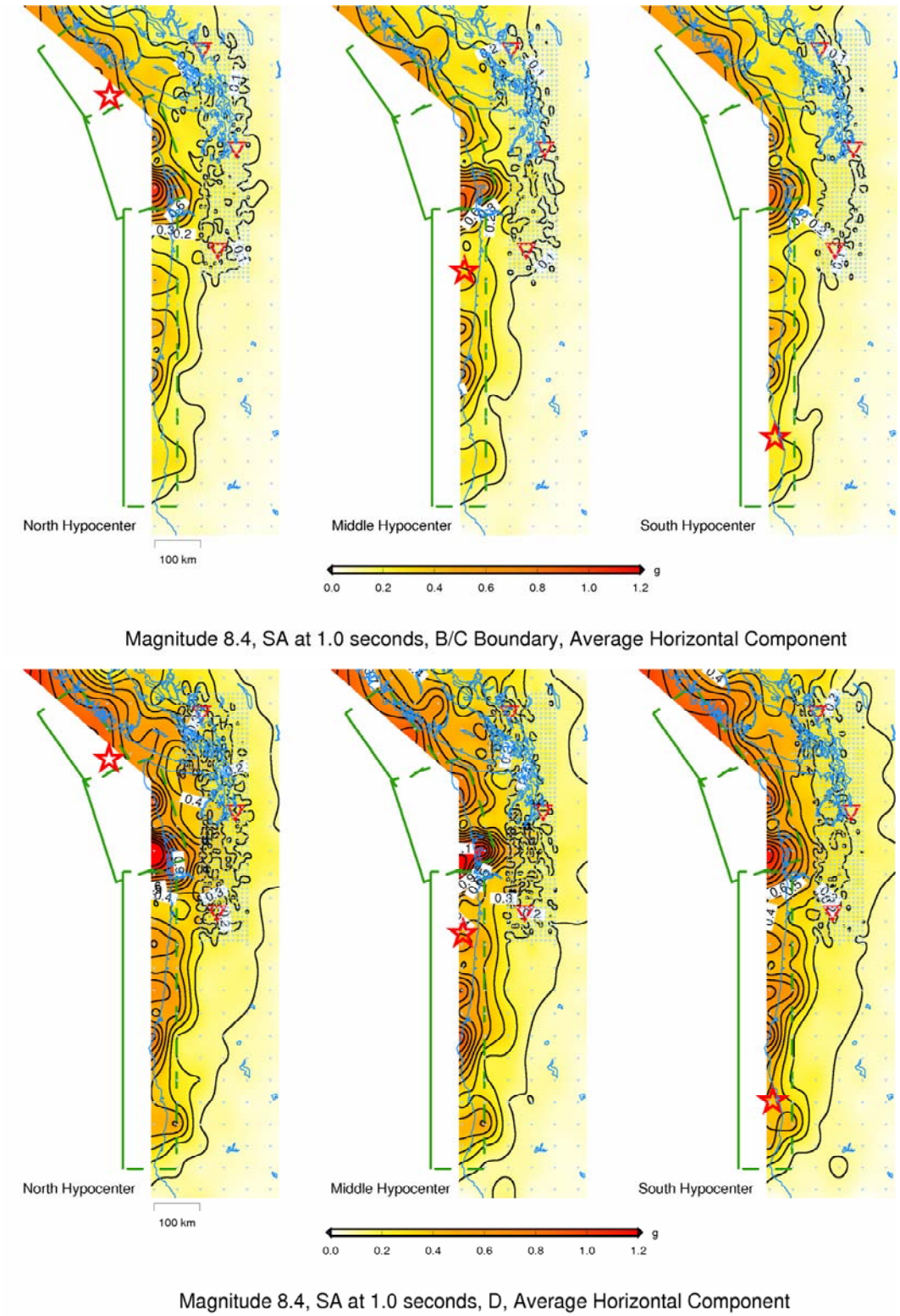

Figure 34. Ground motion maps for 1 sec spectral acceleration for an Mw 8.4 Cascadia earthquake for three hypocenter locations for soft rock (top) and deep soil (bottom) site conditions. The earthquake has average slip half as large as that predicted by the Somerville et al. (2002) scaling relations.

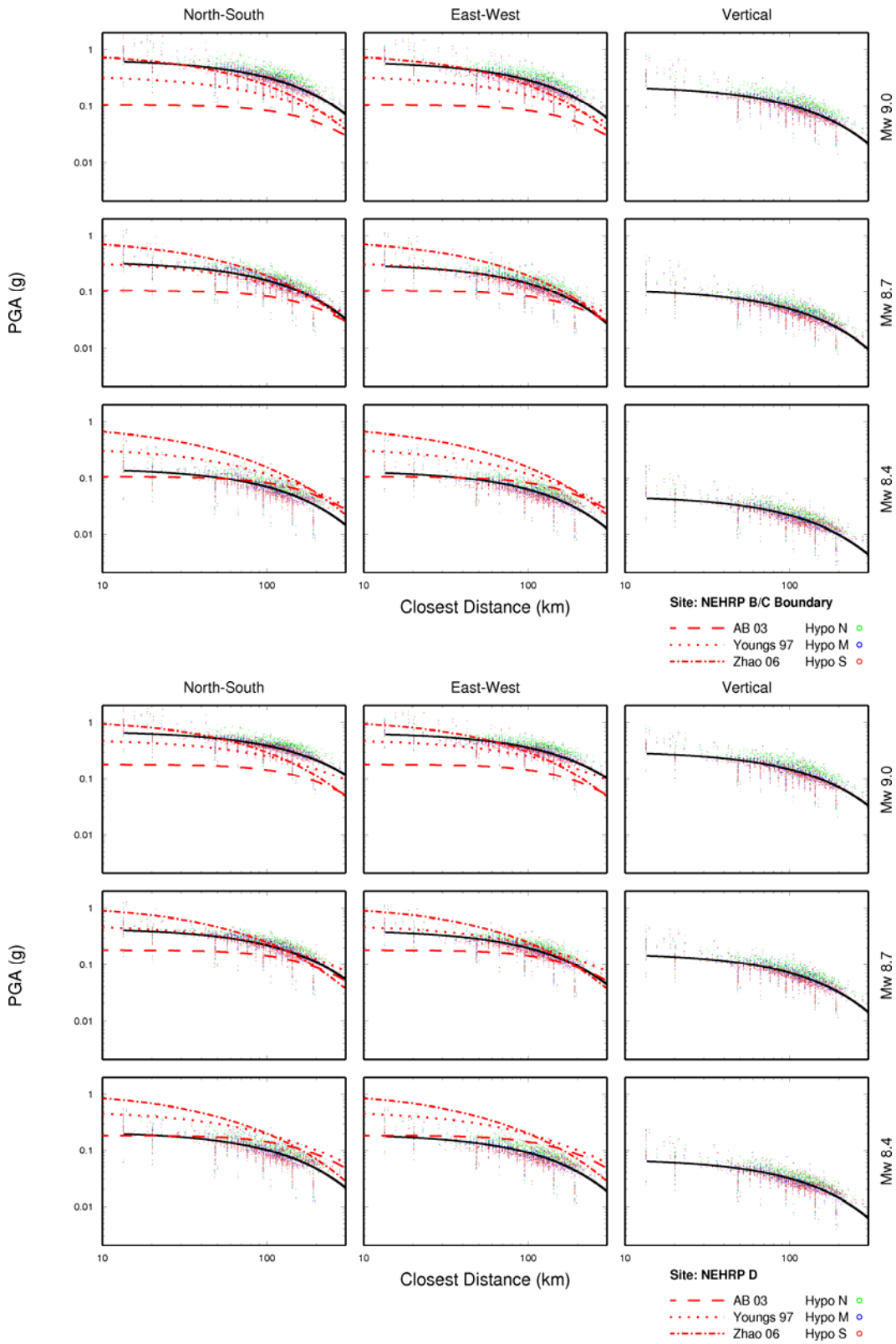

Figure 35. Comparison of simulated peak accelerations (points and black line) for Mw 9.0, 8.7 and 8.4 Cascadia earthquakes with ground motion models for soft rock (top) and deep soil (bottom). Only Mw 8.7 simulations have Somerville et al. (2002) scaling.

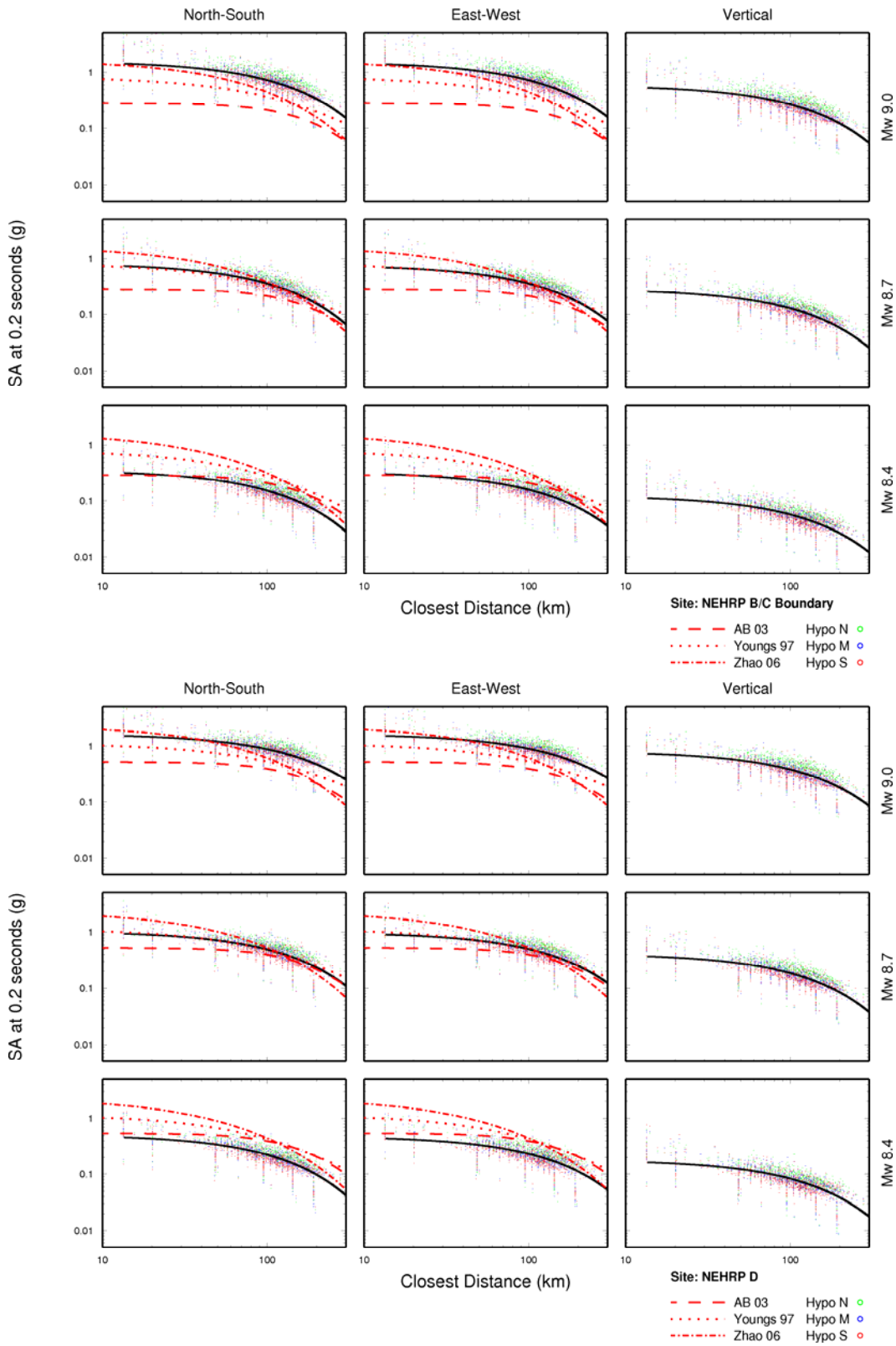

Figure 36. Comparison of simulated 0.2 sec spectral accelerations (points and black line) for Mw 9.0, 8.7 and 8.4 Cascadia earthquakes with ground motion models for soft rock (top) and deep soil (bottom). Only Mw 8.7 simulations have Somerville et al. (2002) scaling.

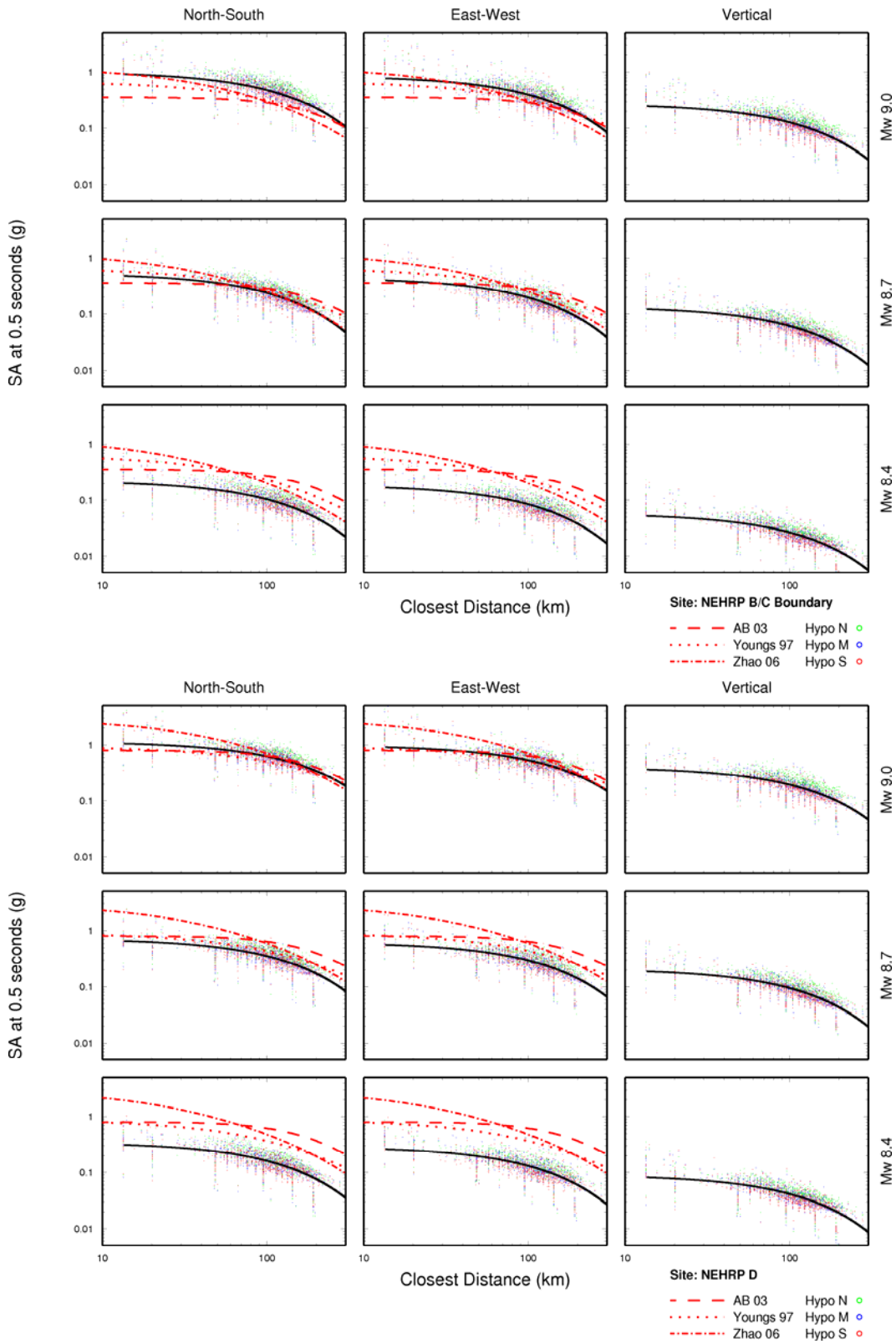

Figure 37. Comparison of simulated 0.5 sec spectral accelerations (points and black line) for Mw 9.0, 8.7 and 8.4 Cascadia earthquakes with ground motion models for soft rock (top) and deep soil (bottom). Only Mw 8.7 simulations have Somerville et al. (2002) scaling.

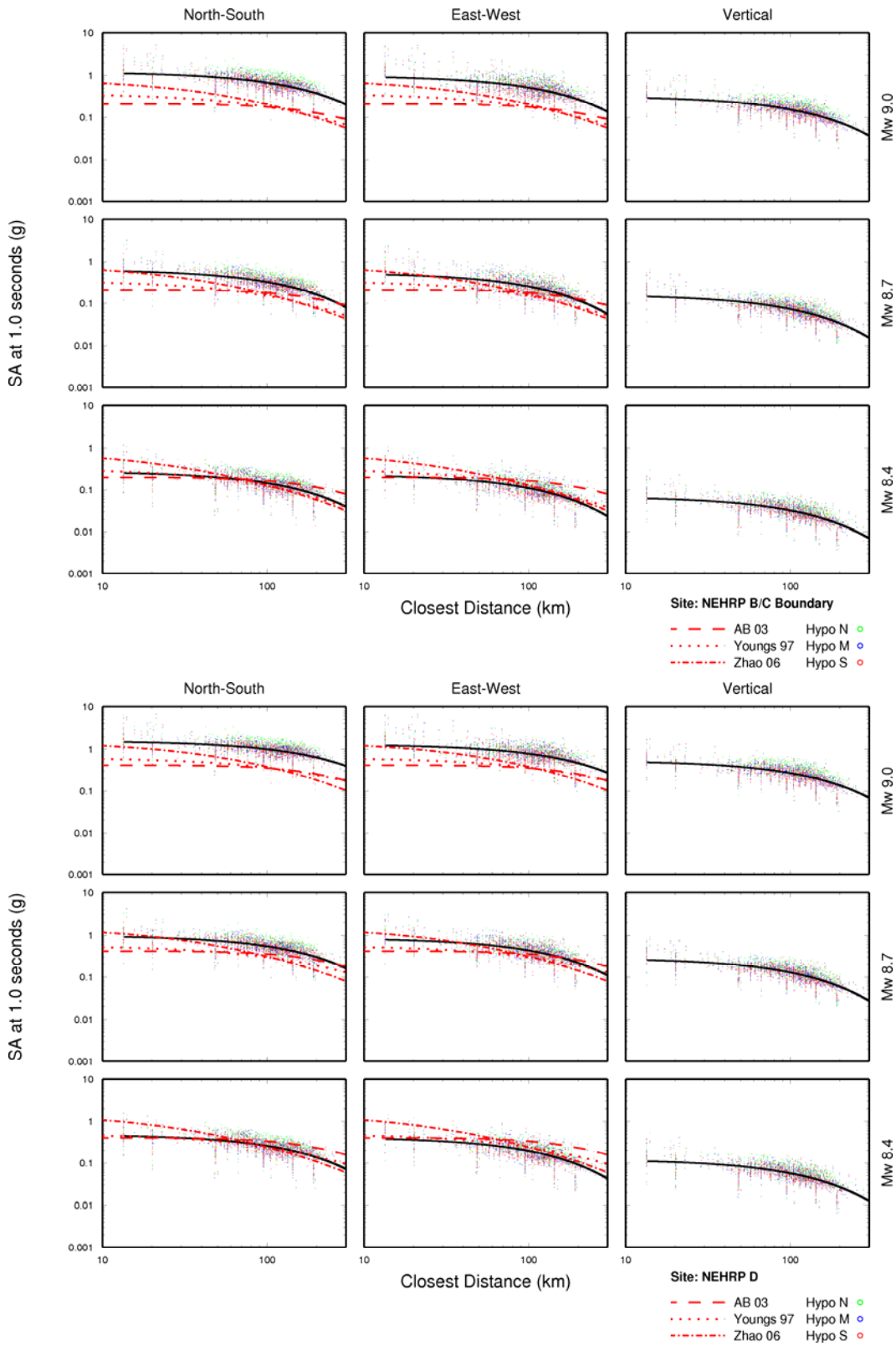

Figure 38. Comparison of simulated 1 sec spectral accelerations (points and black line) for Mw 9.0, 8.7 and 8.4 Cascadia earthquakes with ground motion models for soft rock (top) and deep soil (bottom). Only Mw 8.7 simulations have Somerville et al. (2002) scaling.

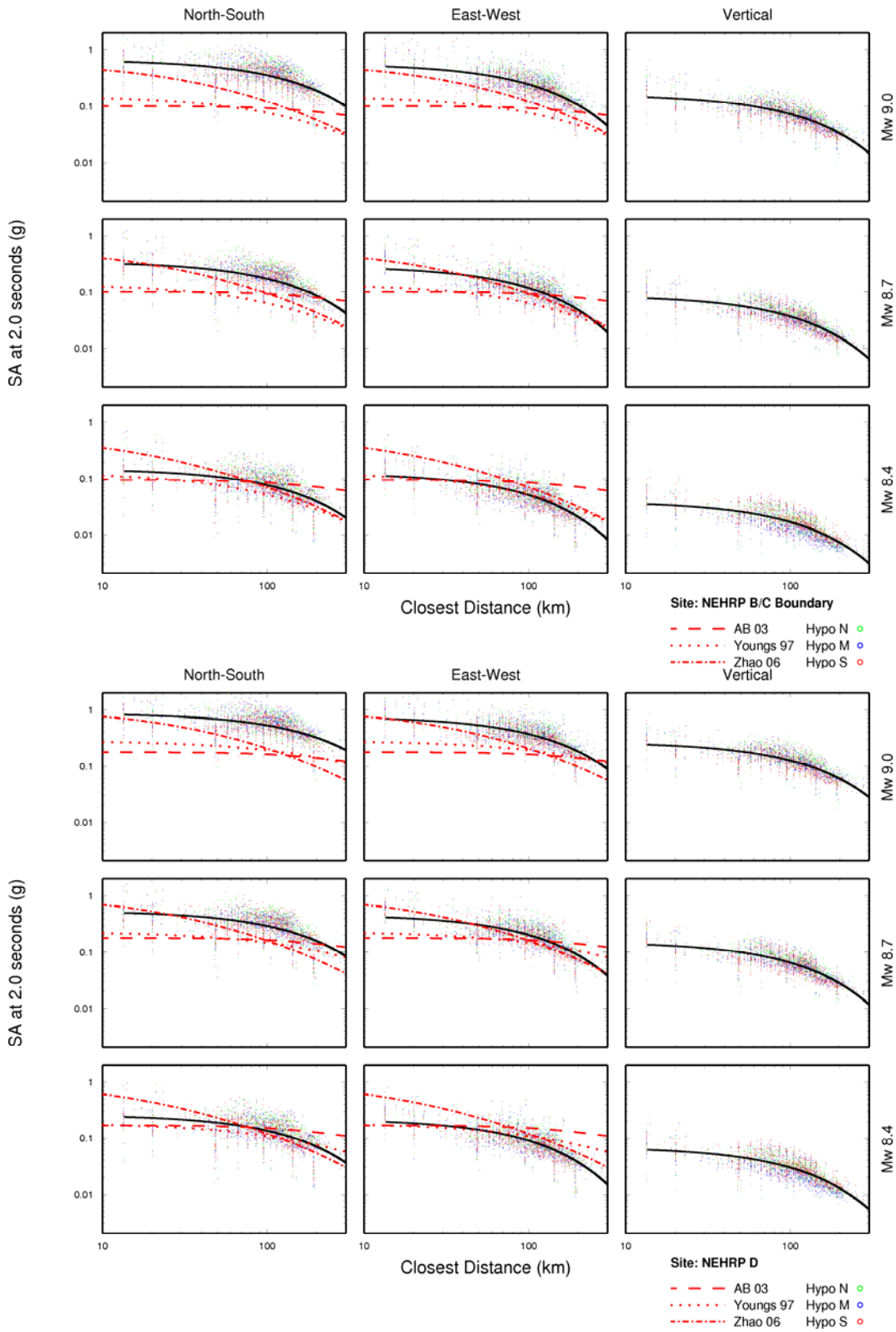

Figure 39. Comparison of simulated 2 sec spectral accelerations (points and black line) for Mw 9.0, 8.7 and 8.4 Cascadia earthquakes with ground motion models for soft rock (top) and deep soil (bottom). Only Mw 8.7 simulations have Somerville et al. (2002) scaling.

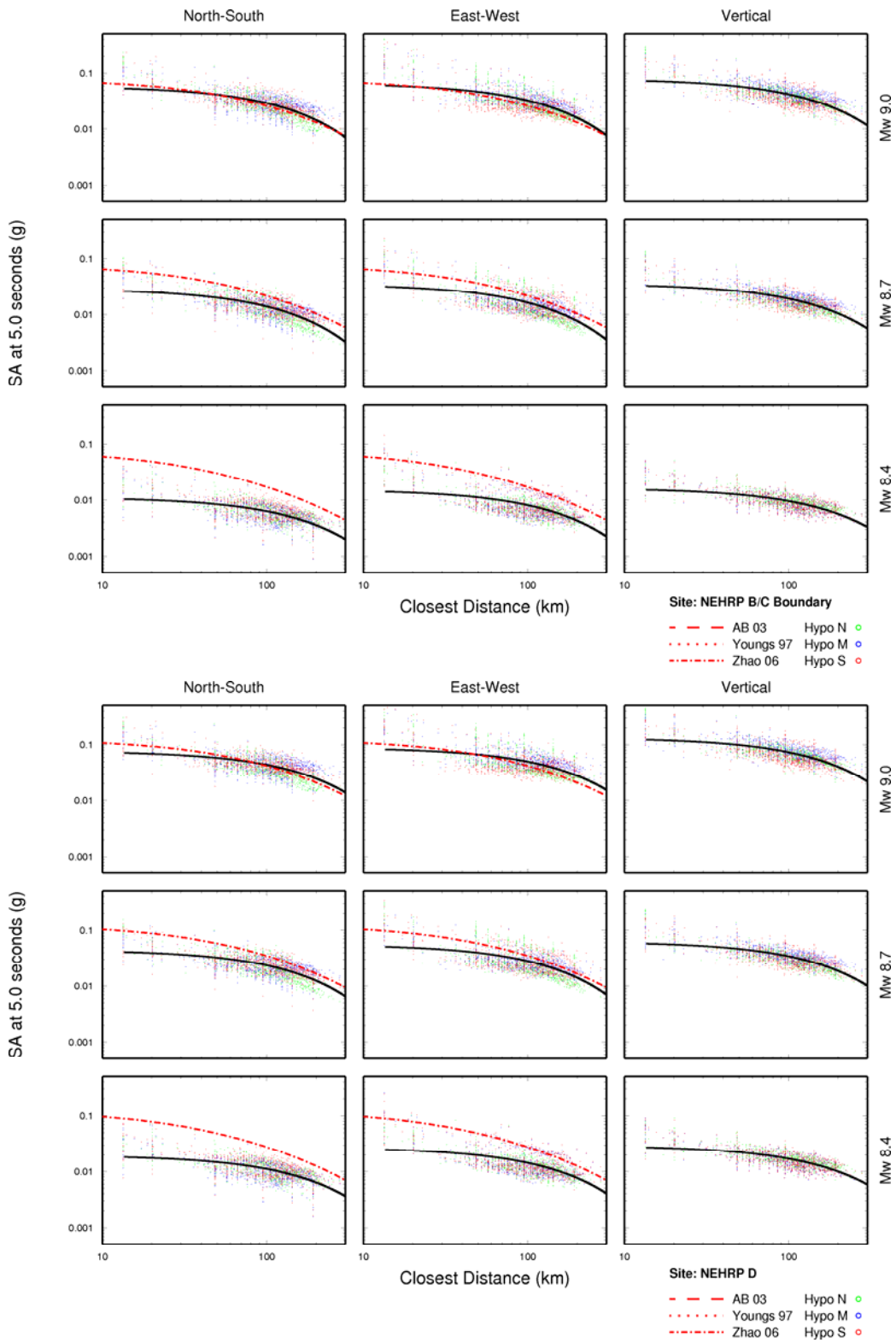

Figure 40. Comparison of simulated 5 sec spectral accelerations (points and black line) for Mw 9.0, 8.7 and 8.4 Cascadia earthquakes with ground motion models for soft rock (top) and deep soil (bottom). Only Mw 8.7 simulations have Somerville et al. (2002) scaling.

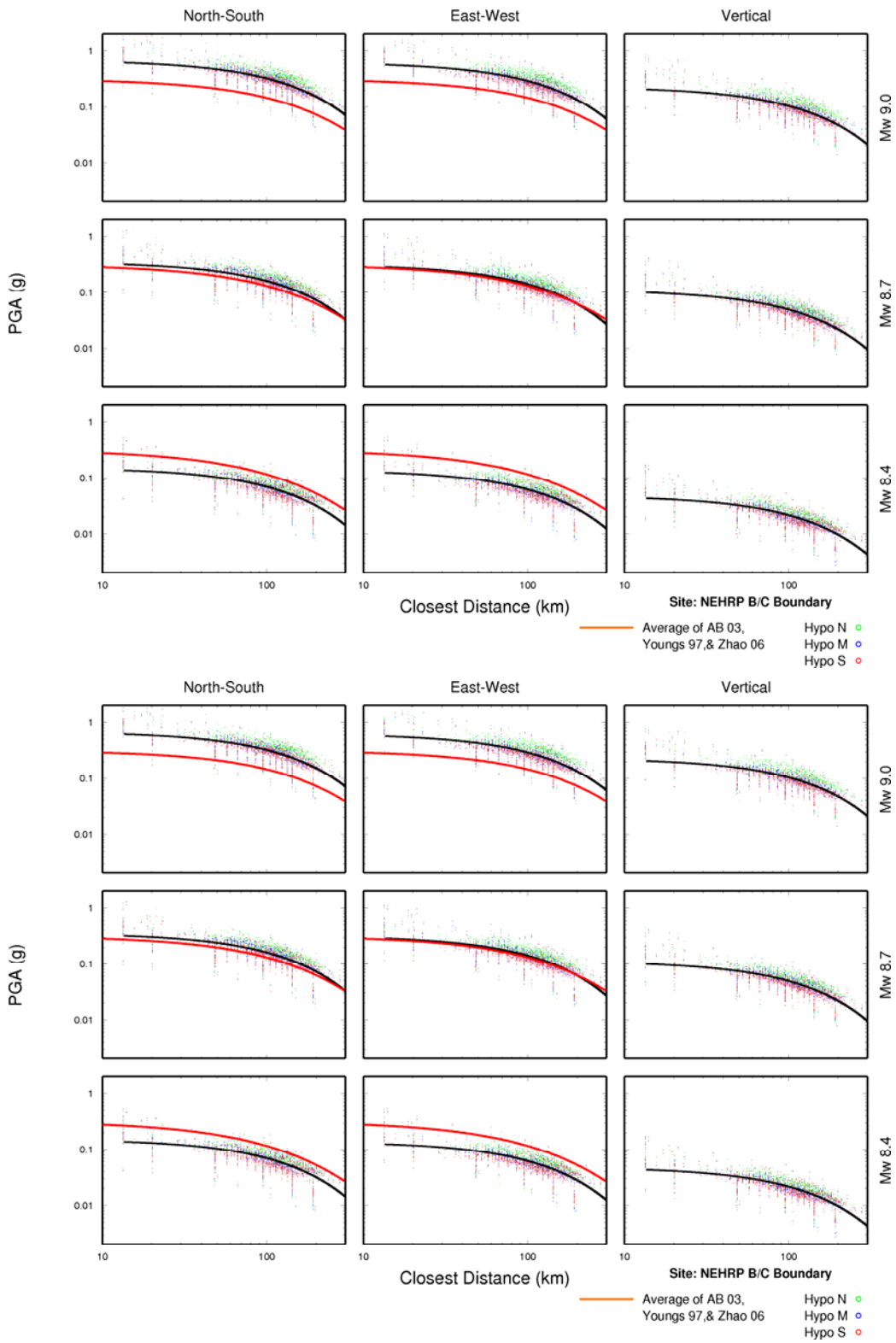

Figure 41. Comparison of simulated peak accelerations (points and black line) for Mw 9.0, 8.7 and 8.4 Cascadia earthquakes with the average of three ground motion models for soft rock (top) and deep soil (bottom). Only Mw 8.7 simulations have Somerville et al. (2002) scaling.

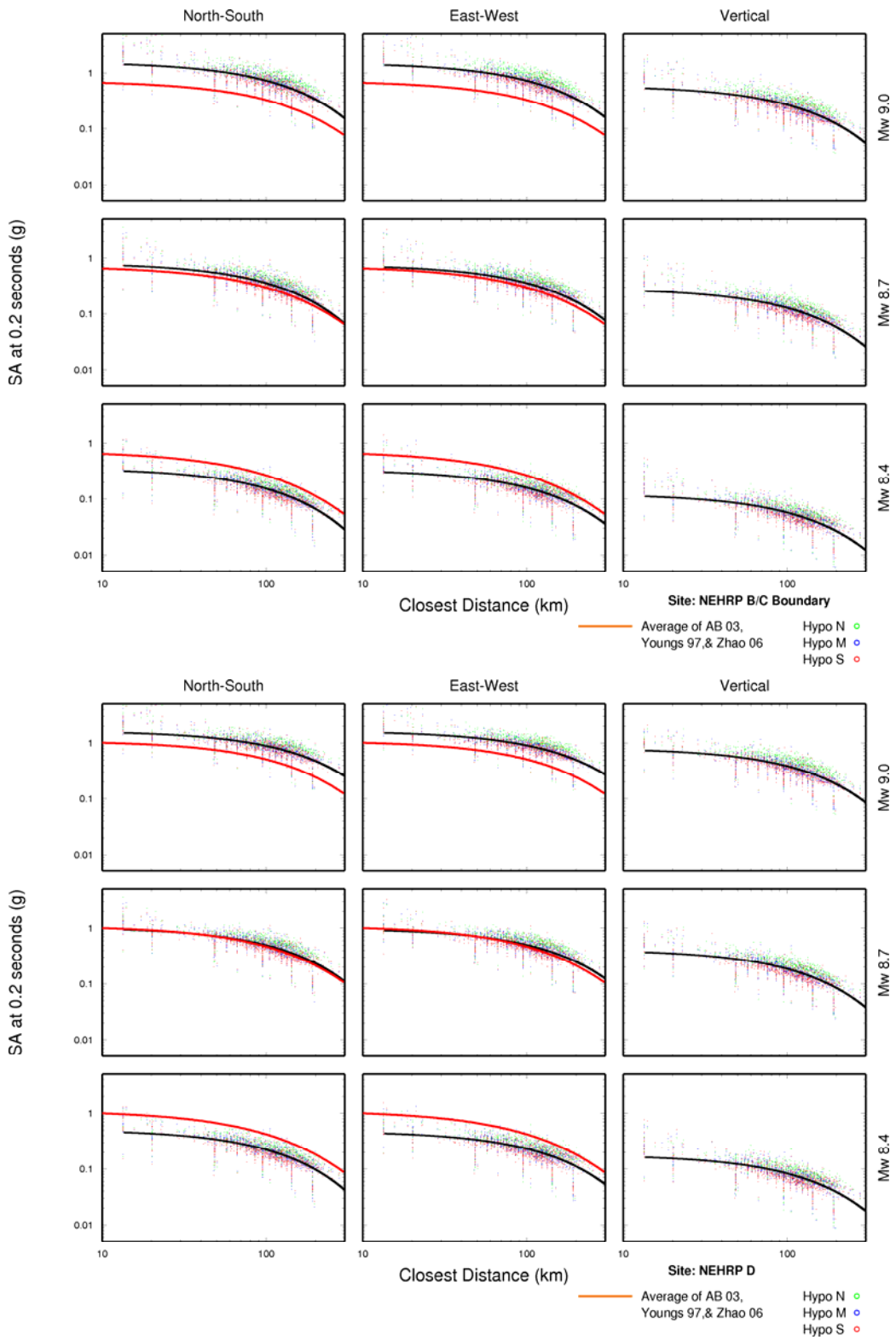

Figure 42. Comparison of simulated 0.2 sec spectral accelerations (points and black line) for Mw 9.0, 8.7 and 8.4 Cascadia earthquakes with the average of three ground motion models for soft rock (top) and deep soil (bottom). Only Mw 8.7 simulations have Somerville et al. (2002) scaling.

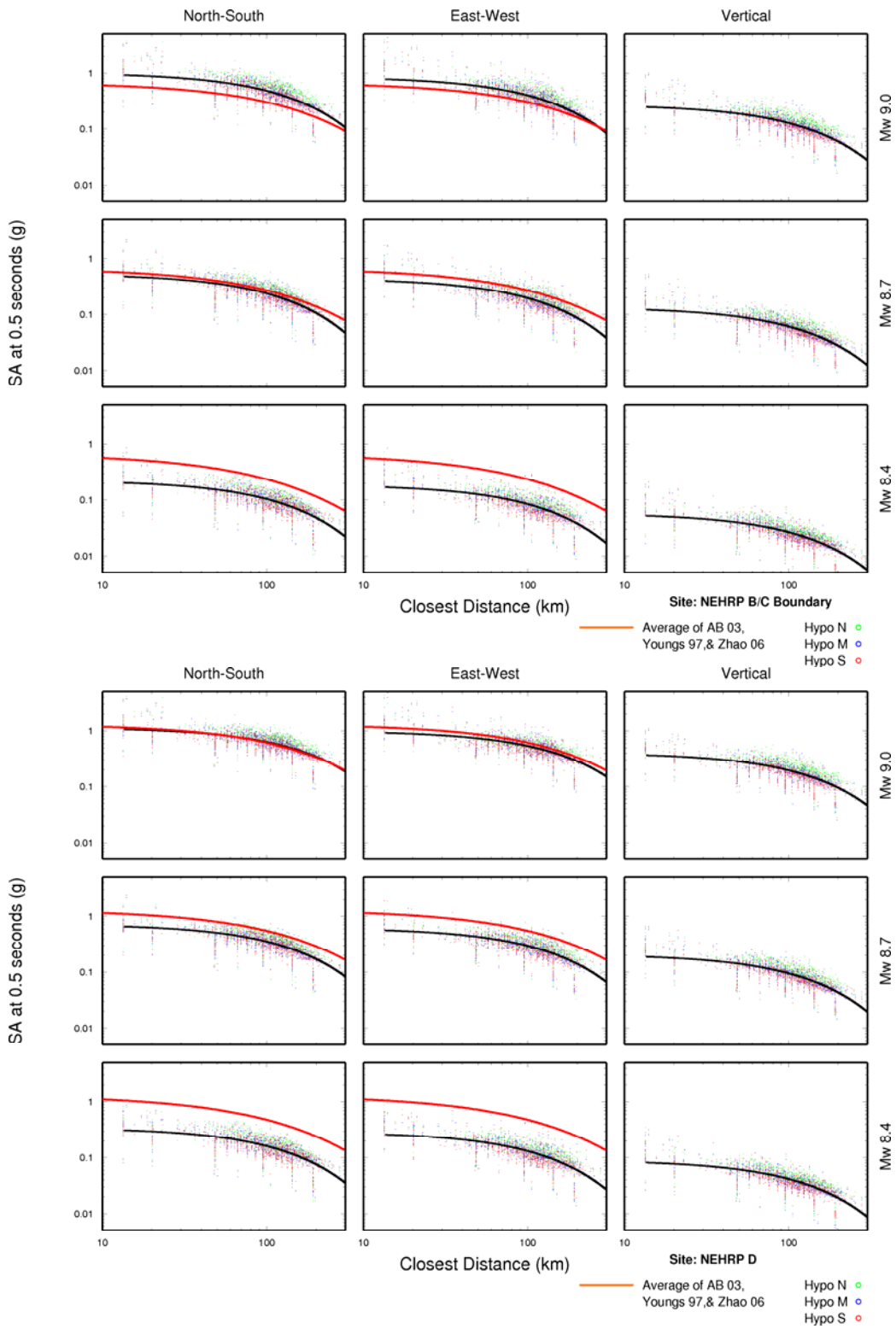

Figure 43. Comparison of simulated 0.5 sec spectral accelerations (points and black line) for Mw 9.0, 8.7 and 8.4 Cascadia earthquakes with the average of three ground motion models for soft rock (top) and deep soil (bottom). Only Mw 8.7 simulations have Somerville et al. (2002) scaling.

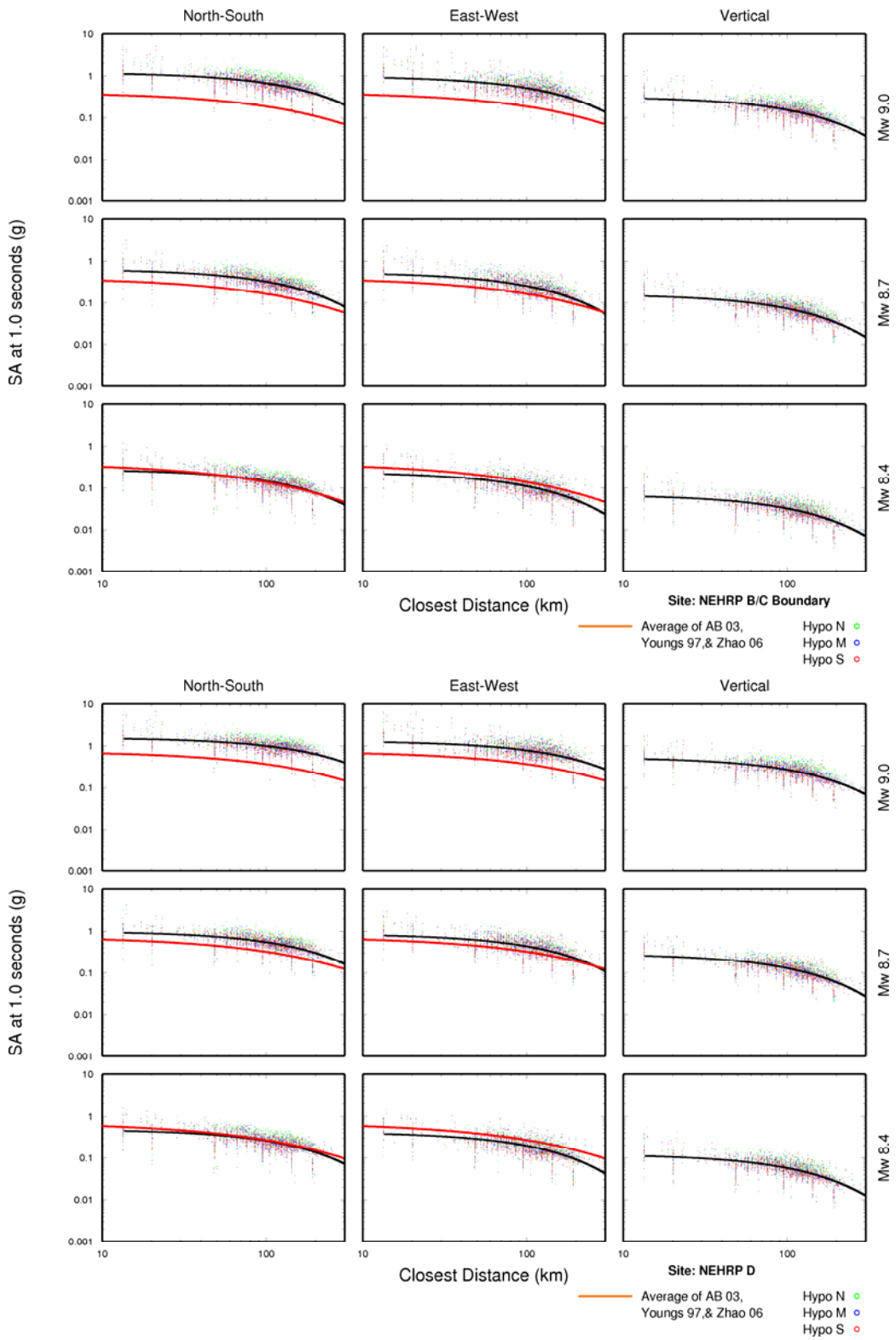

Figure 44. Comparison of simulated 1 sec spectral accelerations (points and black line) for Mw 9.0, 8.7 and 8.4 Cascadia earthquakes with the average of three ground motion models for soft rock (top) and deep soil (bottom). Only Mw 8.7 simulations have Somerville et al. (2002) scaling.

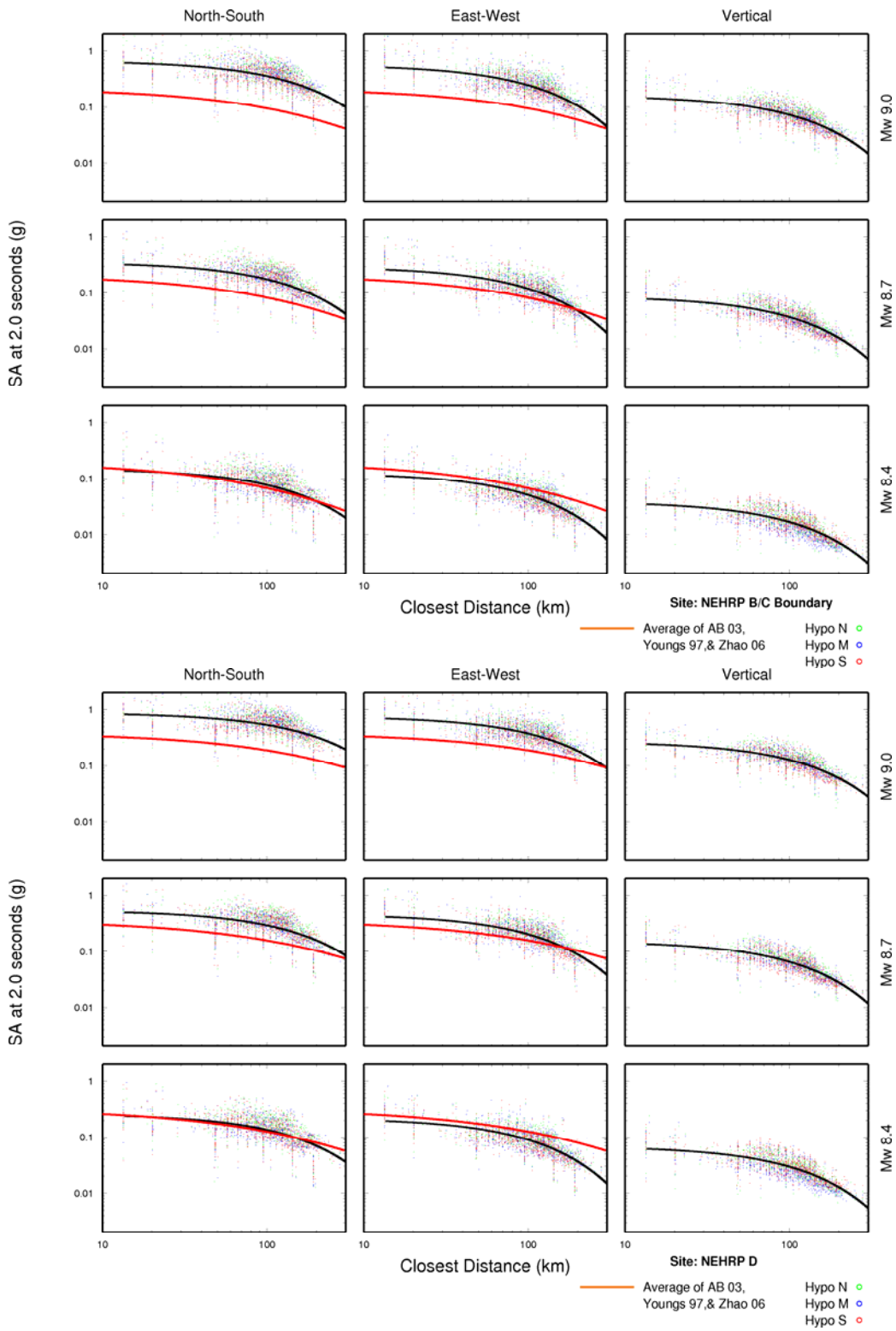

Figure 45. Comparison of simulated 2 sec spectral accelerations (points and black line) for Mw 9.0, 8.7 and 8.4 Cascadia earthquakes with the average of three ground motion models for soft rock (top) and deep soil (bottom). Only Mw 8.7 simulations have Somerville et al. (2002) scaling.

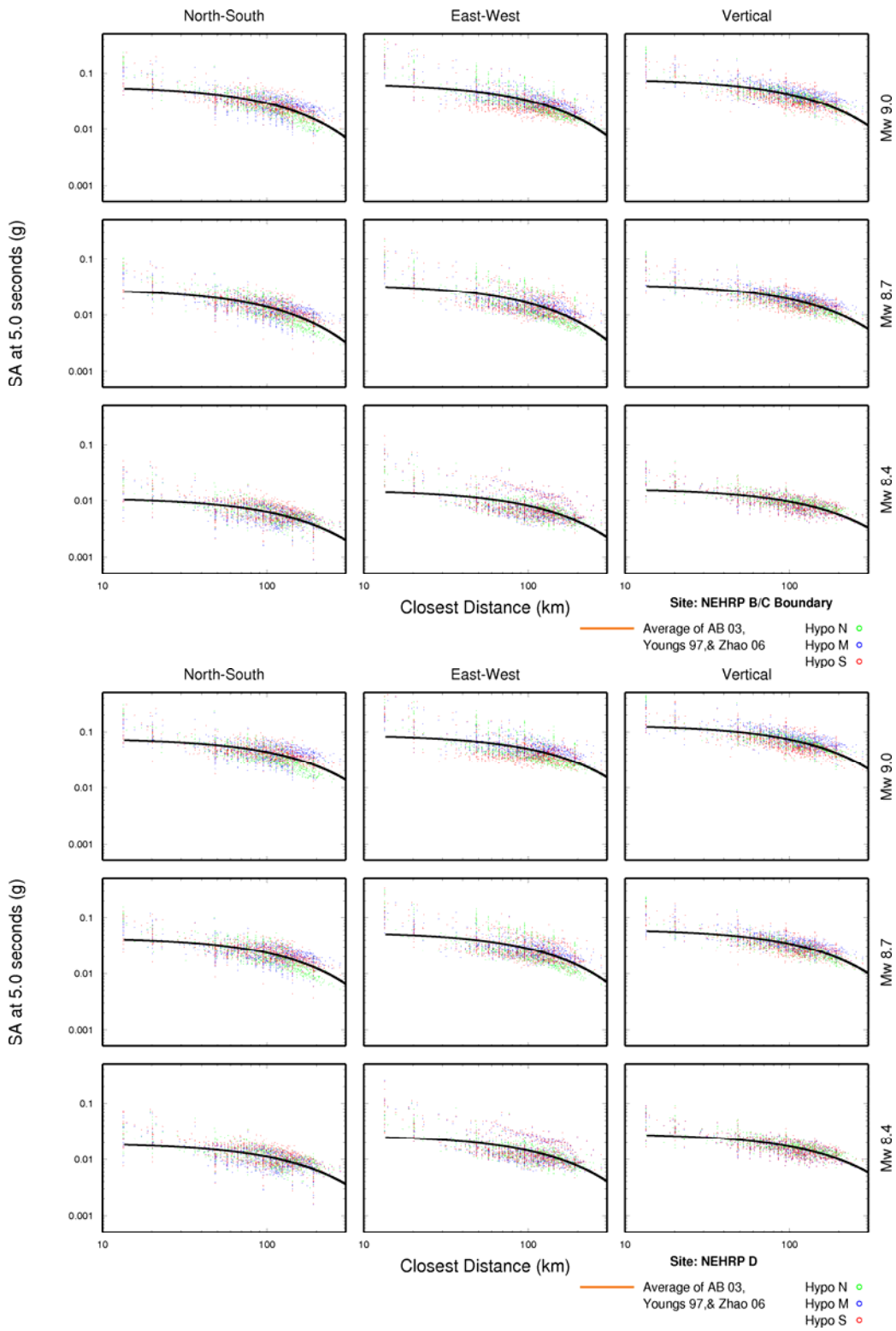

Figure 46. Comparison of simulated 5 sec spectral accelerations (points and black line) for Mw 9.0, 8.7 and 8.4 Cascadia earthquakes with the average of three ground motion models for soft rock (top) and deep soil (bottom). Only Mw 8.7 simulations have Somerville et al. (2002) scaling.

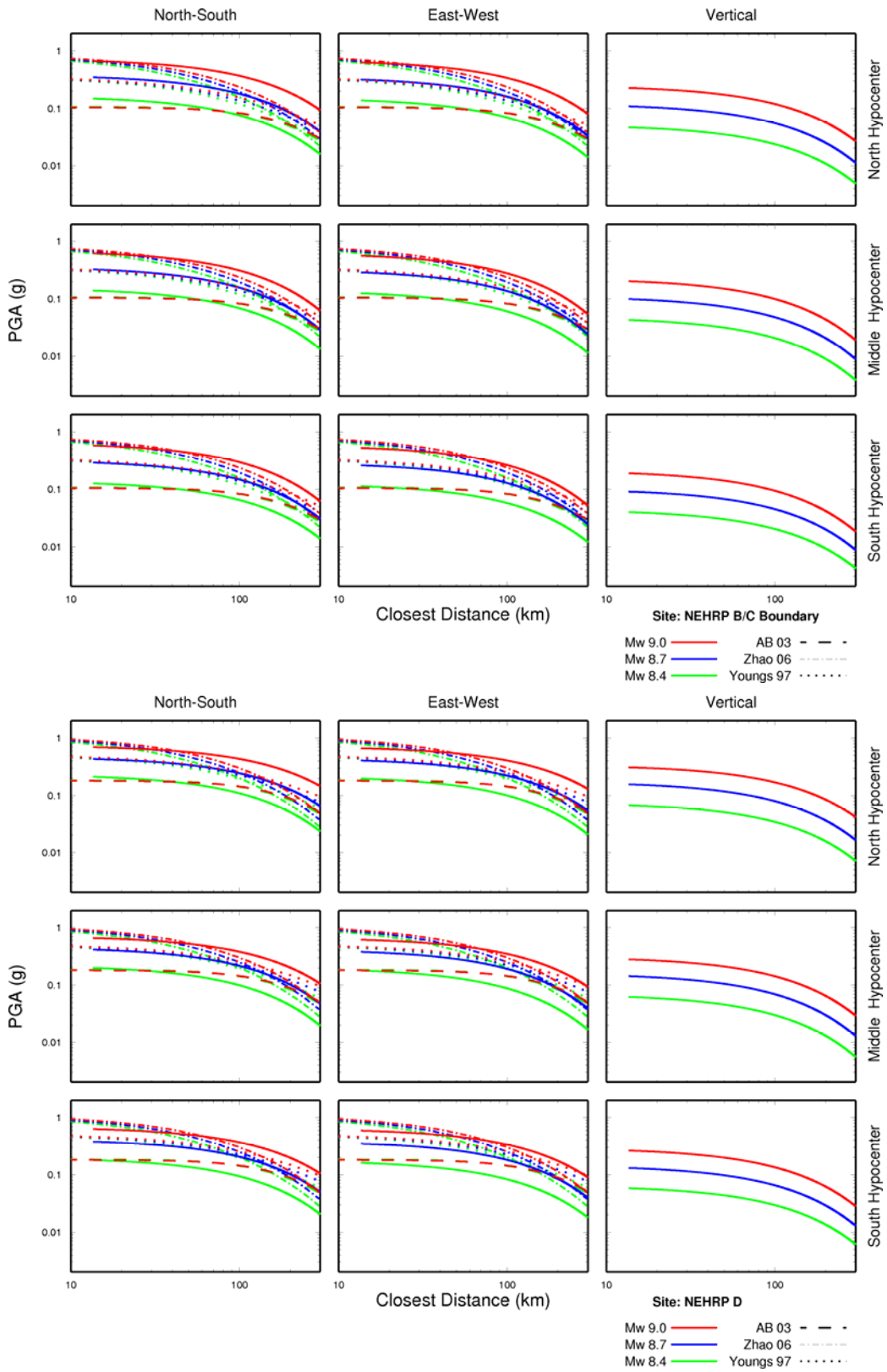

Figure 47. Comparison of simulated peak accelerations (solid lines) for Mw 9.0, 8.7 and 8.4 Cascadia earthquakes with ground motion models (dashed lines) for soft rock (top) and deep soil (bottom). Only Mw 8.7 simulations have Somerville et al. (2002) scaling.

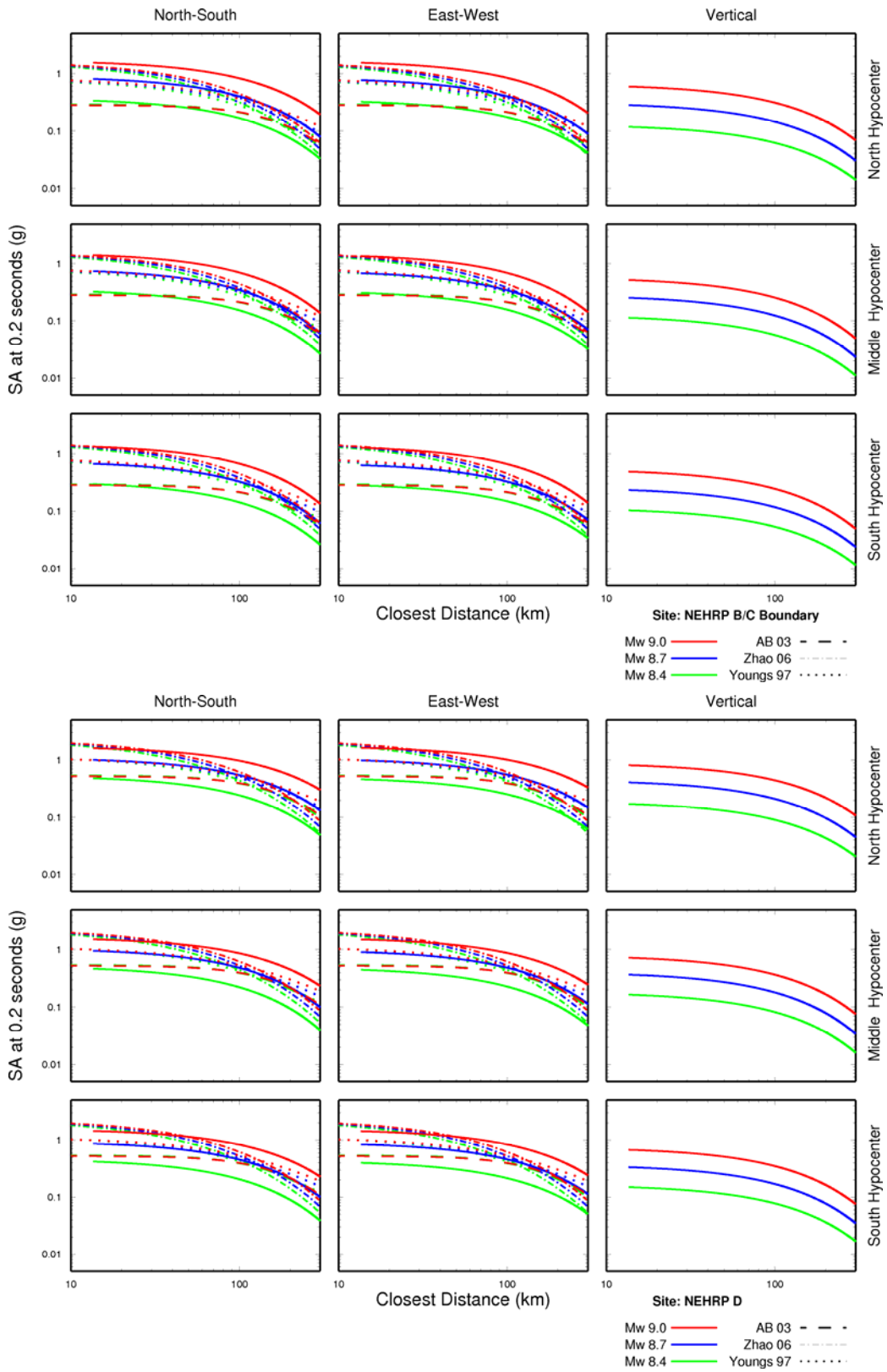

Figure 48. Comparison of simulated 0.2 sec spectral accelerations (solid lines) for Mw 9.0, 8.7 and 8.4 Cascadia earthquakes with ground motion models (dashed lines) for soft rock (top) and deep soil (bottom). Only Mw 8.7 simulations have Somerville et al. (2002) scaling.

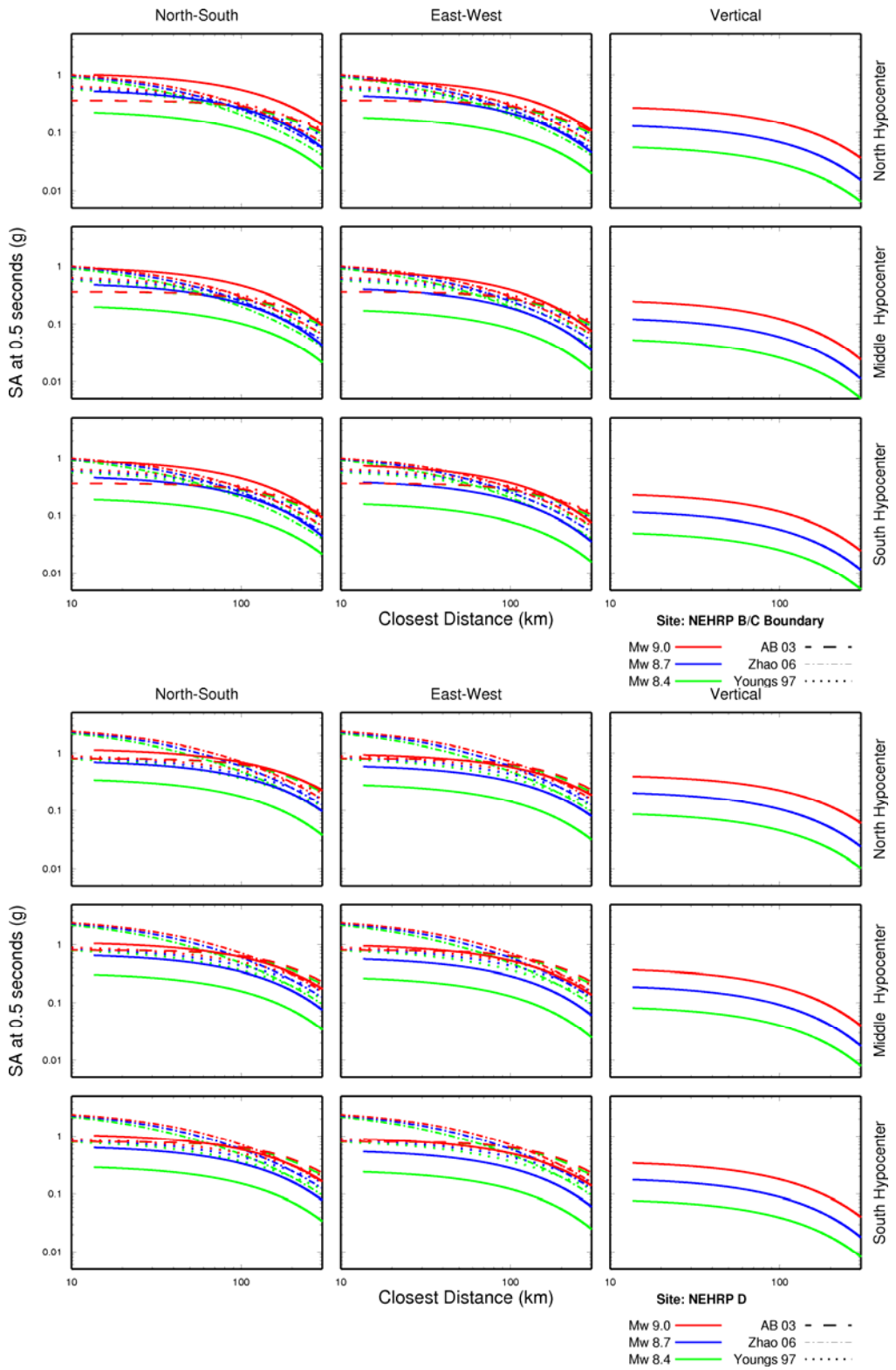

Figure 49. Comparison of simulated 0.5 sec spectral accelerations (solid lines) for Mw 9.0, 8.7 and 8.4 Cascadia earthquakes with ground motion models (dashed lines) for soft rock (top) and deep soil (bottom). Only Mw 8.7 simulations have Somerville et al. (2002) scaling.

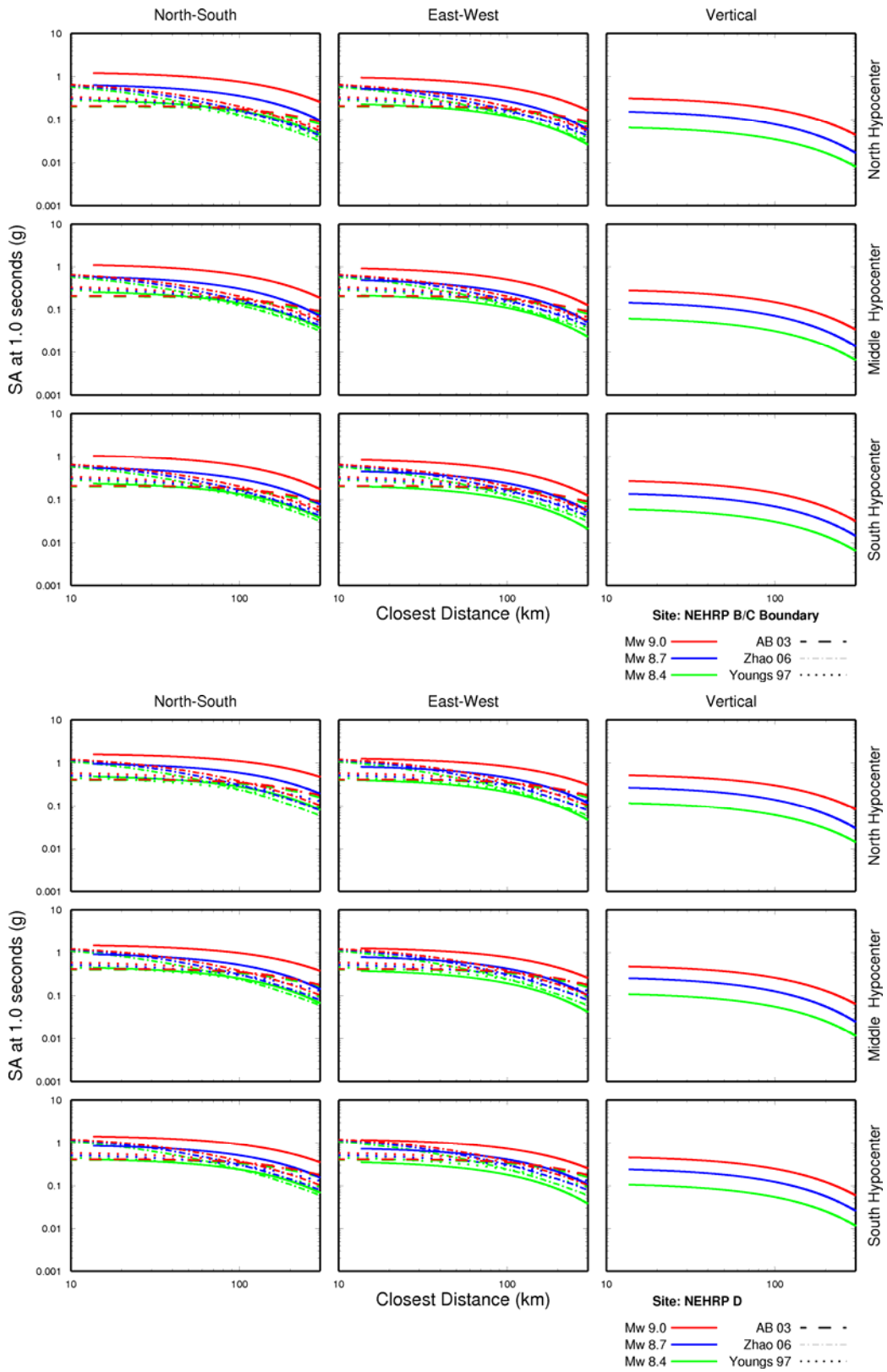

Figure 50. Comparison of simulated 1 sec spectral accelerations (solid lines) for Mw 9.0, 8.7 and 8.4 Cascadia earthquakes with ground motion models (dashed lines) for soft rock (top) and deep soil (bottom). Only Mw 8.7 simulations have Somerville et al. (2002) scaling.

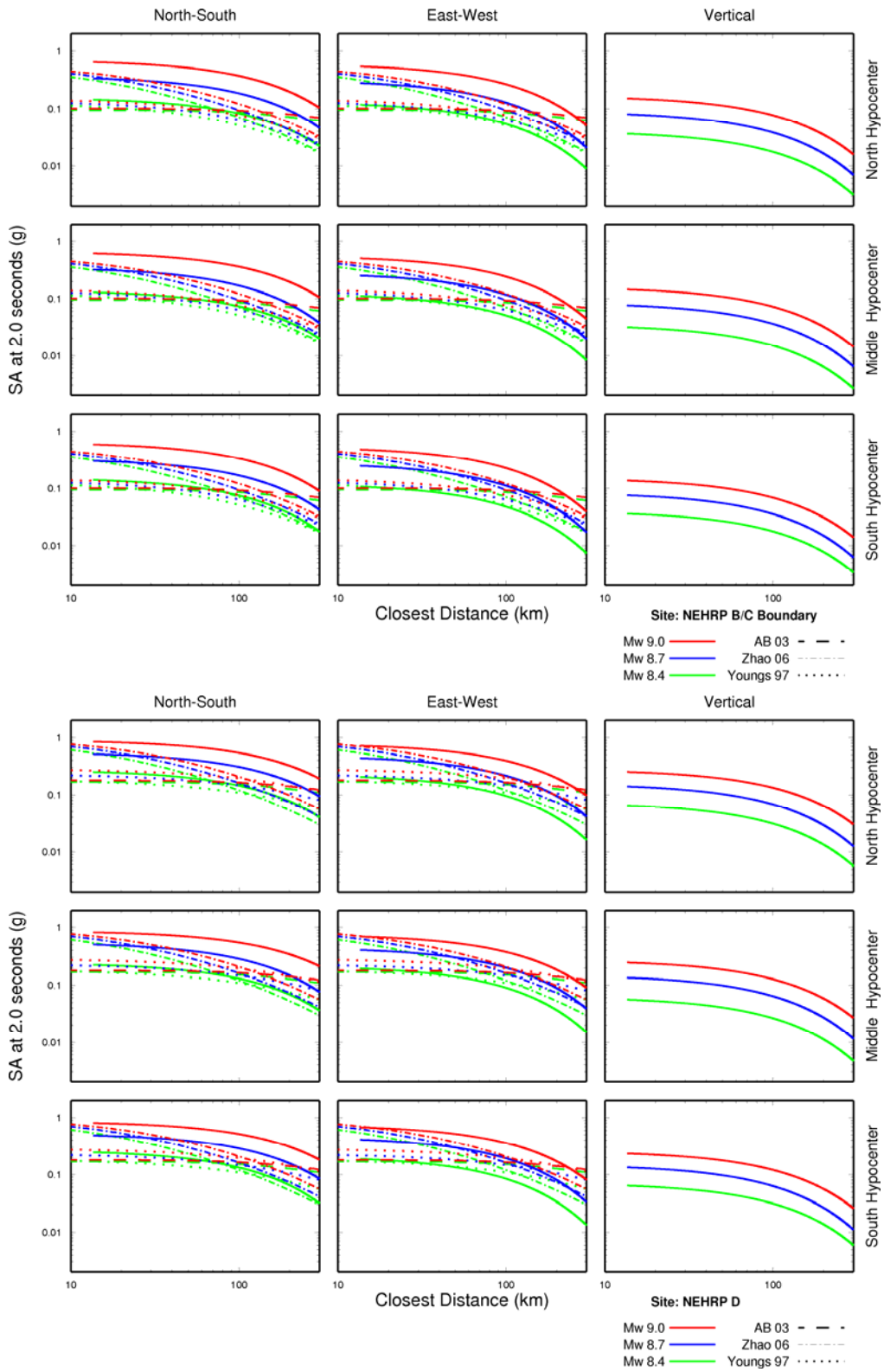

Figure 51. Comparison of simulated 2 sec spectral accelerations (solid lines) for Mw 9.0, 8.7 and 8.4 Cascadia earthquakes with ground motion models (dashed lines) for soft rock (top) and deep soil (bottom). Only Mw 8.7 simulations have Somerville et al. (2002) scaling.

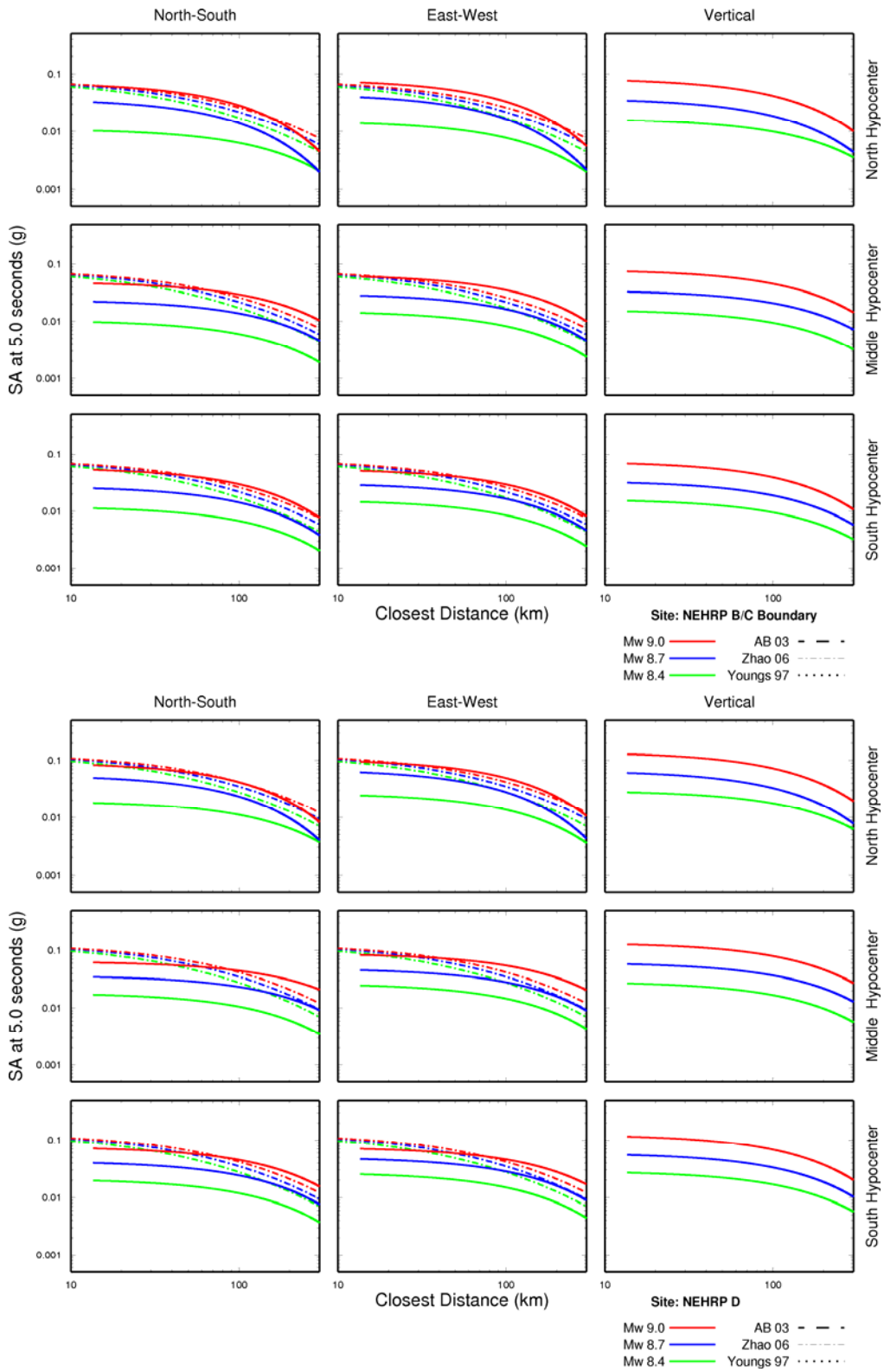

Figure 52. Comparison of simulated 5 sec spectral accelerations (solid lines) for Mw 9.0, 8.7 and 8.4 Cascadia earthquakes with ground motion models (dashed lines) for soft rock (top) and deep soil (bottom). Only Mw 8.7 simulations have Somerville et al. (2002) scaling.

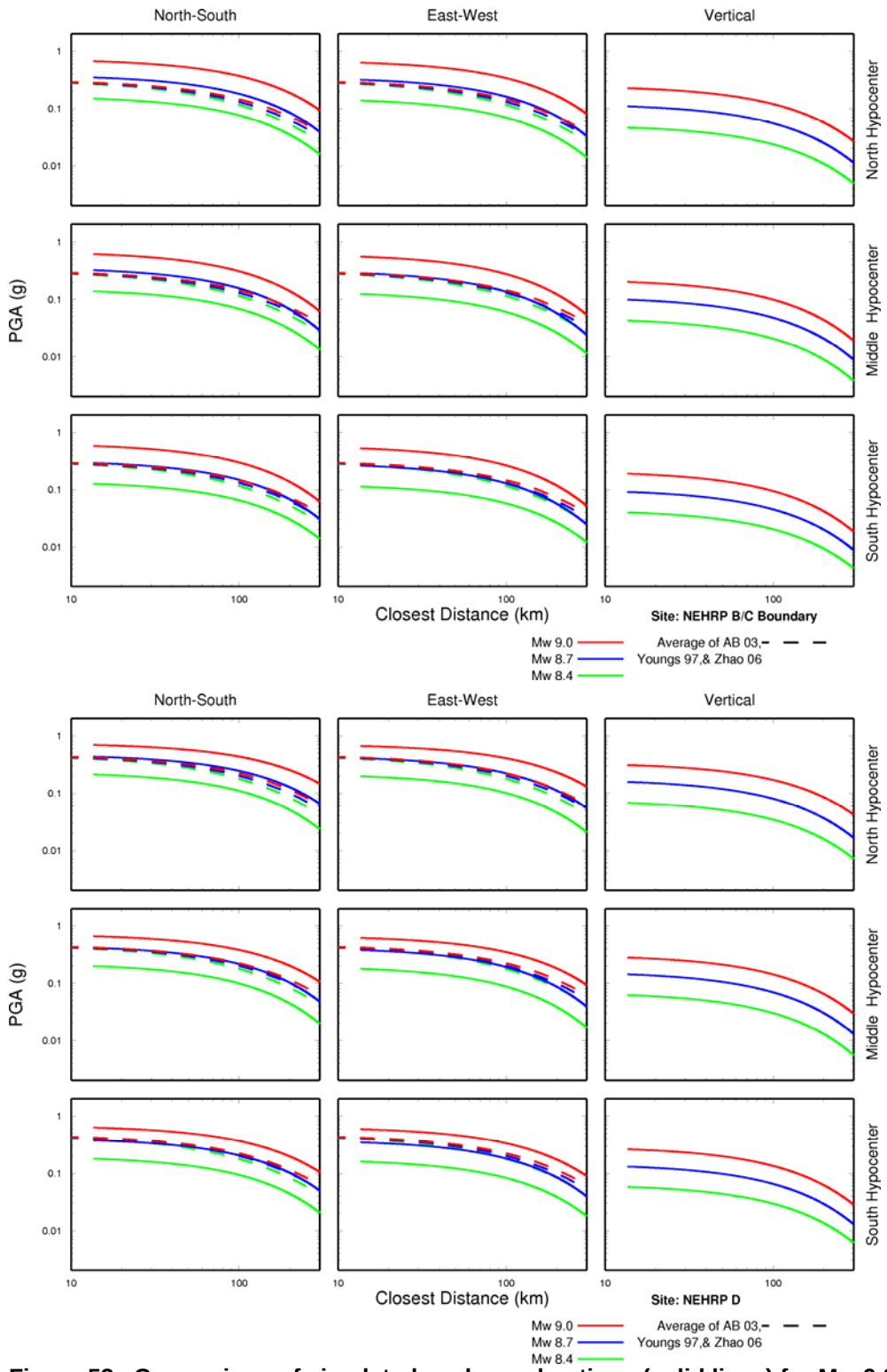

Figure 53. Comparison of simulated peak accelerations (solid lines) for Mw 9.0, 8.7 and 8.4 Cascadia earthquakes with the average of three ground motion models (dashed lines) for soft rock (top) and deep soil (bottom). Only Mw 8.7 simulations have Somerville et al. (2002) scaling.

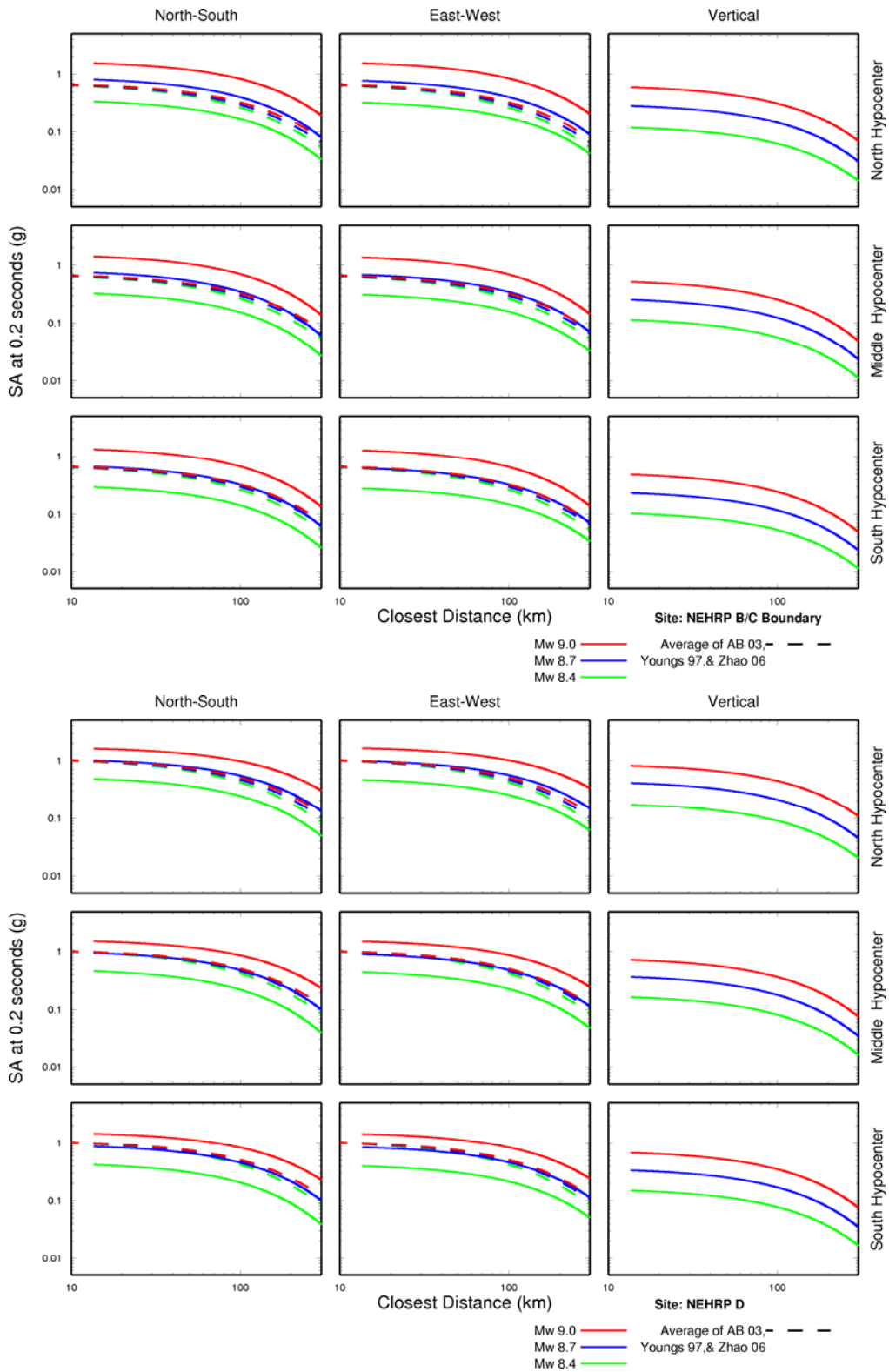

Figure 54. Comparison of simulated 0.2 sec spectral accelerations (solid lines) for Mw 9.0, 8.7 and 8.4 Cascadia earthquakes with the average of three ground motion models (dashed lines) for soft rock (top) and deep soil (bottom). Only Mw 8.7 simulations have Somerville et al. (2002) scaling.

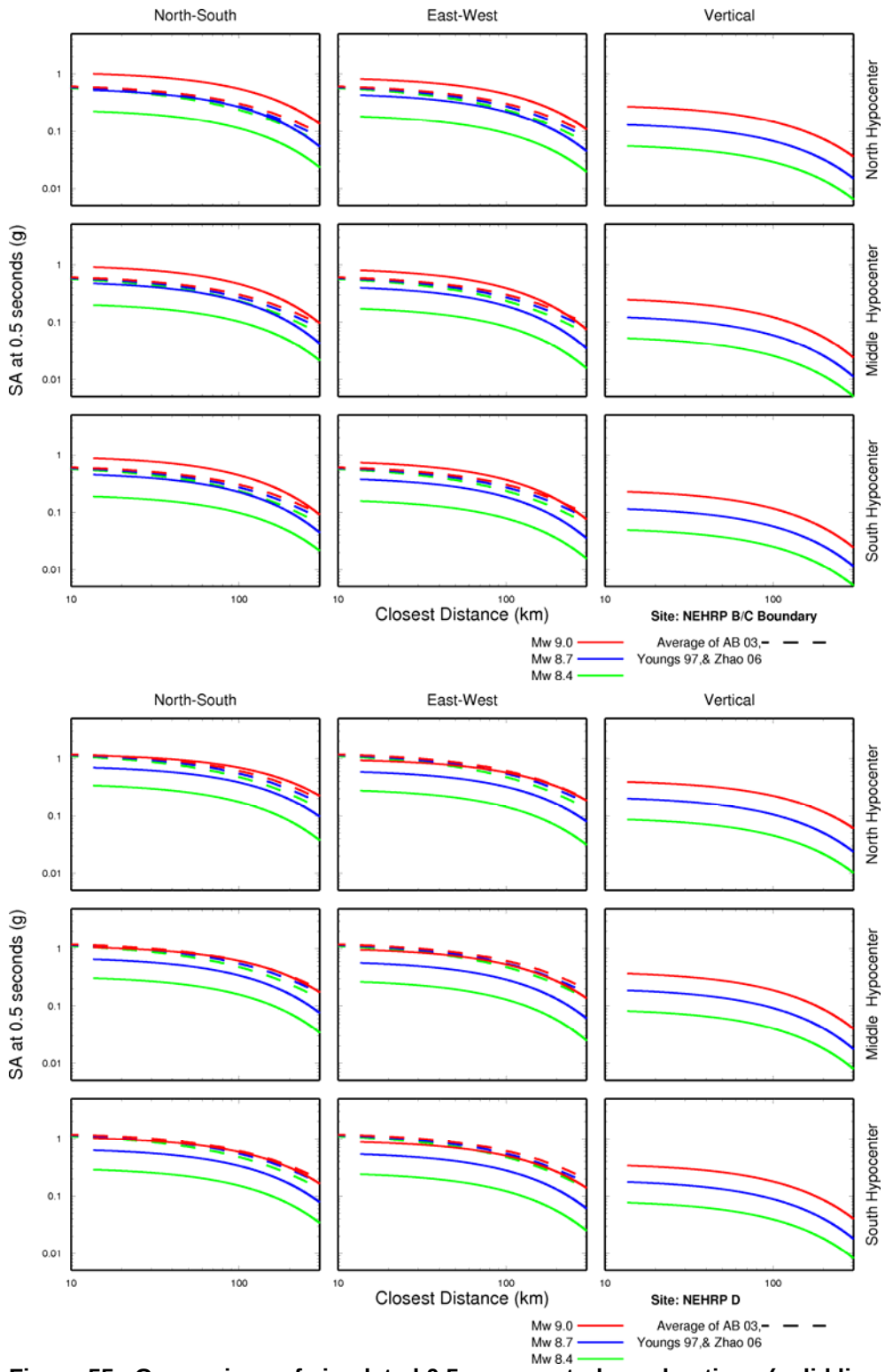

Figure 55. Comparison of simulated 0.5 sec spectral accelerations (solid lines) for Mw 9.0, 8.7 and 8.4 Cascadia earthquakes with the average of three ground motion models (dashed lines) for soft rock (top) and deep soil (bottom). Only Mw 8.7 simulations have Somerville et al. (2002) scaling.

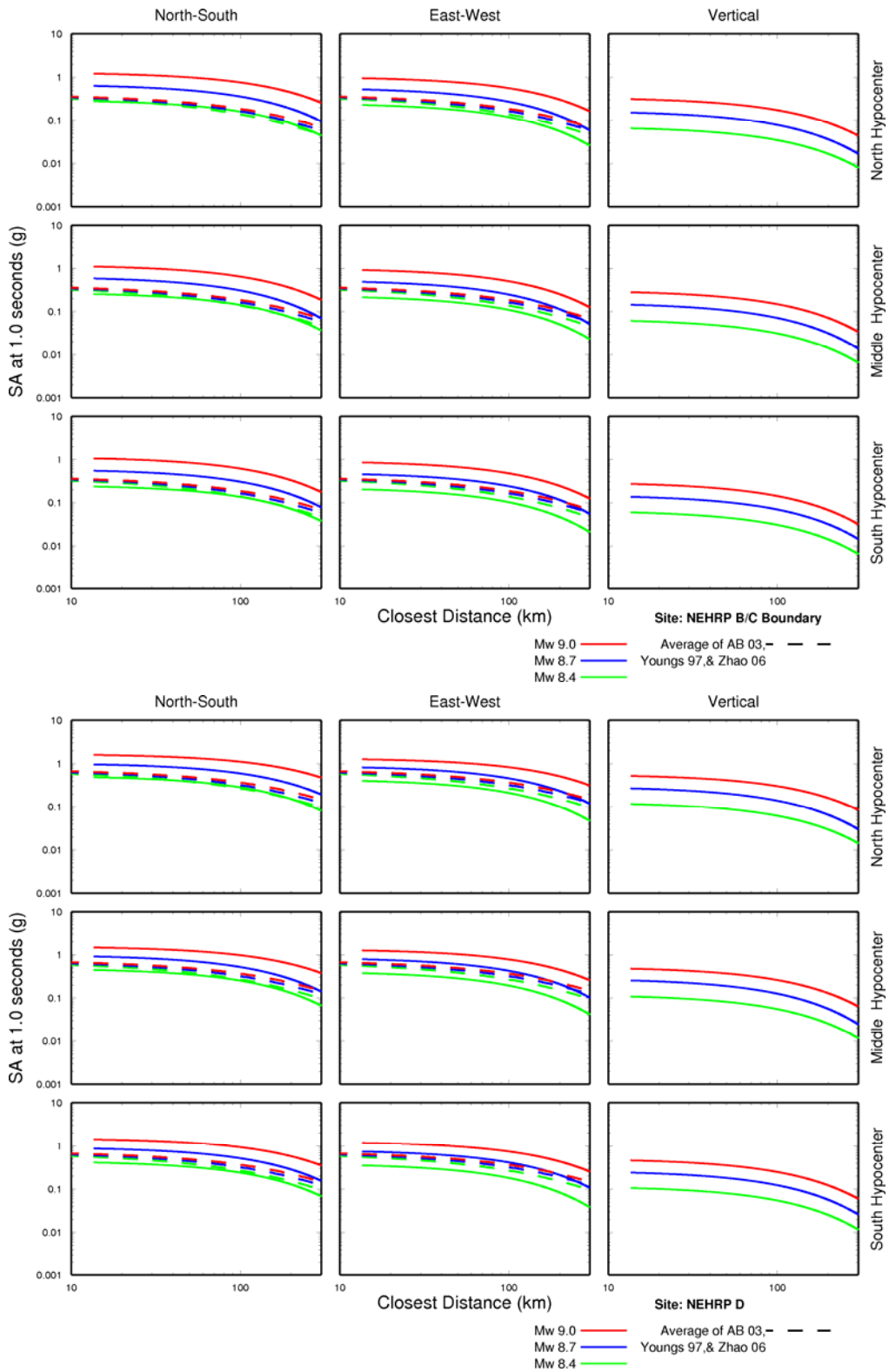

Figure 56. Comparison of simulated 1 second spectral accelerations (solid lines) for Mw 9.0, 8.7 and 8.4 Cascadia earthquakes with the average of three ground motion models (dashed lines) for soft rock (top) and deep soil (bottom). Only Mw 8.7 simulations have Somerville et al. (2002) scaling.

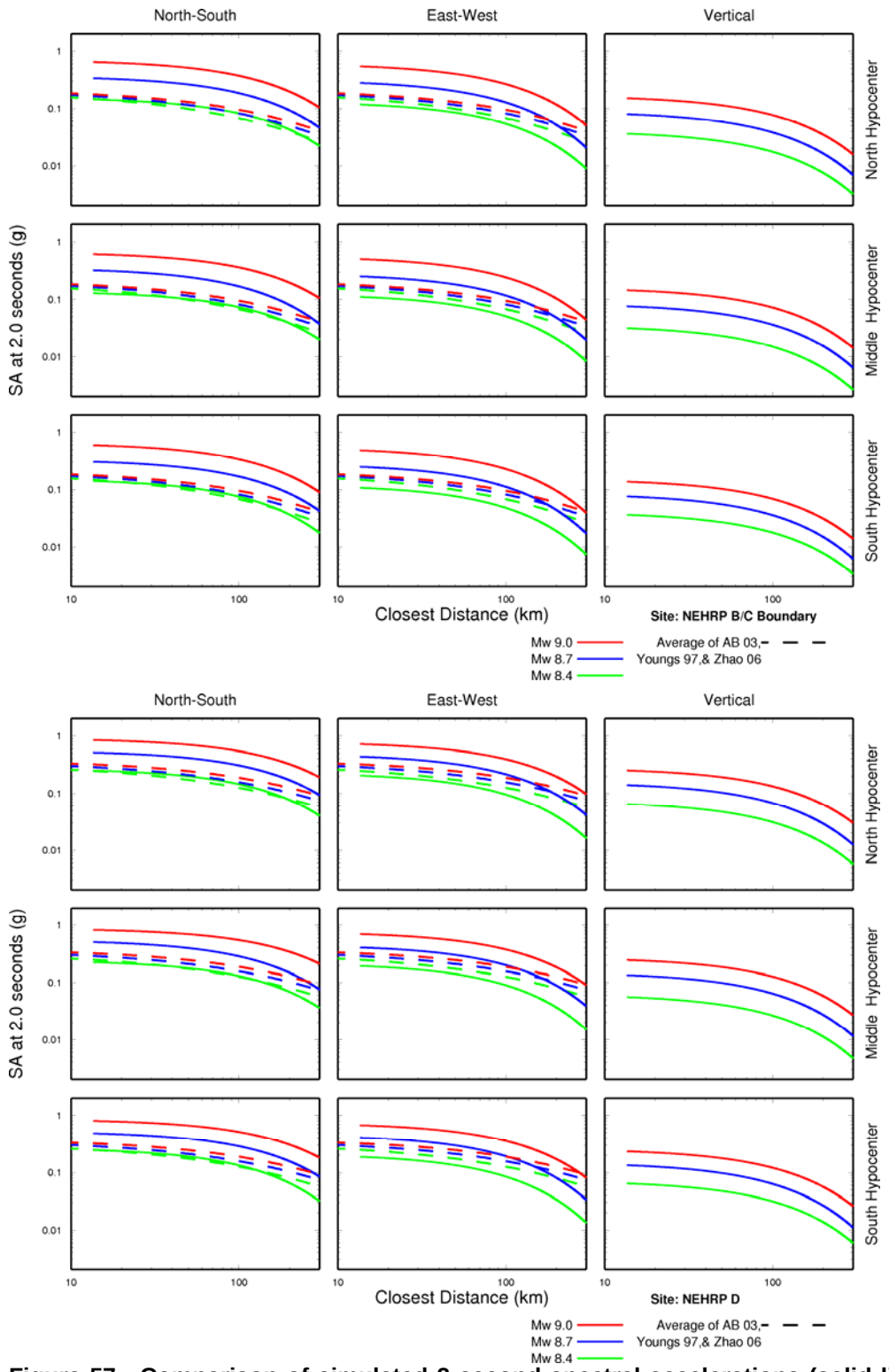

Figure 57. Comparison of simulated 2 second spectral accelerations (solid lines) for Mw 9.0, 8.7 and 8.4 Cascadia earthquakes with the average of three ground motion models (dashed lines) for soft rock (top) and deep soil (bottom). Only Mw 8.7 simulations have Somerville et al. (2002) scaling.

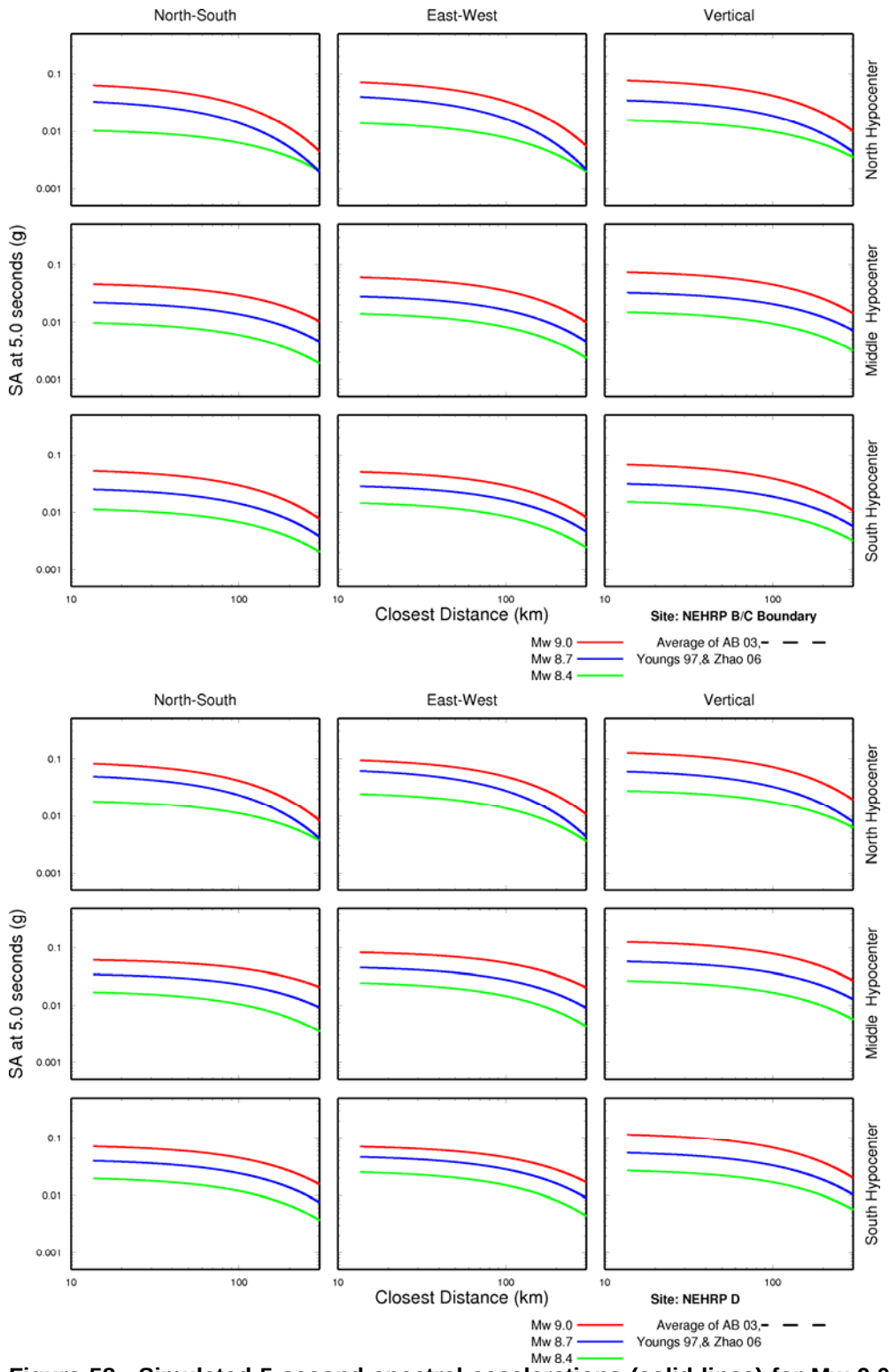

Figure 58. Simulated 5 second spectral accelerations (solid lines) for Mw 9.0, 8.7 and 8.4 Cascadia earthquakes for soft rock (top) and deep soil (bottom). Only Mw 8.7 simulations have Somerville et al. (2002) scaling.

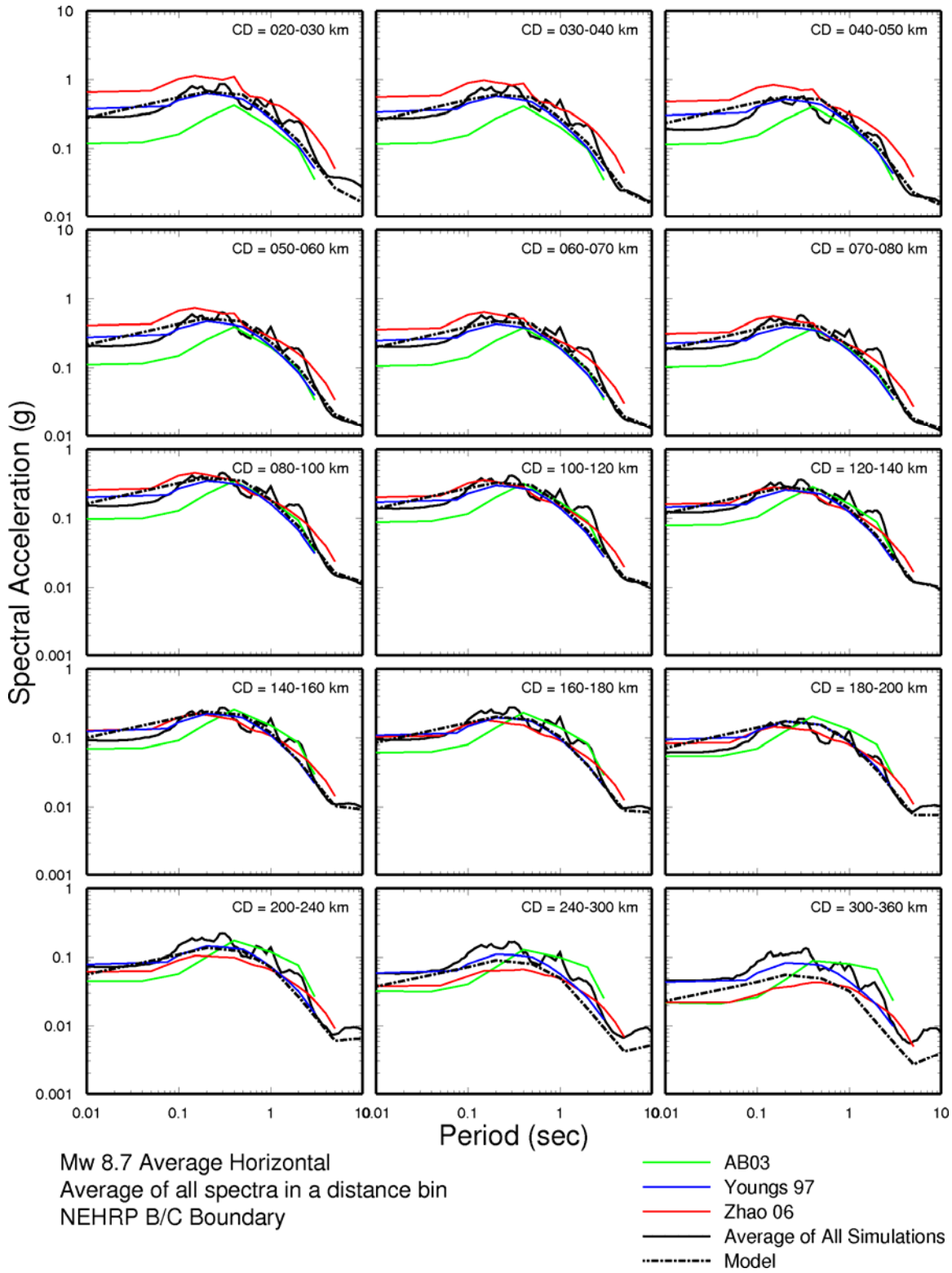

Figure 59. Comparison of simulated response spectra for a suite of distance ranges for Mw 8.7 Cascadia earthquakes for soft rock site conditions with three ground motion models, and a ground motion model representing the simulations.

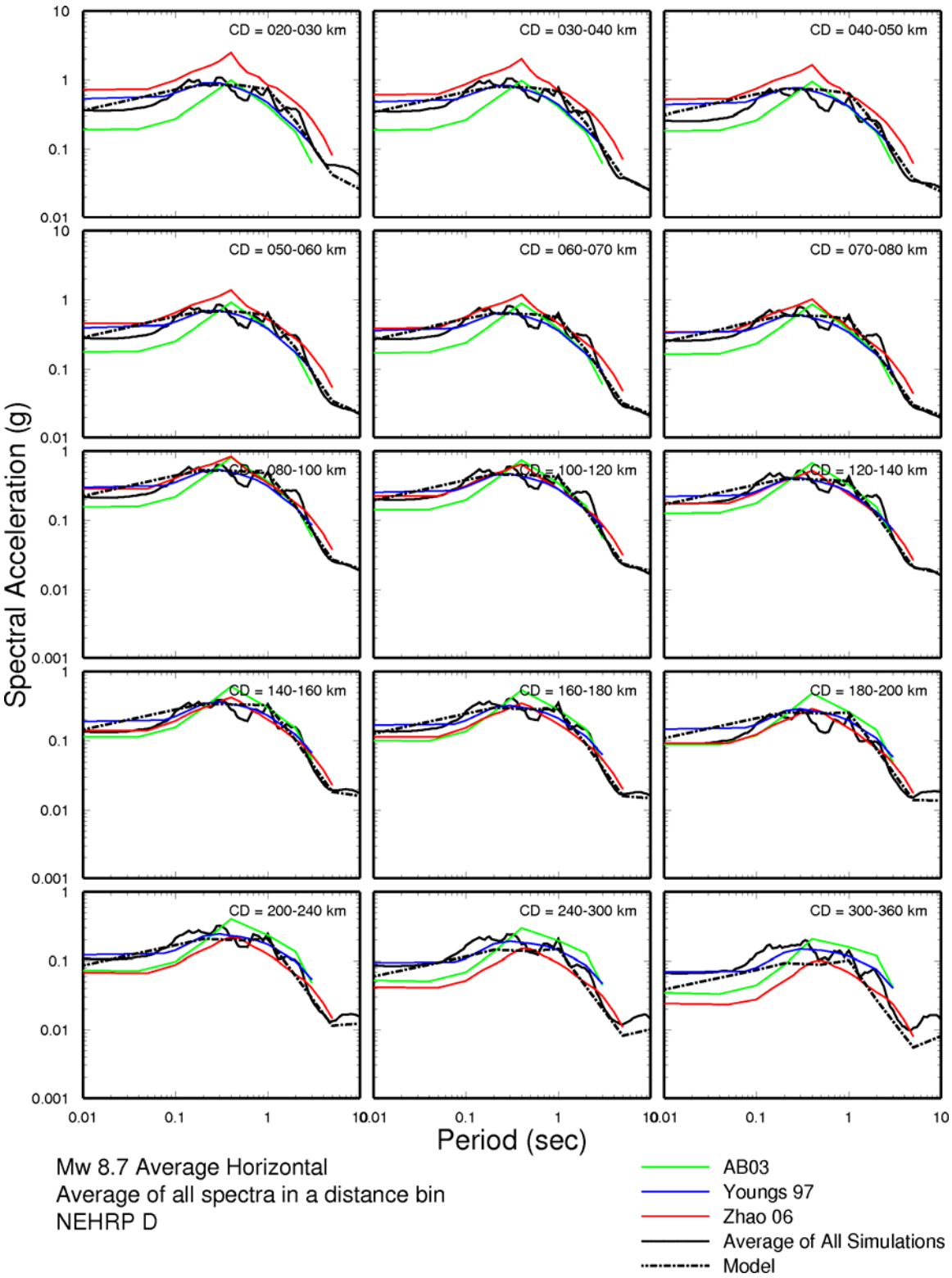

Figure 60. Comparison of simulated response spectra for a suite of distance ranges for Mw 8.7 Cascadia earthquakes for deep soil site conditions with three ground motion models, and a ground motion model representing the simulations.

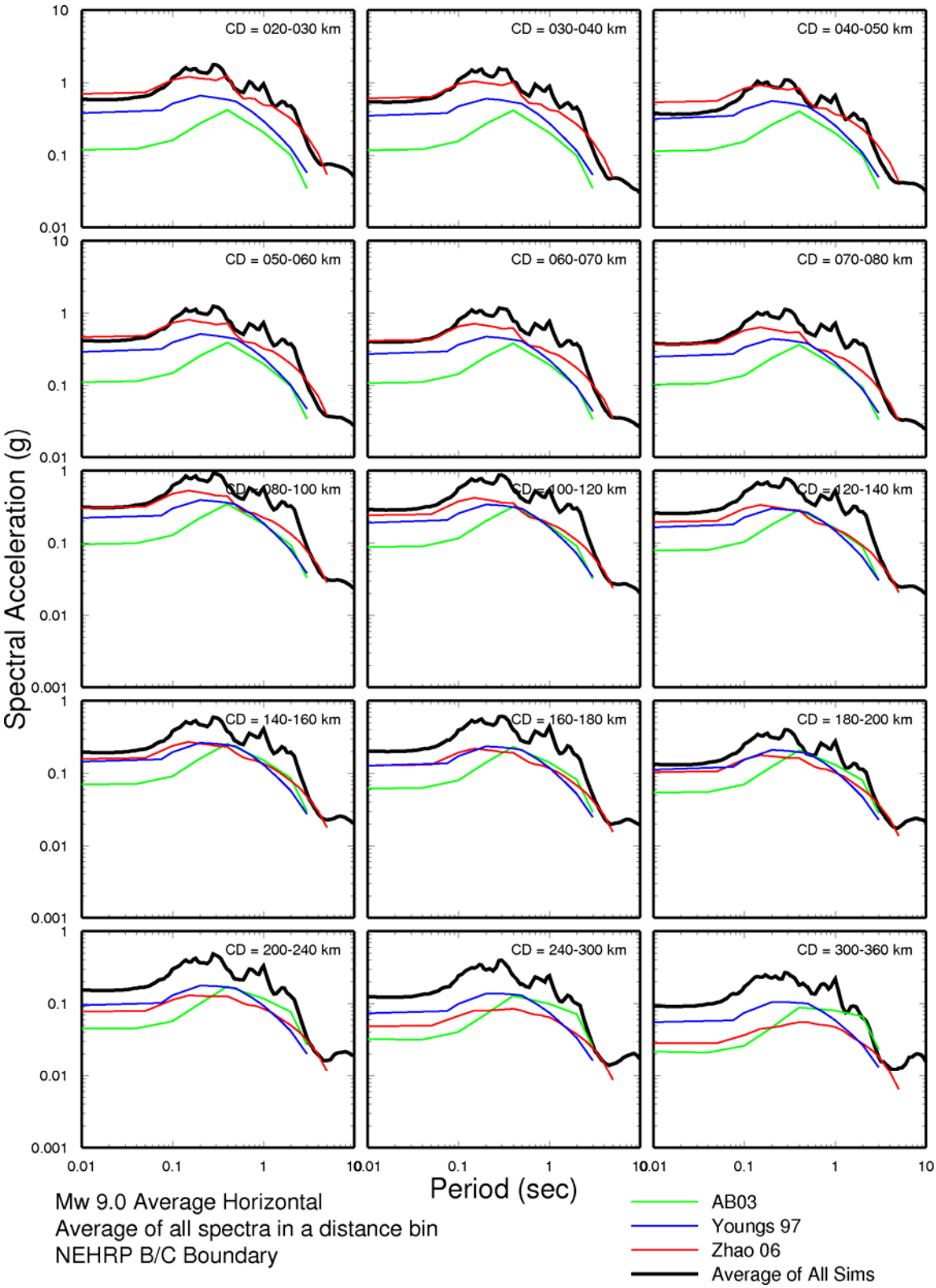

Figure 61. Comparison of simulated response spectra for a suite of distance ranges for Mw 9.0 Cascadia earthquakes for soft rock site conditions with three ground motion models. The earthquake has average slip twice as large as that predicted by the Somerville et al. (2002) scaling relations.

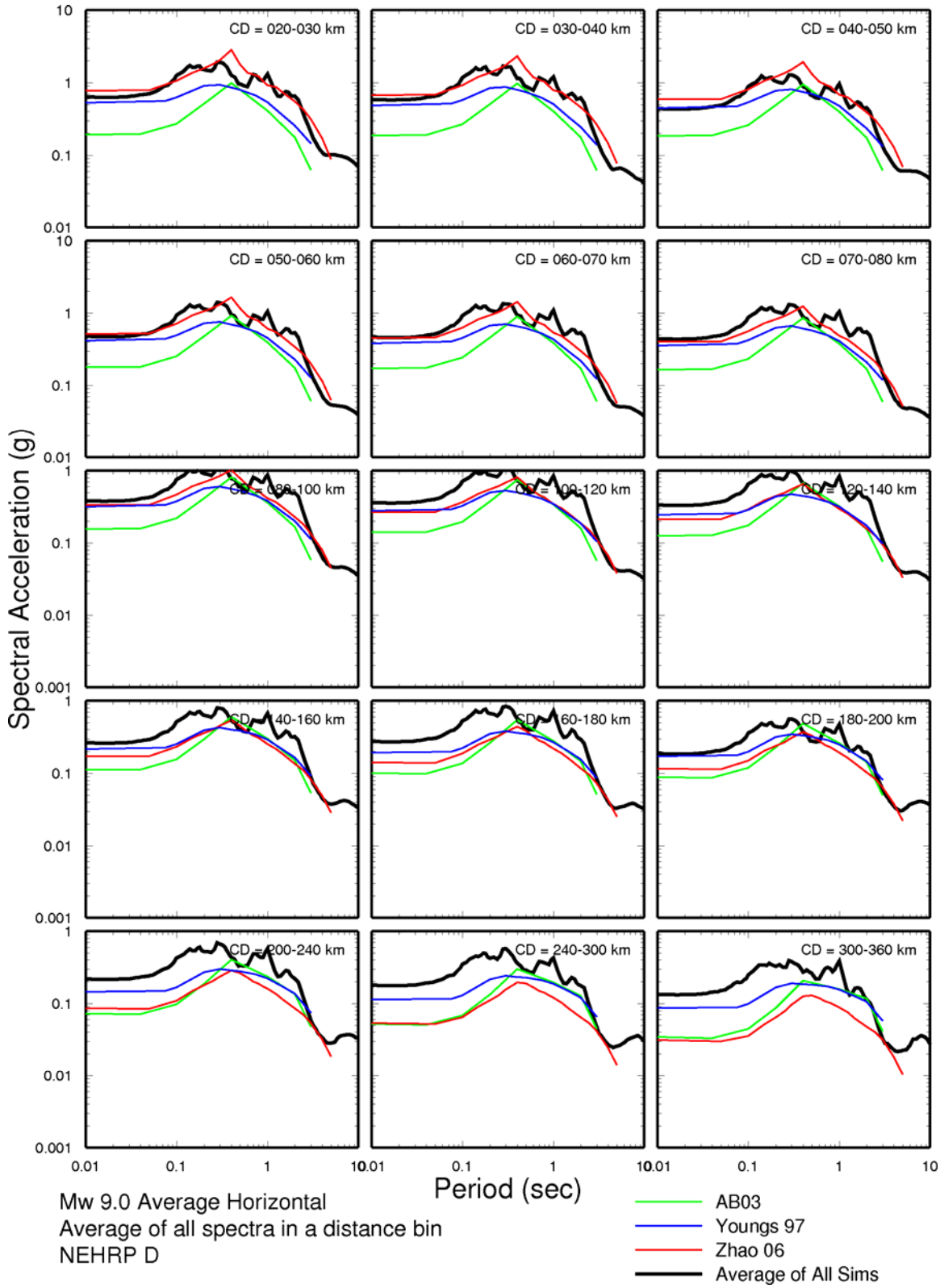

Figure 62. Comparison of simulated response spectra for a suite of distance ranges for Mw 9.0 Cascadia earthquakes for deep soil site conditions with three ground motion models. The earthquake has average slip twice as large as that predicted by the Somerville et al. (2002) scaling relations.

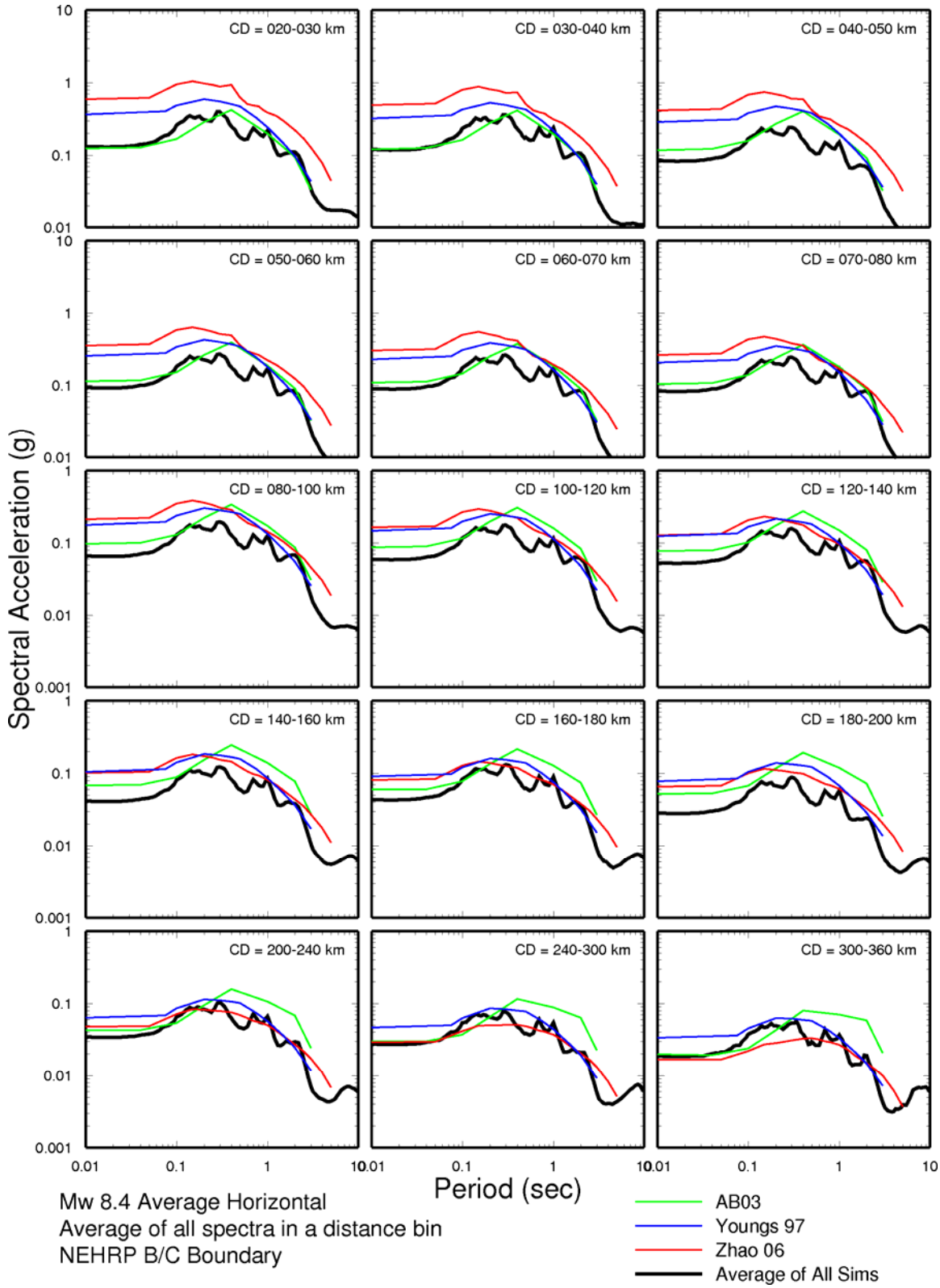

Figure 63. Comparison of simulated response spectra for a suite of distance ranges for Mw 8.4 Cascadia earthquakes for soft rock site conditions with three ground motion models. The earthquake has average slip half as large as that predicted by the Somerville et al. (2002) scaling relations.

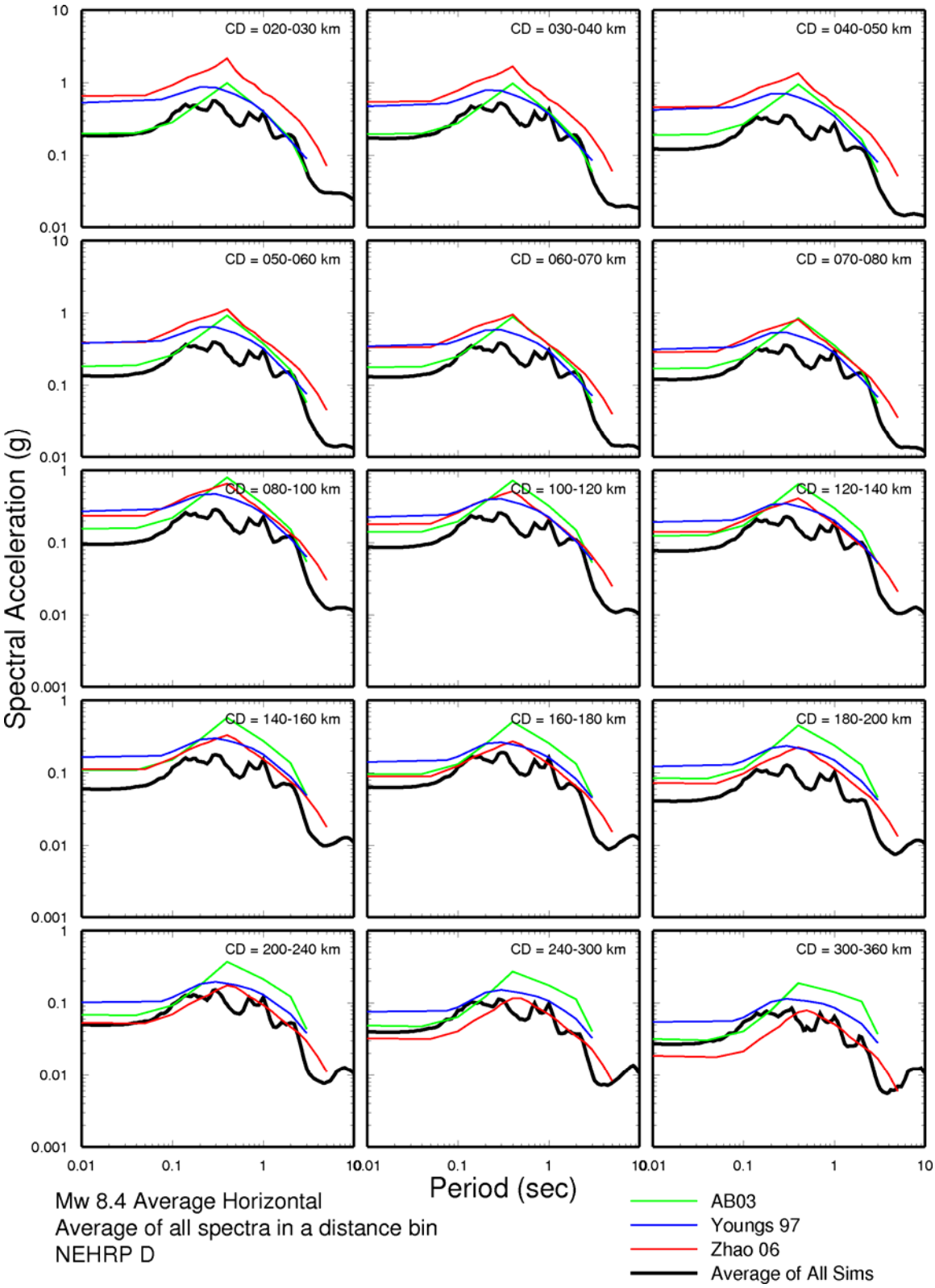

Figure 64. Comparison of simulated response spectra for a suite of distance ranges for Mw 8.4 Cascadia earthquakes for deep soil site conditions with three ground motion models. The earthquake has average slip half as large as that predicted by the Somerville et al. (2002) scaling relations.

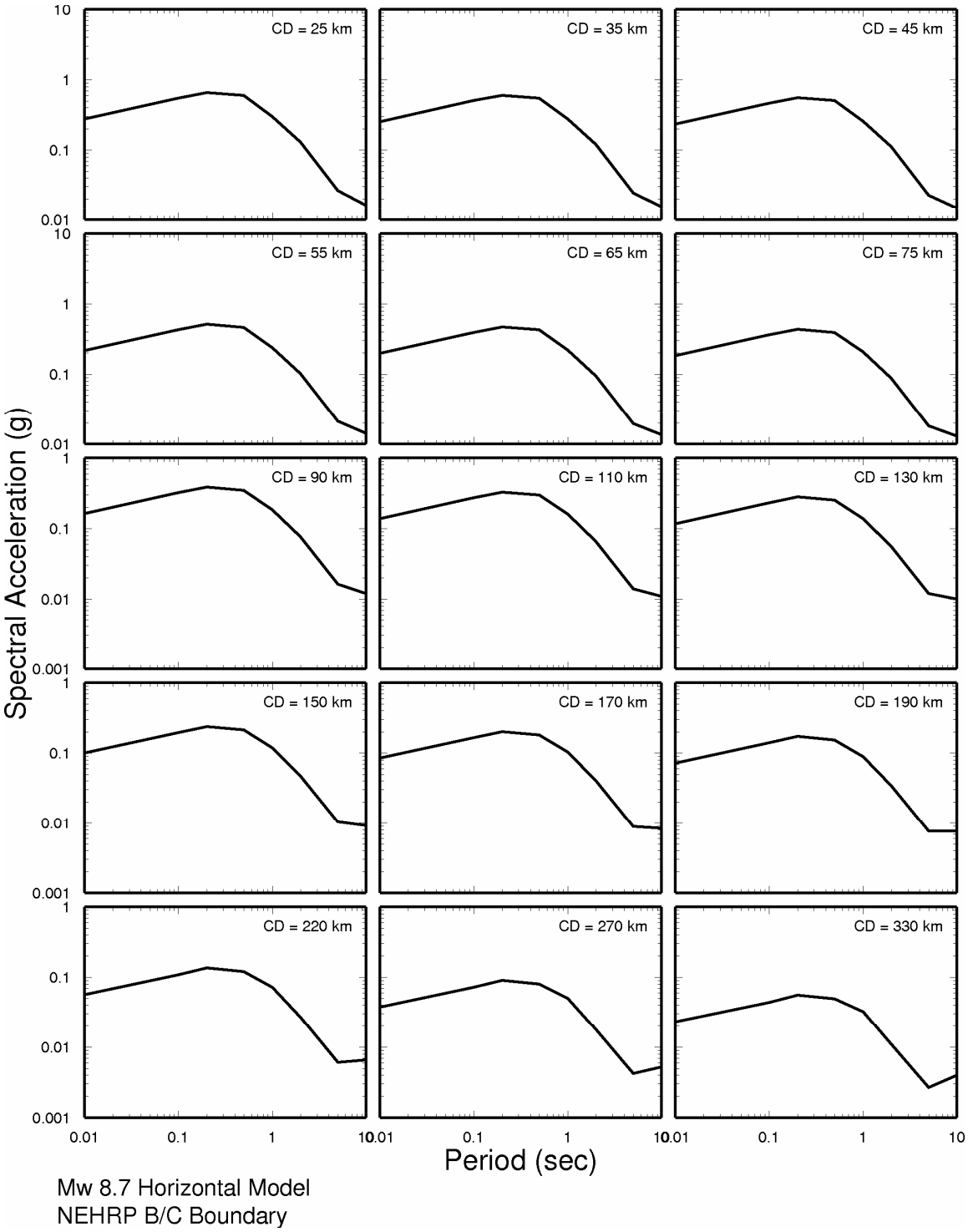

Figure 65. Model ground motion response spectra for a suite of distances for Mw 8.7 Cascadia earthquakes for soft rock site conditions derived from strong motion simulations.

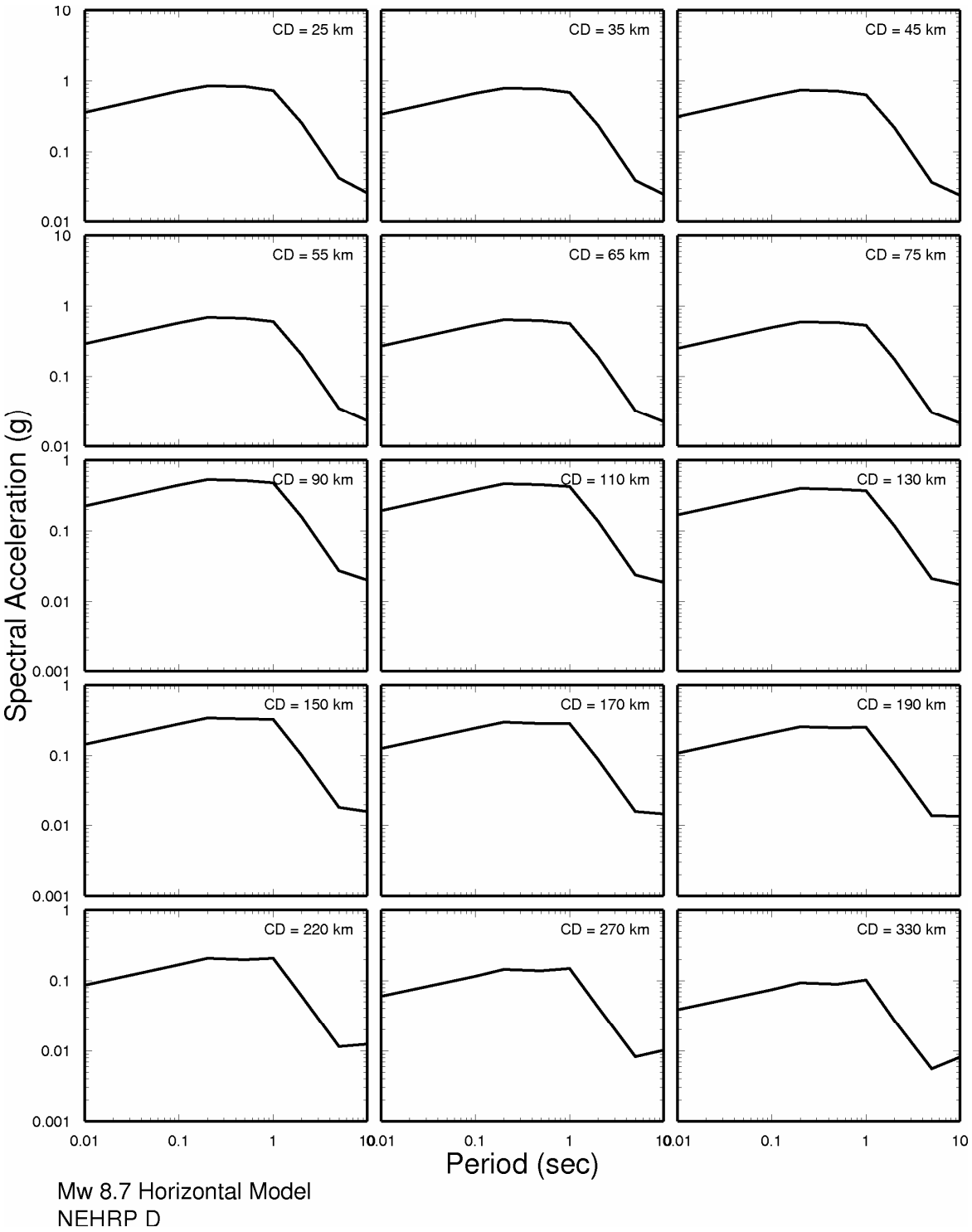

Figure 66. Model ground motion response spectra for a suite of distances for Mw 8.7 Cascadia earthquakes for deep soil site conditions derived from strong motion simulations.

REFERENCES

Abrahamson, N.A., P.G. Somerville, and C. Allin Cornell (1990). Uncertainty in numerical strong motion predictions, *Proc. 4th U.S. National Conference on Earthquake Engineering,* **1**, 407- 416.

Atkinson, G.M. and D.M. Boore (2003). Empirical ground motion relations for subduction zone earthquakes and their application to Cascadia and other regions, *Bull. Seism. Soc. Am*., in press.

Boroscheck, R., and D. Comte (2004). Time – frequency characteristics of the 2001 Southern Peru, Mw 8.4 earthquake. 13th World Conference on Earthquake Engineering, Vancouver, B.C., Canada, August 1 – 6, Paper No. 287.

Brocher, T.M., T. Parsons, A. Trehu, C.M. Snelson, and M.A. Fisher (2003). Seismic evidence for widespread serpentinized forearc upper mantle along the Cascadia margin. Geology 31, 267-270.

Clowes, R.M., M.T. Brandon, A.G. Green, C.J. Yorath, A.S. Brown, E.R. Kanasewich, and C. Spencer (1987). LITHOPROBE – southern Vancouver Island: Cenozoic subduction complex imaged by deep seismic reflections. Can. J. Earth Sci., 24, 31-51.

Cohee, B.P., P.G. Somerville and N.A. Abrahamson (1991). Ground motions from hypothesized M_w = 8 subduction earthquakes in the Pacific Northwest, *Bull. Seism. Soc. Am.*, **81**, 28-56.

Graves, R.W. and A. Pitarka (2004). Broadband time history simulation using a hybrid approach. Proceedings of the 13th World Conference on Earthquake Engineering, Vancouver, Canada, August 1-6, 2004, Paper No. 1098.

Graves, R.W. (2005). Broadband simulation for a Mw 6.7 earthquake on the Puente Hills Fault. *SRL* 76, p. 242.

Guatteri, M., Mai, P.M., Beroza, G., and Boatwright, J. (2003). Strong ground motion prediction from stochastic-dynamic source models." Bull. Seism. Soc. Am. 93: 301-313.

Hartzell S. (1978). Earthquake aftershocks as Green's functions. Geophys. Res. Lett. 5: 1-4.

Hartzell S., and T. Heaton (1983). Inversion of strong ground motion and teleseismic waveform data for the fault rupture history of the 1979 Imperial Valley, California earthquake. Bull. Seism. Soc. Am. 1983; 1553-1583.

Hisada, Y. (2001). A theoretical omega-squared model considering spatial variation in slip and rupture velocity. Part 2. Case for a two-dimensional source model. Bull. Seism. Soc. Am. 91, 651-666.

Irikura K. (1978). Semi-empirical estimation of strong ground motions during large earthquakes. Bull. Disast. Prev. Res. Inst., Kyoto Univ. 33: 63-104.

Ichinose, G. A., H. K. Thio, P. G. Somerville, T. Sato, and T. Ishii (2003). Rupture model for the 1944 Tonankai earthquake from the inversion of teleseismic and regional seismograms, J. Geophys. Res. 108, 10, 2497.

Ichinose, G., H.K. Thio and P. Somerville (2003b). Source characteristics of modern and historical in-slab Cascadia earthquakes applicable to strong motion prediction. USGS Final Report, Award 02HQGR0018.

Ishii, T. T. Sato and P.G. Somerville (2000). Identification of main rupture areas of heterogeneous fault models for strong motion estimates. J. Struct. Constr. Eng. AIJ, 527, 61-70.

Kagawa, T., K. Irikura and P.G. Somerville (2004). Differences in ground motion and fault rupture process between the surface and buried rupture earthquakes. *Earth Planets Space*, 56, 3-14.

Mai, M.P. and G. Beroza. (2002). A spatial random field model to characterize complexity in earthquake slip. J. Geophys. Res. 107(B11): doi:10.1029/2001JB000588.

McNeill, A.F., M.G. Bostock, G.C. Rogers, and J.C Shragge (2004). The effect of forearc mantle serpentinization on ground motions from megathrust and intraslab events in the Cascadia subduction zone. BSSA. 94, 147-154.

Ocola, L.C., J. Luetgert, L.T. Aldrich, R.P. Meyer, and C.E. Helsey (1995). Velocity structure of the coastal region of southern Peru from seismic refraction / wide-angle reflection data. J. Geodynamics 20, 1-30.

Ohtsuka, H., P.G. Somerville, and T. Sato (1998). Estimation of broadband strong ground motions considering uncertainty of fault parameters, J. Struct. Mech. Earthq. Eng., JSCE, No.584/I-42, 185-200.

Petersen, M., A. Frankel, A., S. Harmsen, C. Mueller, K. Haller, R. Wheeler, R. Wesson, Y. Zeng, O. Boyd, D. Perkins, N. Luco, E. Field, C. Wills, and K. Rukstales (2008). Documentation for the 2008 updated of the United States National Seismic Hazard Maps. *U.S. Geological Survey Open File Report* 2008-1128.

Petersen, M.D., C.H. Cramer, and A.D. Frankel (2002). Simulations of seismic hazard for the Pacific Northwest of the United States from earthquakes associated with the Cascadia subduction zone. Pure Appl. Geophys. 159, 2147-2168.

Pitarka, A., R. Graves, P.G. Somerville (2002). Investigation of effects of the Seattle Fault Zone structural complexities on ground motions in the Seattle Basin, EOS 83.

Somerville, P.G., H.K. Thio, G, Ichinose, N. Collins, A. Pitarka, and R.Graves (2003). Earthquake source and ground motion characteristics of the June 23, 2001 M_w 8.4 Arequipa, Peru, earthquake. *SRL* 74, 223.

Somerville, P.G., T. Sato, T. Ishii, N.F. Collins, K. Dan and H. Fujiwara (2002). Characterizing heterogeneous slip models for large subduction earthquakes for strong ground motion prediction. Proceedings of the Architectural Institute of Japan.

Somerville, P.G., K. Irikura, R. Graves, S. Sawada, D. Wald, N. Abrahamson, Y. Iwasaki, T. Kagawa, N. Smith and A. Kowada (1999). Characterizing earthquake slip

models for the prediction of strong ground motion. *Seismological Research Letters* 70, 59-80.

Somerville, P.G., M.K. Sen and B.P. Cohee (1991). Simulation of strong ground motions recorded during the 1985 Michoacan, Mexico and Valparaiso, Chile earthquakes, *BSSA.*, **81**, 1-27.

Wald, D.J. and P.G. Somerville (1995). Variable slip rupture model of the great 1923 Kanto, Japan earthquake: geodetic and body-waveform analysis. *Bull. Seism. Soc. Am.*, 85, 159-177.

Youngs, R.R., S.-J. Chiou, W.J. Silva, and J.R. Humphrey (1997). Strong ground motion relationships for subduction earthquakes, *Seismological Research Letters* 68, 58-73.

Zhao, J.X., J. Zhang, A. Asano, Y. Ohno, T. Oouchi, T. Takahashi, H. Ogawa, K. Irikura, H.K. Thio, P. Somerville, Y. Fukushima, and Y. Fukushima (2006). Attenuation Relations of Strong Motion in Japan using Site Classification based on Predominant Period. *Bull. Seism. Soc. Am*. 96, 898-913.